Fabrication and Characterization of Graphene Reinforced Titanium Matrix Composites

A thesis submitted in fulfilment of the requirement for the award of the degree of

DOCTOR OF PHILOSOPHY

IN

MECHANICAL ENGINEERING

Submitted by

DEEPAK SHARMA

Roll No. 901708010

Under the supervision of

Dr. Vinod Kumar
Associate Professor
Department of Mechanical Engineering

Dr. Sachin Singh
Assistant Professor, MED
Department of Mechanical Engineering

Department of Mechanical Engineering,

Thapar Institute of Engineering and Technology, Patiala-147004, India

(Deemed to be University)

August, 2024

CANDIDATE'S DECLARATION

I, Deepak Sharma, Roll No. 901708010, hereby declared that the thesis entitled **"Fabrication and Characterization of Graphene Reinforced Titanium Matrix Composites"** submitted to the Department of Mechanical Engineering at Thapar Institute of Engineering and Technology, Patiala, Punjab (India) is an authenticated record of my own research work for the award of the degree **"Doctor of Philosophy"** under the supervision of **Dr. Vinod Kumar and Dr. Sachin Singh**. This report has not been submitted to any other institute for the award of any other degree.

Place: Patiala

Deepak Sharma

Dated: 06/08/2024

Roll No. 901708010

This is to certify that above declaration made by the student is correct to the best of my knowledge.

Dr. Vinod Kumar 06/08/2024
Associate Professor
Department of Mechanical Engineering
Thapar Institute of Engineering
and Technology, Patiala-147004 (Punjab)
India
(Supervisor)

Dr. Sachin Singh 6/8/24
Assistant Professor
Department of Mechanical Engineering
Thapar Institute of Engineering
and Technology, Patiala-147004 (Punjab)
India
(Supervisor)

i

ACKNOWLEDGEMENT

First and foremost, I am deeply grateful to the **Almighty** for guiding me throughout this journey and granting me the strength and perseverance to accomplish this milestone.

I extend my heartfelt appreciation to my supervisors, **Dr. Vinod Kumar** and **Dr. Sachin Singh**, for their invaluable guidance, unwavering support, and insightful feedback. Their expertise, encouragement, and patience have been instrumental in shaping this thesis and enriching my academic journey. I feel honored to have worked under their mentorship throughout my Ph.D. work.

I thank the doctoral committee members **Dr. T.K. Bera** (Chairman, Board of Studies), **Dr. Anant Kumar Singh**, **Dr. Ravinder Joshi,** and **Dr. Satnam Singh** for the feedback and reviews that were given on my research proposal and progress monitoring presentations. Their guidance was beneficial for me to improve my research work. I am also thankful to **Dr. Tarun Nanda** and **Dr. Anu Mittal** our Ph.D. coordinators for their approachability and informing me with all the relevant communication.

I am thankful to all the Lab technicians and clerical staff of the Mechanical Engineering Department, especially **Mr. Sarabjit Singh** and **Mr. Narinder Singh** for their selfless contribution.

I am indebted to my loving parents, wife, and sisters for their unconditional love, endless encouragement, and unwavering belief in my abilities. Their sacrifices and understanding have been my pillar of strength throughout this endeavor. I am also thankful to my dear friends Mr. Kunal Arora, Mr. Rahul Gupta, Mr. Ashutosh Bisht, Mr. Parag Chourey, Mr. Sandeep Bansal, Mr. Shubham Choudhary, Mr. Manjit Singh, Mr. Pushpinder Kumar, Mr. Rajat Rajput, Mr. Khalid Bashir and Mr. Rajjan Singh for their constant encouragement, motivation, and camaraderie. Their friendship has made this journey enjoyable and memorable.

This thesis would not have been possible without the support and encouragement of all those mentioned above. Thank you from the bottom of my heart**.**

ABSTRACT

Titanium matrix composites (TMCs) represent a cutting-edge class of materials renowned for their exceptional strength-to-weight ratio, high-temperature resistance, and excellent corrosion properties. The fabrication of TMCs involves embedding reinforcing materials such as ceramic, metallic, or carbon fibers within a titanium matrix through various techniques, including powder metallurgy, solid-state diffusion bonding, and liquid phase sintering. These fabrication methods allow for precise control over the microstructure and properties of the resulting composite, tailoring it to specific applications. The properties of TMCs are highly desirable in numerous industries, including aerospace, automotive, biomedical, and defense. In aerospace, TMCs find extensive applications due to their lightweight nature coupled with high strength, making them ideal for components subjected to high loads and extreme temperatures. In automotive engineering, TMCs offer promising avenues for lightweight, leading to enhanced fuel efficiency and performance. Moreover, in biomedical applications, the biocompatibility of titanium (Ti) combined with the mechanical properties of TMCs make them suitable for implants and prosthetic devices, providing long-term stability and compatibility within the human body. Furthermore, TMCs exhibit remarkable thermal stability and corrosion resistance, rendering them suitable for use in aggressive environments such as chemical processing plants and marine applications.

Recent advancements in the field of TMCs include the development of novel fabrication techniques, optimizing microstructural properties, and exploring hybrid composites combining multiple reinforcing materials. Additionally, computational modeling and simulation advancements have facilitated the design of TMCs for specific applications, further expanding their potential utility across various industries. In conclusion, titanium matrix composites represent a promising class of materials with a wide range of applications and significant potential for further advancements. Continued research and development efforts aimed at optimizing fabrication techniques, enhancing properties, and exploring new applications will undoubtedly propel the utilization of TMCs in diverse fields, contributing to technological innovation and sustainable engineering solutions.

Much work is carried out to develop TMCs using ceramic reinforcements (boron carbide, silicon carbide, aluminum oxide). The densities of most of the ceramic reinforcing materials are higher than Ti/Ti alloy. Therefore, improvement in the mechanical properties of titanium matrix composite (TMC) comes with a slight increase in their density. In addition,

various researchers reported that the high chemical reactivity of titanium at high temperatures makes traditional fabrication techniques unfeasible for the fabrication of TMCs.

Recently, many efforts have been made to use graphene (GR) as a better substitute for ceramic reinforcing material. GR is a 2D carbon material (single atomic layer of sp^2-hybridized carbon atoms) with excellent mechanical, thermal, self-lubrication, low density, and electrical properties. Spark plasma sintering (SPS) is gaining popularity for fabricating TMCs due to its fast heating rates, short sintering time, high densification, and limited grain growth. However, minimal literature on the fabrication of Ti alloy (Ti6Al4V) reinforced with multilayer graphene (MLG) via the SPS process is available. The detailed mechanical, tribological, corrosion, and finishing experimental studies still need to be done.

To address the above stated challenges, in the current work Ti6Al4V/MLG nanocomposites have been fabricated via the SPS process. Detailed experimental studies were performed to study the effect of the input parameters, viz., MLG content and SPS process sintering temperature on the various output responses of the fabricated TMCs. The content of MLG in Ti6Al4V nanocomposites is varied between 0 % to 1.36 %, while sintering temperature varied from 787 °C to 1212 °C. The present work explores the influence of input parameters by investigating fabricated nanocomposites' properties. Microstructural study reveals an in-situ reaction between a carbon source from MLG and Ti from the Ti6Al4V to form a secondary phase TiC. It is evident from the results obtained that MLG plays a vital role in improving the microstructural, mechanical, tribological and corrosion properties of sintered nanocomposites. A detailed parametric study is performed to develop regression equations of the output responses, viz., hardness, elastic modulus, wear rate and corrosion current density (I_{corr}) as a function of input parameters, i.e., sintering temperature and wt. % of MLG. Analysis of variance showed that % contribution of sintering temperature and wt. % of MLG was 42.15 % and 55.40 %, respectively for hardness. Also, the % contribution for the elastic modulus was 49.24 % for sintering temperature and 48.61 % for wt. % of MLG. Maximum value of hardness and elastic modulus achieved for TMCs is 5.37 GPa and 138.90 GPa, respectively. A minimum wear rate of 14.50 x 10^{-6} g/m and I_{corr} of 1.45 1.45 μAcm^{-2}, corresponding to a 54.40 % and 53.82 % improvement compared to bare Ti6Al4V, is achieved for Ti6Al4V /0.8 wt. % MLG fabricated at 1000 °C. In-house developed abrasive flow finishing process setup and abrasive media successfully finished the TMCs with a maximum improvement of 73.20 % in surface roughness.

CONTENTS

LIST OF FIGURES

LIST OF TABLES

LIST OF ABBREVIATIONS

ANOVA	Analysis of variance
AFF	Abrasive flow finishing
ASTM	American Society for Testing and Materials
AMC	Aluminum matrix composite
Al_2O_3	Aluminium oxide
BN	Boron nitride
B_4C	Boron carbide
CIPs	Carbonyl iron particles
CCRD	Central composite rotatable design
CNTs	Carbon nanotubes
COF	Coefficient of friction
CMP	Chemical mechanical polishing
DOE	Design of experiments
DC	Direct current
EDS	Energy Dispersive Spectroscopy
FESEM	Field emission scanning electron microscopy
FMAB	Flexible magnetic abrasive brush
FAP	Ferromagnetic abrasive particles
I_{corr}	Corrosion current density
MRAFF	Magnetorheological abrasive flow finishing
MR	Magnetorheological
MML	Mechanical mix layer
MLG	Multilayer graphene
MMCs	Metal matrix composites
MAP	Magnetic abrasive particles
MRAFF	Magnetorheological abrasive flow finishing
NMAPs	Non-magnetic abrasive particles
PMCs	Polymer matrix composites
PM	Powder metallurgy
RSM	Response Surface Methodology
SiC	Silicon carbide
Si_3N_4	Silicon nitride
SPS	Spark plasma sintering
Ti	Titanium
TiC	Titanium carbide
wt.%	Weight Fraction in %
XRD	X-Ray Diffraction
ZrB_2	Zirconium diboride

LIST OF SYMBOLS

°	Degree
°C	Degree centigrade
μm	Micrometre
g/cm^3	Grams per centimetre cube
mm^3/min.	Millimetre cube per minute
GHz	Giga-Hertz
kN	Kilonewtons
Å	Armstrong
F_R	Radial force
F_A	Axial force
P	Extrusion pressure
σ_{YS}	Yield strength
σ_{UTS}	Ultimate tensile strength
wt.%	Weight fraction in %
HV	Vickers Microhardness
g	Grams
nm	Nanometer
N	Newton
GPa	Gigapascal
MPa	Megapascal
t_m	Thickness of the medium cylinder
d_{im}	Internal diameter of medium cylinder
σ_{dm}	Design stress for medium cylinder
σ_{um}	Tensile strength
d_{om}	Outer diameter of the medium cylinder
L_m	Length of medium cylinder
d_{pm}	Pitch circle diameter
t_{fm}	Thickness of the flange
σ_{dp}	Design stress for piston material
t_{rp}	Thickness of the piston ring
t_{ap}	Axial thickness of the ring
d_{ocr}	Outer diameter of the connecting rod
R_a	Surface roughness
CIPs	Carbonyl iron particles
$\% \Delta R_a$	Percentage change in surface roughness

CHAPTER 1
INTRODUCTION

1.1 Introduction to composites

Over the past few decades, the worldwide development of engineering materials has shown a constant need for growth driven by the ever-evolving demands of technology, industry, and society. Almost all industries require high-performance and lightweight materials with improved mechanical, tribological, and corrosion properties, leading to extensive research and development efforts in the field of composites [1,2]. Composites consist of two or more materials combined to obtain superior properties compared to individual constituents. Each composite constituent retains chemical, physical, and mechanical properties [3]. The two main constituents in a composite are base matrix and reinforcement. The selection and combination of matrix and reinforcement phase are decided by the requirements of a composite for a given purpose, such as improved stiffness, lower density, high temperature performance, improved tribological properties, etc. The reinforcement should be uniformly distributed in the matrix to promote homogeneity in material properties (e.g., strength and stiffness). Metals, ceramics, and polymers are all examples of matrix materials that can be used in composites. Reinforcements are generally used as fibers, sheets/laminates, whiskers, or particles. The commonly used reinforcements are oxides, carbides, and nitrides of various materials (e.g., SiC, Al_2O_3, B_4C, Si_3N_4, BN, etc.). Recently, researchers employed carbon, graphite, and glass fibers as reinforcements in their studies. The nomenclature of a composite is decided by the base matrix, i.e., whether the composite is metal based (i.e. metal matrix composite), polymer based (i.e. polymer matrix composite) or ceramic based (i.e. ceramic matrix composite).

1.2 Introduction to metal matrix composites

Metal matrix composite (MMC) typically contains metal as their base matrix, adding them with various reinforcements such as ceramics and carbonaceous materials. MMCs have been shown to have great potential for the next generation of building materials. These composites involve the incorporation of various reinforcements into a metal matrix to enhance the metal's mechanical properties. The absence of a certain amount of strength and stiffness necessary in structural materials motivated the development of MMCs [4]. This deficiency is made up for by the addition of reinforcement that is either ceramic or particulate into the metal matrix. MMC's capability of combining the properties of metals with other metals/ceramics, etc., has been the center of attraction for engineers, designers, and manufacturers. Their excellent properties, like specific strength, modulus, wear resistance, etc., have widened their applications for various engineering and structural purposes [5]. MMCs are a viable replacement for conventional materials, particularly in the automotive, aerospace, medical, and defense sectors [6,7]. MMCs are further differentiated based on the metal matrix chosen, such as aluminum composites, magnesium composites, copper composites, and titanium composites.

1.2.1 Aluminum composite

Aluminum matrix composite (AMC) is a material that is developed using aluminum as the matrix material, and various reinforcing components are used to enhance specific qualities. These composites can be used in a wide variety of applications. These composites have been developed by considering the lightweight nature of aluminum in addition to improving properties like strength, stiffness, thermal conductivity, wear resistance, and several other characteristics. Kumar et al. [8] fabricated nickel powder reinforced Al-7075 composites and reveled that the physical, mechanical and tribological properties were improved as compared to its counter part. Mohanvel et al. [9] compared pure aluminum to zirconium di-boride (ZrB_2) reinforced AMCs, revealing improved tribological and mechanical properties. ZrB_2 has a high hardness and wear resistance, contributing to the improved composite's mechanical (tensile strength and elastic modulus) and wear resistance. However, adding excessive ZrB_2 particles can adversely affect the composite's ductility and fracture toughness. Chen et al. [10] fabricated AMCs reinforced with carbon nanotubes (CNTs) and aluminum oxide (Al_2O_3). The ball milled powder was consolidated through a spark plasma sintering (SPS) process followed by hot extrusion. In contrast, previous researchers reported improvement in the tensile strength and elastic modulus of the AMCs but at the cost of decreased tensile strain to fracture. However, in the reported literature, the presence of CNTs improves the primary strengthening of the composites, while Al_2O_3 enhances dimple fracture.

1.2.2 Magnesium composite

Magnesium based composites enhance characteristics by combining magnesium with ceramic, metallic, or polymer reinforcement. They reduce weight, improve mechanical qualities, and increase thermal stability. Aerospace, automobile, sports, electronics, and biomedical industries use magnesium composites. The researchers optimized the processing methods and materials for their practical application. Say et al. [11] concluded that CNTs have the potential to significantly improve the mechanical and corrosion properties of magnesium matrix composites. The composite's tensile strength and hardness can be enhanced by increasing the CNT ratio. However, this may result in a reduction in the material's ductility. In addition, increasing the ratio of CNTs in the composite can improve its resistance to corrosion by producing a protective layer on the material surface. Agglomeration and restricted dispersion can be caused by an excessive amount of CNTs, which decreases the material's resistance to corrosion and mechanical characteristics. Dinaharan et al. [12] studied different processing methods that affected the microstructure and wear resistance of fly ash-reinforced AZ31 magnesium matrix composites. The desired composites were fabricated using stir casting as well as powder metallurgy. According to the findings, the composites fabricated through powder metallurgy had a more uniform microstructure than those made through stir casting. Furthermore, the composites made through powder metallurgy had finer grain sizes and uniform particle distribution. Similarly, the wear resistance of composites made using powder metallurgy was significantly higher than that of those made using stir casting. Overall, the processing method significantly impacted the improvement in various properties of the fly ash-enhanced AZ31 magnesium matrix composites.

1.2.3 Copper composite

The unique features of copper-based composites have made them popular as highly advanced materials. These composites use copper as the matrix and ceramic particles, metallic additives, carbon-based fillers, and polymers as reinforcement. This synergistic integration improves mechanical, thermal, electrical, and corrosion resistant properties, making copper composites appropriate for many applications. Copper composites are growing in electronics, aircraft, automotive, energy, and industrial equipment. Chen et al. [13] concluded that adding graphene to copper matrix composites improved its microstructural characteristics and mechanical properties. Similar findings were reported that graphene addition could improve strength, stiffness, thermal conductivity, and wear resistance [14]. However, the ductility and hardness of the material decrease by adding an excessive amount of graphene. Overall, the appropriate graphene content depends on the application being researched and the balance that must be struck between enhancing mechanical properties and preserving ductility and toughness. Tjong and Lau [15] exhibited improved tribological properties by reinforcing SiC into the copper matrix. The size, shape, volume fraction, and distribution of the SiC particles play an important role in determining the tribological behavior of these composites. Also, testing conditions (load, sliding speed) determine such properties. Moreover, the sliding mechanism also determines tribological behavior.

1.2.4 Titanium composite

Titanium-based composites combine titanium (Ti) as the primary matrix or base material with other reinforcing substances to obtain specific properties and improve upon existing ones. Titanium-based composites have several desirable properties, including a high strength-to-weight ratio, superior corrosion resistance, and biocompatibility. These characteristics make titanium-based composites appealing for use in a variety of industries. By varying the nature, concentration, and orientation of the reinforcement components, it is possible to modify the performance of these composites to fulfill various specific performance criteria.

Titanium and its alloys are currently the subject of significant scientific attention for diverse uses, including the biomedical, aerospace, and automotive industries [16]. These materials have a low overall weight and generally possess desirable qualities such as high specific strength, good corrosive resistance, and excellent biocompatibility [17,18]. Compared to steel and nickel alloys, titanium has a lower Young's modulus, a lower wear resistance, and a lower heat resistance [19]. To overcome these shortcomings, researchers have focussed on fabricating TCMs in the past decade. Moreover, the results obtained from their research validate that the TMCs have the potential to overcome the current shortcomings of the various industrial sectors.

The most common technique used to fabricate such TMCs is powder metallurgy. Pan et al. [20] reinforced TiC into a titanium matrix to study the microstructure and tribological properties. By varying the processing inputs, it is possible to regulate the shape, size, and dispersion of these TiC particles. The addition of TiC particles enhances the TMCs' tribological characteristics. The composites exhibit enhanced wear resistance, frictional characteristics, and high-temperature stability. The high hardness and thermal stability of TiC particles, which can serve as a barrier against wear, are principally responsible for the composites' wear resistance. Wozniak et al. [21] studied the microstructural and mechanical properties of 2-dimensional Ti_2C sheets reinforced into silicon carbide matrix composites. Compared to the base sample, the fracture toughness and hardness of the composites with 1.5 wt. % of reinforcement is significantly improved.

1.3 Strengthening mechanism in metal matrix composites

The strengthening in MMCs is mainly attributed to reinforcements. The reinforcements incorporated in matrices result in strengthening due to various mechanisms, some of which are as follows:-

- Hall-Petch effect: This is the strengthening resulting from the refinement in grain size and the strength of the composite increases with the increase in the piling up of dislocated grain boundaries.
- Enhanced dislocation density: This is achieved by increasing the dislocation density, which occurs due to thermal mismatch. A thermal mismatch pertains to the difference in the base matrix's thermal expansion coefficients and reinforcements.
- Solid solution strengthening: This is achieved by adding solute atoms from another element to the base metal. Due to this, the dislocations undergo slow/obstructed movements in the crystal lattice of the metal, thus strengthening the matrix [22].

1.4 Introduction to powder metallurgy

Powder metallurgy (PM) is a solid-state process wherein the composite is developed by mixing different metal powders of required composition along with the reinforcement, followed by consolidation. PM technique is usually carried out in the following sequence, first, the blending of powders of a base matrix with the reinforcing phase followed by cold pressing of the blend to obtain green compacts. Second, these green compacts are strengthened by various processes, viz., direct sintering, hot isostatic pressing, hot extrusion, etc. PM is generally considered an efficient way of developing high-quality products with near-net shape, material utilization, and shape complexity. The detailed methodology for carrying out the various steps of the PM process is as follows:-

1.4.1 Production of powder

Several methods are used for the production of powder. Some of them are listed below.

- Gas atomization
- Water atomization
- Plasma atomization
- Centrifugal atomization
- Plasma spheroidization

1.4.2 Powder blending

Powders of the matrix and dispersed phase are mixed thoroughly using various techniques such as mortar pestle, tumbling action, double cone mixer, etc. The powders are mixed with lubricants such as metallic stearates, stearic acid, stearin, or other organic compounds. The lubricant is added for smooth compaction and ejection of the green compact by reducing friction between the die walls and powder particles.

1.4.3 Compaction

Mixing powders is followed by compaction, which includes pressing the powders in a die by applying high pressures. After compaction, powder particles are cold welded. These cold welds give sufficient strength to the compact, known as green strength, and the compact is known as green compact. The compaction carried out may be uni-axial, bi-axial, and iso-static

1.4.4 Sintering

Sintering is the application of thermal energy to develop density controlled products from powders of metals, ceramics, etc. It is a heat treatment process of a green compact to impart strength and integrity. The temperature at which sintering is performed is always less than the temperature at the melting point of the principal constituent of the material. The sintering process aims to produce parts with the desired and reproducible microstructure by controlling sintering parameters. The desired microstructure refers to controlled density, grain size, and distribution of different phases. Sintering can be classified mainly into two categories, i.e., solid state and liquid state sintering. The solid state sintering occurs when the green compact is densified to a solid state at the sintering temperature. Solid state sintering occurs in two stages, as shown in Fig. 1.1. There is neck formation between adjacent particles at the initial stage, followed by pore rounding and pore shrinking in the second stage. The bulk volume of the sintering particles undergoes shrinking in both stages, i.e., a decrease in the center-to-center distance of the particles in the first stage and pore volume shrinkage in the later stage. In the case of solid state sintering of heterogeneous materials, alloy formation occurs only at the neck. Liquid phase sintering occurs when one of the constituents of the composite exists in the liquid phase, as shown in Fig. 1.2. The compact is prepared from heterogeneous powders, as shown in Fig. 1.2(a). Due to the capillary action, the liquid phase infiltrates between the solid grains, as shown in Fig. 1.2(b). The bonds developed during sintering are dissolved by the liquid phase and cause grain refinement. Further, a larger contact area develops between the solid and liquid phases, leading to the alloying process Fig. 1.2 (c). The liquid phase disappears if its quantity is less than its solubility in the solid phase.

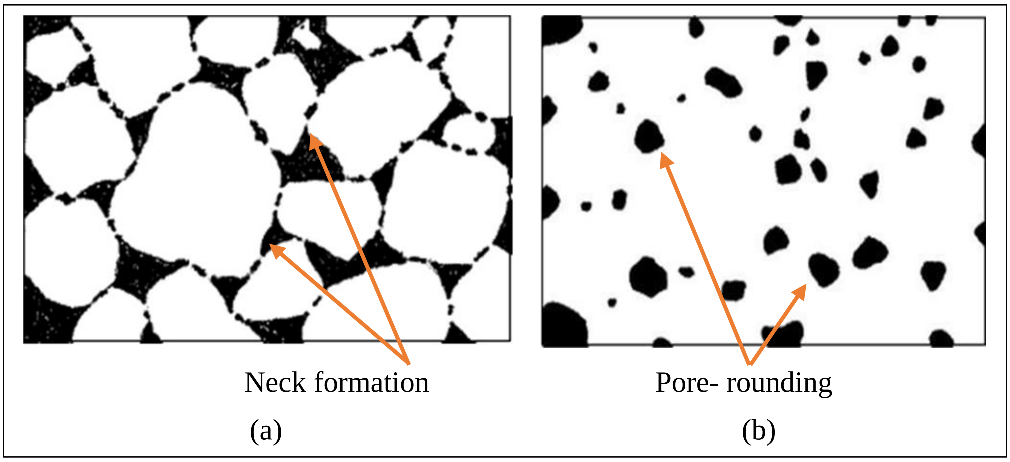

Fig. 1.1 (a) Solid state sintering- 1st stage **(b)** Solid state sintering- 2nd stage [23].

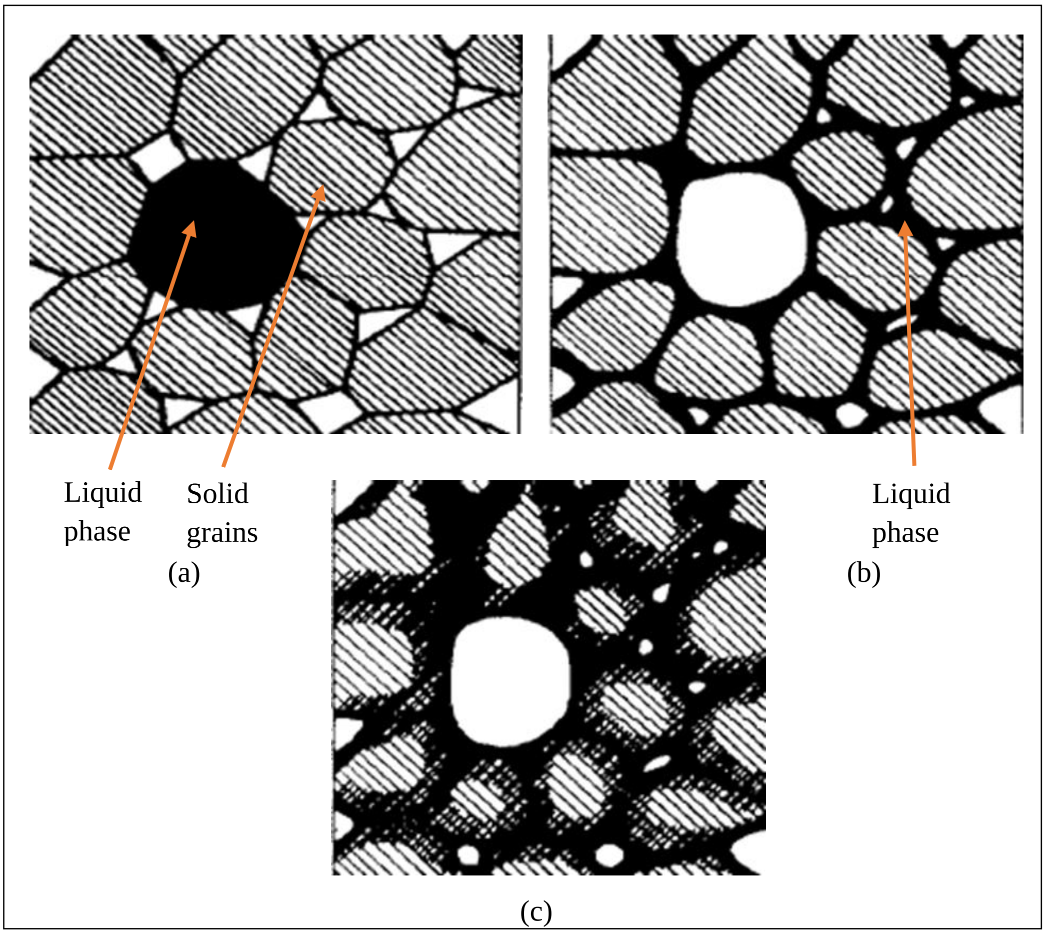

Fig. 1.2 (a) Liquid state sintering- 1st stage **(b)** Liquid state sintering- 2nd stage **(c)** Liquid state sintering- 3rd stage [23].

Since the evolution of the PM technique, which is used to fabricate TMCs, several ways were developed to sinter the green compacts. Some of them are discussed below.

1.4.4.1 Conventional sintering

During the conventional sintering process, heat is transported from one object to another by traditional procedures, i.e., employing three transfer mechanisms: conduction, convection, and radiation. The material's surface is first heated in conventional heating, and then the heat penetrates further into the material. This indicates that there is a difference in temperature between the surface and the interior of the object. By heating a compact to around 2/3rd of its melting temperature, this sintering process consolidates particles into a more uniform structure (this temperature would allow for significant atomic movability and is often used as a reference to determine the parameters necessary for sintering). Fig. 1.3 shows the schematic of the conventional sintering process.

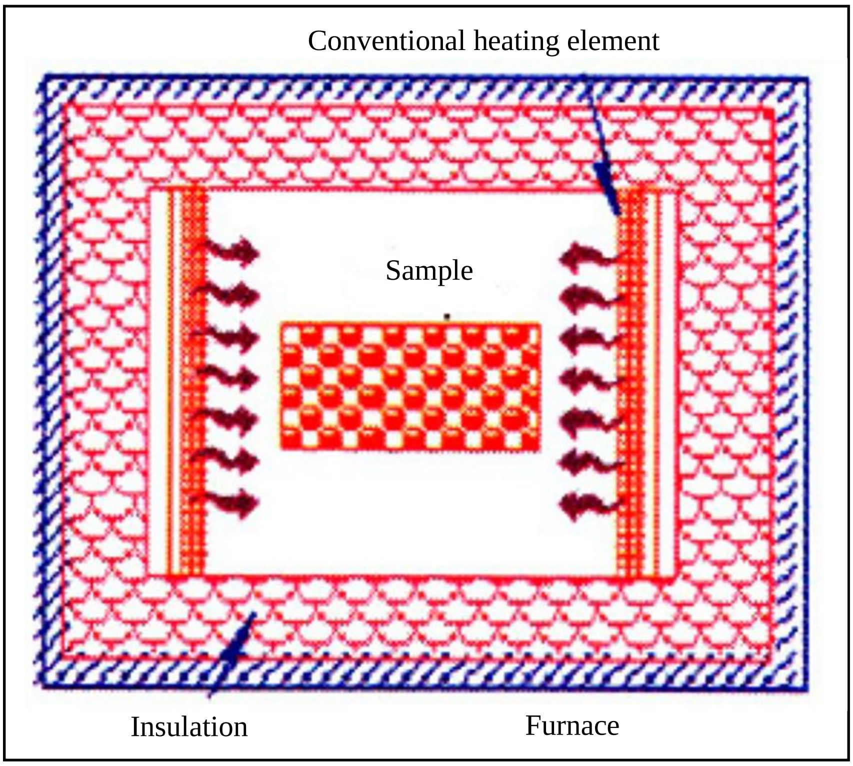

Fig. 1.3 Schematic diagram of the conventional sintering process [24].

1.4.4.2 Microwave sintering

Microwave sintering is an advanced sintering process for fabricating dense structures. This innovative method uses microwave heating, which converts electromagnetic energy into thermal energy. The electromagnetic waves that make up microwaves have a specific frequency, 2.45 GHz microwaves are frequently used in research and industry. Microwaves that penetrate a substance cause mobility in independent and bound charges, including ions and electrons. Electromagnetic radiation causes this motion, which breaks the material's natural equilibrium and thus raises its temperature. The direction of heat flow is the main distinction between microwave and conventional sintering methods. Fig. 1.4 shows the microwave sintering process.

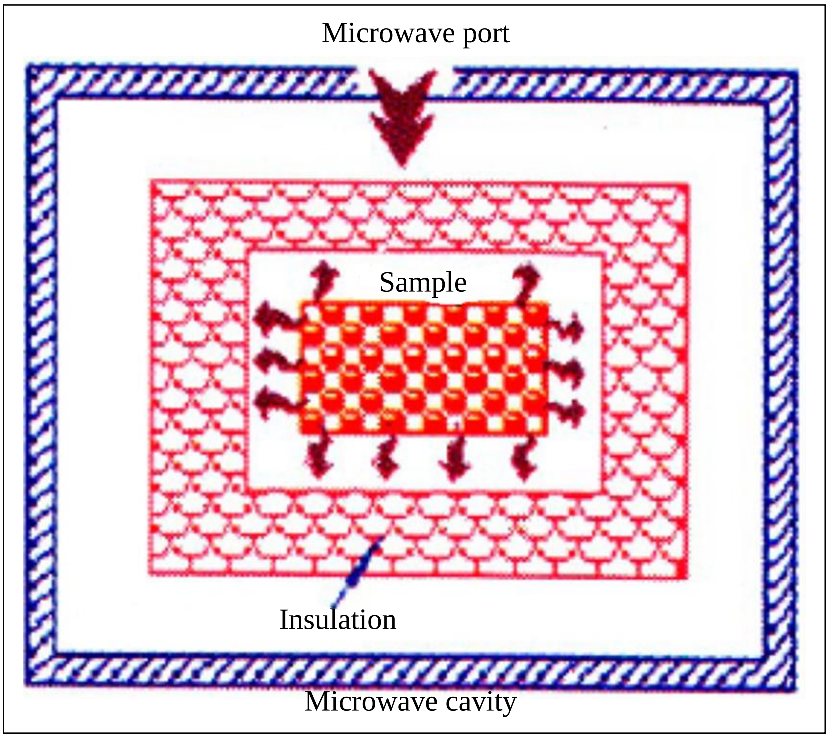

Fig. 1.4 Schematic diagram of the microwave sintering process [24].

1.4.4.3 Spark plasma sintering

Spark plasma sintering (SPS) is a novel technique developed to consolidate metal powders into sintered products. The schematic of the equipment is shown in Fig. 1.5. It consists of a vacuum chamber in which the blended powders are loaded into the punch and die assembly. The mechanical assembly is also connected to a DC pulse generator. No separate compaction is required for the process. The metal powders are directly fed into the sintering furnace, and the simultaneous application of high energy DC pulse and modest pressure of < 100 MPa leads to good activation and consolidation of the metal powders. Joule heating of powders is provided through low voltages, which produce high currents. The heat is more quickly transferred to the metal powders, even if it is a non-conductive powder. The pulse pattern with pause durations can be defined explicitly for the process. The pulse duration followed is generally in the order of a few milliseconds. A high sintering rate of up to 300 °C/min. has been used to investigate the sintering behavior of different metal alloys. Thus, the process gets completed within a few minutes.

Densification of the powder compact occurs by simultaneously applying mechanical load in the order of 50 to 250 kN. The sintering process is generally carried out under vacuum conditions but can also be done under a protective gaseous atmosphere. Later, the sintered parts are moved to a water-cooled chamber. The temperature in the process is measured using thermocouples or pyrometers. As the DC pulse is generated, spark discharge appears in the contact points between the particles and the gaps between them. This results in a momentary high temperature of the order of several thousand degrees. Due to this local high temperature, the surface of the particles is subjected to evaporation and melting. To achieve a homogeneous sintering behavior of the part, the temperature within the specimen should be at a minimum. The parameters that influence the temperature variations inside the sample are the material's electrical conductivity, die wall thickness, and the graphite papers placed between the specimen and the die [25].

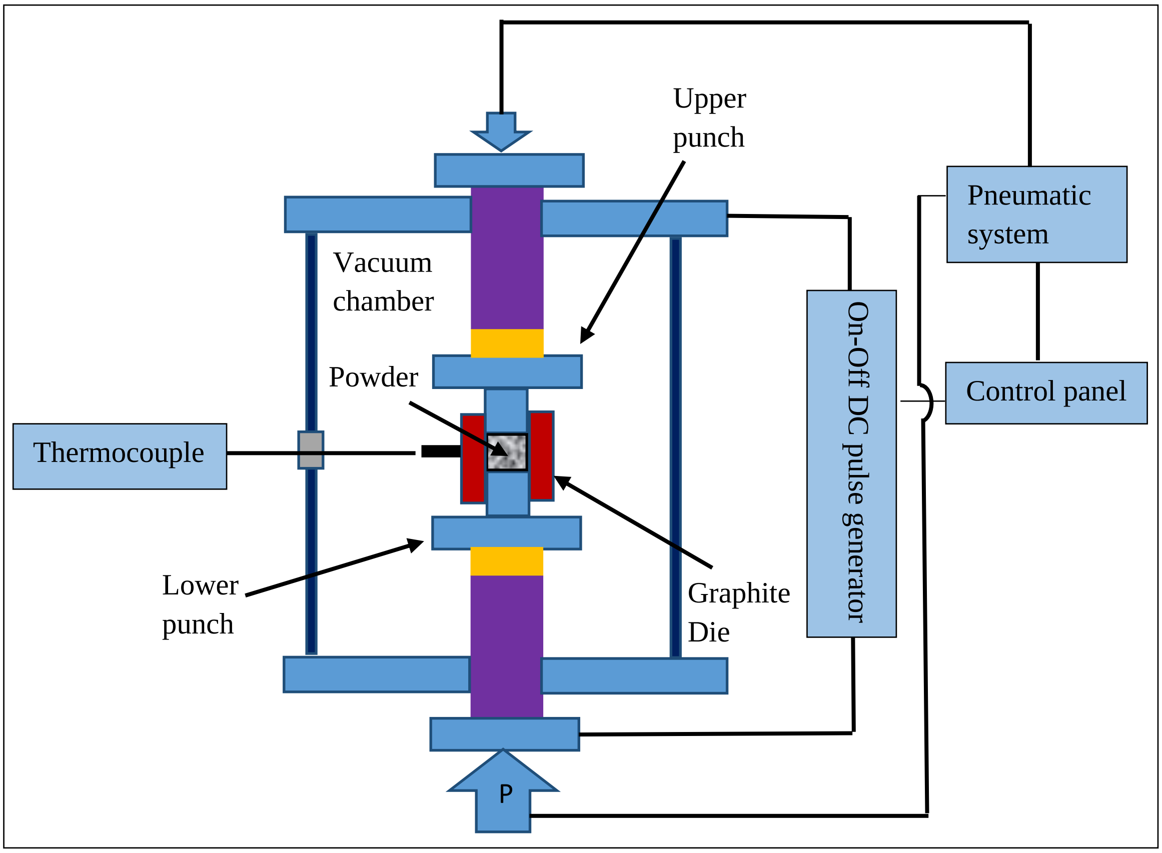

Fig. 1.5 Schematic diagram of the spark plasma sintering process.

1.5 Introduction to finishing

Finishing is the most complex machining process carried out in the manufacturing sector. The cost of finishing operations accounts for up to 15 % of the overall machining cost throughout a manufacturing cycle [26]. Surface roughness plays a vital role in deciding the component's mechanical, tribological, and corrosion properties. Various traditional and advanced techniques have been employed in the past to improve the surface finish of components. Some of them are discussed below:

1.5.1 Chemical mechanical polishing process

The chemical mechanical polishing (CMP) process is characterized by the simultaneous application of chemical and mechanical forces (Fig. 1.6). An initial chemical reaction occurs between the workpiece's surface and the silica slurry. The chemical reaction's byproducts are later eliminated by mechanical abrasion. The wafer containing abrasive particles (silica sols) is spun against the polishing pad and pressed down forcefully in order to shear any residual roughness peaks and remove reaction products. On titanium dioxide thin film, CMP has the ability to achieve a surface roughness of approximately 1.16 Å [27].

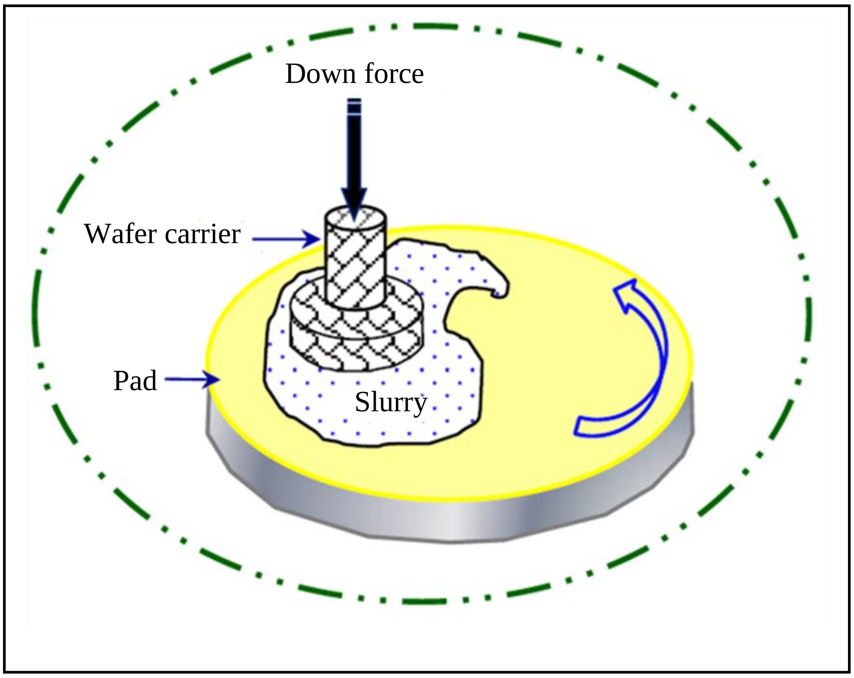

Fig. 1.6 Schematic diagram of the chemical mechanical polishing process.

1.5.2 Magnetic abrasive finishing

Finishing with magnetic abrasives was explicitly developed to finish large, flat workpieces made of materials that are difficult to machine. During this procedure, ferromagnetic particles and fine abrasive particles (such as diamond or SiC) are mixed to form ferromagnetic abrasive particles (FAP or magnetic abrasive particles-MAPs). As seen in Fig. 1.7, a magnetic field is applied across the gap between the workpiece and electromagnet to perform the finishing process. When a magnetic field is applied to the gap, it causes the formation of a flexible magnetic abrasive brush (FMAB) by magnetic alignment particles (MAPs). The dipole-dipole attraction between MAPs' magnetic poles along magnetic field lines is the source of this phenomenon. The abrasive particles become trapped within the interlocking chains of FMAB. FMAB functions as a multi-point cutting tool for removing the surface roughness peaks from the workpiece surface through shearing. [28].

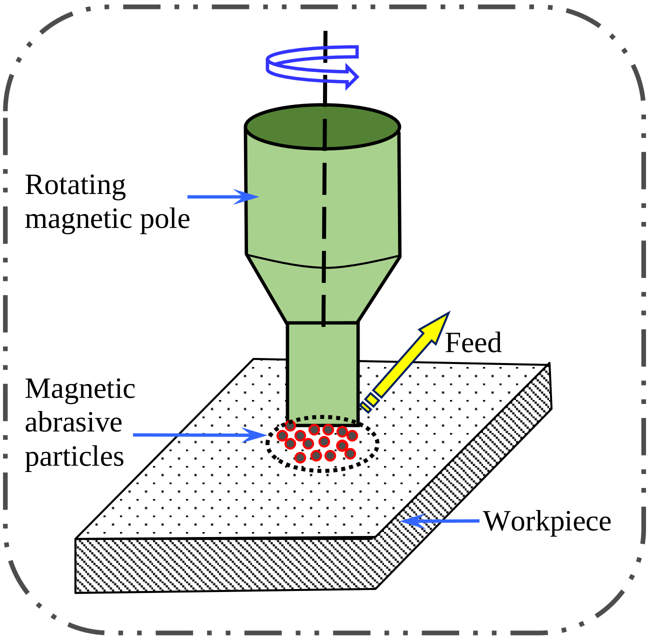

Fig. 1.7 Schematic diagram of magnetic abrasive finishing process.

1.5.3 Abrasive flow finishing

The abrasive flow finishing (AFF) process is a non-traditional finishing procedure that is relatively new and is used to obtain a high surface quality, especially on the complex featured components made of difficult-to-finish material. AFF is becoming increasingly significant as a result of its capacity to produce results that are predictable, repeatable, and consistent [29]. A viscoelastic substance infused with abrasive particles is passed through the surface of the workpiece that is being finished using AFF. The abrasive effect of AFF is comparable to operations like grinding, lapping, and polishing. As the media is extruded down the restricted pathway of the workpiece, it transforms into a self-forming mass, taking on the form of the workpiece as it goes. This facilitates the finishing of both simple and complex geometric components.

The AFF process mainly comprises the following four elements:-

1. AFF process setup: The AFF setup is designed in such a manner that it could meet the requirements of the workpiece being finished. The primary components of the AFF process setup include medium cylinders, hydraulic cylinders, a fixture, and a power supply (hydraulic and mechanical). The arrangement of these components might be either vertical or horizontal, depending on the specific task requirements and manufacturing convenience [30].
2. Tooling: Tooling is employed to hold the workpiece in a fixed position and guide the abrasive to specific places, either to control the flow in regions where abrasion is intended or to obstruct the flow in parts that should stay unchanged (Fig. 1.8(a)). The design should ensure a firm hold on the workpiece and allow for the controlled insertion and removal of the abrasive media.
3. Media: Using an appropriate AFF media is crucial in achieving the desired surface finish of a workpiece. The composition of the media primarily consists of a viscoelastic base polymer, along with additives such as plasticizers, softeners, and abrasive particles. Fig. 1.8(b) demonstrates that the application of extrusion pressure (P) to the media leads to the creation of radial force (F_R) due to the elastic component of the media. In contrast, the viscous component generates axial force (F_A). As a pliable adhesive, the base polymer and other additives hold abrasive particles in place and transfer pressures created in the media to the active abrasive particles. While F_A drives the indented abrasive particle in the axial direction to reduce surface roughness by microploughing or microcutting, F_R is responsible for the indentation of abrasive particles into the workpiece's surface. [31].

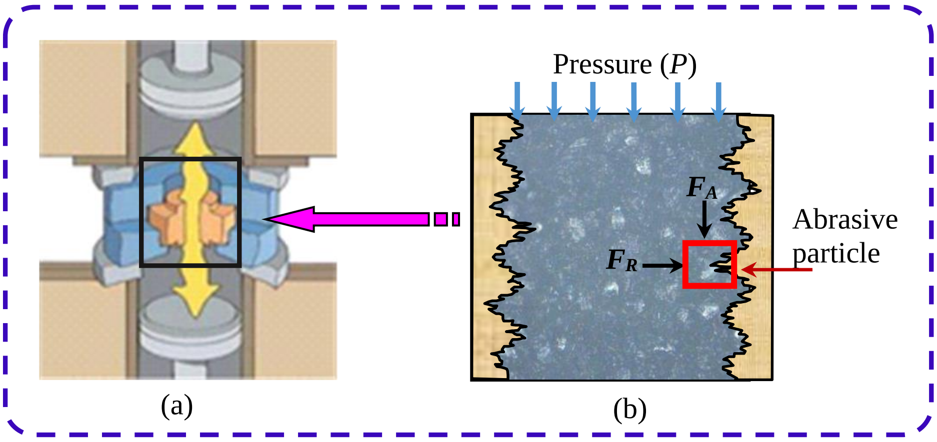

Fig. 1.8 Schematic showing **(a)** Tooling and **(b)** Various finishing forces acting on the media during its extrusion through the workpiece passageway.

4. Workpiece: The significance of the AFF process resides in its ability to finish components comprising soft aluminum, tough carbides, and ceramics with simple to intricate geometries [32].

Fig. 1.9 shows the AFF setup with its major components. During the working of the AFF process, the workpiece that needs to be finished is kept firmly in place within the tooling, and then it is positioned within the gap created by the upper and lower medium cylinders. When it comes to the process of extruding the media, the medium cylinder's primary responsibility is to both confine and direct the media during the reciprocating motion of the piston. At the beginning of each new AFF cycle, the lower medium cylinder is typically loaded with abrasive media, while the top medium cylinder is either empty or very close to being so. The media is extruded through the confined path under the operation of an external force, which may be hydraulic or mechanical. Once the lower medium cylinder has released its media, it transfers it to the upper medium cylinder. Subsequently, the upper medium cylinder piston initiates the process of pushing the media back into the lower medium cylinder. This constitutes one complete cycle of the AFF process. The media is extruded back and forth through the workpiece until the desired level of surface roughness on the workpiece surface is attained.

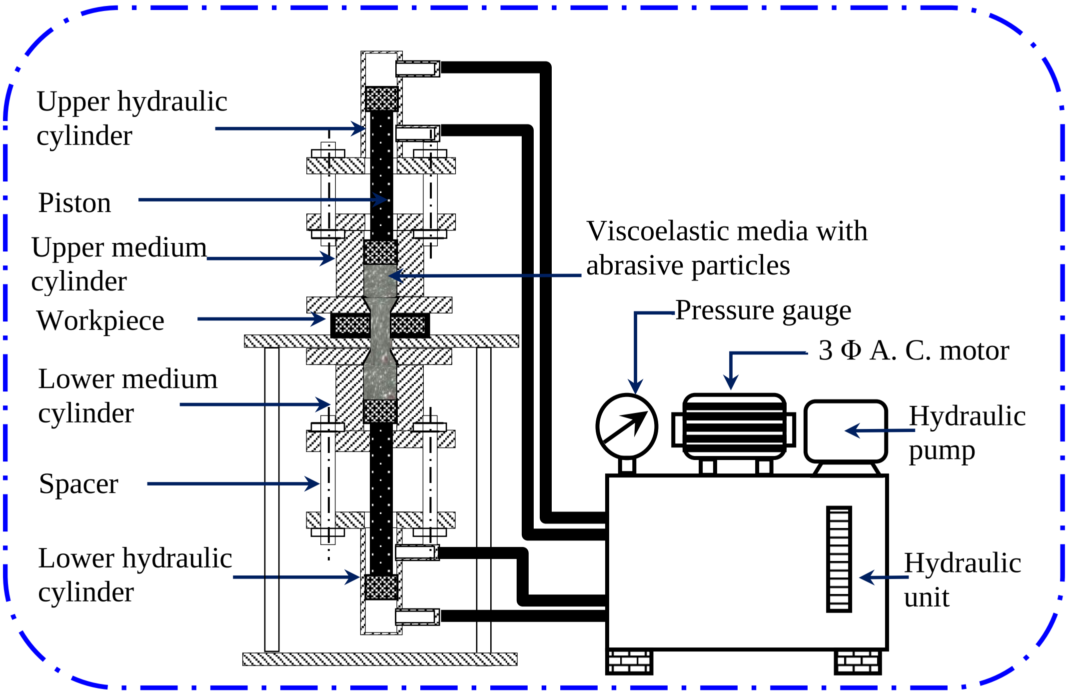

Fig. 1.9 Schematic diagram of abrasive flow finishing process [33].

1.5.4 Magnetorheological abrasive flow finishing

A schematic of magnetorheological abrasive flow finishing (MRAFF) is shown in Fig. 1.10. MRAFF is a method that is very similar to AFF in the sense that it extrudes the abrasive media through or past the workpiece surface. However, it uses magnetorheological (MR) fluid instead of employing normal abrasive media. The fluid consists of micron-sized magnetizable particles, non-magnetic abrasive particles (NMAPs), and a non-magnetic carrier media such as silicon oil, water, or mineral oil. When MR fluids are applied, the magnetizable particles form a columnar structure with abrasives between the chains. Shearing peaks from the surface of the workpiece occur as the MR fluid is extruded back and forth through the passageway of the workpiece fixture.

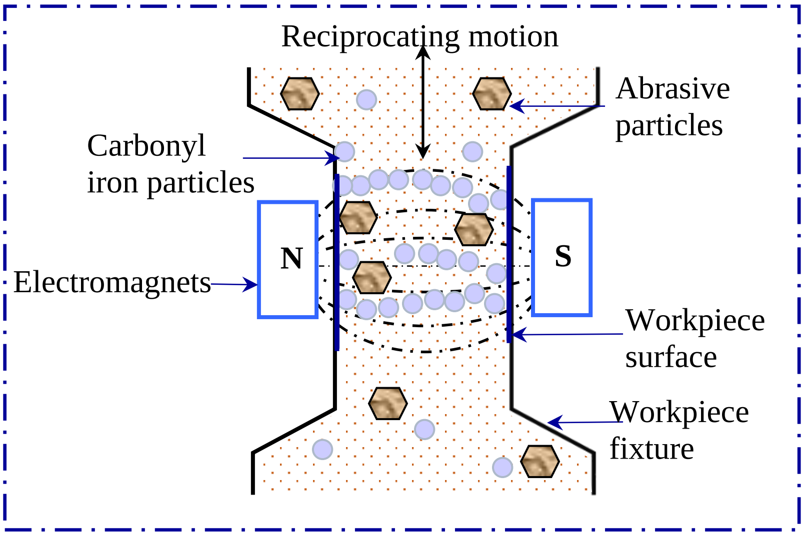

Fig. 1.10 Schematic diagram of the magnetorheological abrasive flow finishing process.

CHAPTER 2

LITERATURE REVIEW

MMCs have seen substantial development over the years, with various materials and fabrication methods continually developed to enhance their qualities and broaden the variety of applications for which they may be used. In the past, several types of reinforcement have been reinforced in the metal matrix, majorly with silicon carbide (SiC), titanium carbide (TiC), boron carbide (B_4C), aluminum oxide (Al_2O_3), etc. [34]. In the past decade, the need for the use of titanium has grown due to its potential physical, mechanical, wear, and corrosive properties. So, researchers have started to focus on titanium-based composites. The developed TMCs find application in various applications (aerospace, automotive, defense, biomedical). These composites were able to replace existing super alloys in those application areas.

Further, the researchers started to focus on the advancement of fabrication techniques. In recent times, continuous efforts have been made to improve the fabrication process of these TMCs. Overall, the advancement of TMCs has been driven by a mix of developments in reinforcing materials and fabrication techniques, as well as an enhanced understanding of the fundamental scientific and technical concepts that govern the properties of TMCs. Moreover, surface finishing plays a vital role in various industrial sectors. Also, it improves the functionality and lifespan of the composites by improving their multiple properties. Therefore, researchers in the past have focussed on the various finishing processes. The conventional finishing process doesn't adequately address the current industrial requirement. Thus, advanced finishing processes have recently been developed. In the present chapter a detailed literature survey has been carried out about the recent developments in the evolution of TMCs. A summary of the surface finishing techniques of various composites has also been discussed in the present chapter.

2.1 Mechanical properties of titanium matrix composites

Over the years, efforts are been made to improve the mechanical properties of the TMCs. However, with continuous increases in the industrial demand, further improvement in the mechanical characteristics of these TMCs erupts. As stated above, the development of reinforcing material and fabrication techniques has been the highlight of improving the functionality of TMCs. Therefore, ceramic-based reinforcement was introduced in the titanium matrix, and various researchers reported improvement in their findings. **Li et al.** [35]

investigated the microstructure and mechanical properties of titanium matrix composites reinforced by in-situ synthesized TiC-TiB. Significant improvements were recorded for the fabricated TMCs. These improvements included greater yield strength levels (σ_{YS}) and ultimate tensile strength (σ_{UTS}). Quantitatively, the value of σ_{YS} and σ_{UTS} of the TMCs increased by 89.3 % and 74 % compared to bare titanium. However, the increase in the tensile properties was at the expense of losing the ductility of the titanium composites. **Lagos et al.** [36] reveal a unique method for the preparation of reinforcement (TiC) using self-propagating high-temperature synthesis (SHS). Ti and C are cold pressed into a stainless steel die in this method. After a foam structure is formed, it is crushed and sieved. Reinforcement with 5 wt.% and 10 wt.% has been added to the Ti6Al4V powder and compacted using SPS. The density obtained for the sintered composites was more than 99 % compared to the theoretical density. The mechanical results show that the composite with 10 wt. % of TiC has increased the ultimate tensile strength and Young's modulus by 14 % and 15 %, respectively. **Pouzet et al.** [37] studied the grain refinement and mechanical properties of B_4C reinforced Ti6Al4V composites fabricated using direct metal deposition (DMD). The hardness of the composite with 12 wt. % TiB was 455 HV, which was 26.38 % higher than that of the unreinforced sample. At 500 °C, a 7.79 % increase in the tensile strength was recorded for 1.5 wt.% of B_4C. However, loss in the ductility for the composite was also reported, which could be revealed with the help of an SEM image of the fracture surface. **Falodun et al.** [38] used SPS to synthesize Ti6Al4V/TiN composites. TiN reinforcement was added to the matrix in the volume fraction of 1 % to 5 %. The incorporation of TiN resulted in the formation of new hard phase Ti_2N into the composites. The value of hardness increases with the addition of TiN into the matrix due to the formation of a hard phase and uniform distribution of TiN into the matrix. Similarly, **Sribalaji et al.** [39] **and Liu et al.** [40] incorporated WC mixed with TiC and SiC nanowires into titanium and reported enhancement in fabricated composites' physical and mechanical properties. Further, researchers observed that the tensile and hardness of the TMCs show some improvement. However, it is at the cost of hampering other properties (density, ductility). Researchers have started using carbonaceous reinforcement in the titanium matrix to solve this issue. Incorporating these reinforcements results in the overall improvement in the mechanical properties of the TMCs.

A strong transition interface is required to form a strong bond between the matrix and CNTs. The interaction between the CNTs and metal is mechanically bonded without interfacial reactions, where the bonding force is mainly dependent on wettability between CNTs and the matrix. Such bonding is relatively weak due to the difference in surface energy between the matrix and reinforcement [41]. To overcome this problem, researchers explored graphene and its different structural forms to fabricate composites. **Wei et al**. [42] tried to overcome the above-stated issue by reinforcing CNTs along with graphene oxide into the titanium matrix.

Over time, various developments in fabrication techniques have been done to consolidate these TMCs. Traditional ingot metallurgy techniques cannot be used to produce TMCs. **Kondoh et al.** [43] concluded that the high chemical reactivity of titanium at high temperatures makes traditional fabrication techniques unfeasible for the fabrication of TMCs. **Yang et al.** [44] synthesized TMCs with various wt. % of graphene using microwave sintering. The compressive strength of the composite with 0.2 wt.% of graphene shows improvement while it decreases with a further increase in graphene content to 0.4%**.** This is due to agglomeration and a further decrease in the aspect ratio of graphene. **Cao et al.** [45] reinforced graphene into Ti6Al4V to form TMCs where 0.5 wt.% of graphene was blended into the titanium matrix. The composites were consolidated using hot isostatic pressing followed by isothermal forging. Adding graphene nanoflakes (GNFs) at a weight fraction of 0.5 considerably increased the tensile strength (12.31%) and yield strengths (20.11%) of the composite material without negatively impacting its ductility.

Munir et al. [46] revealed in their study that the SPS is the most effective process to preserve composite material characteristics during sintering. In their study, the authors reinforced multi-walled carbon nanotubes (MWCNTs) into a pure Ti matrix. **Mu et al.** [47] studied the interfacial structure and tensile properties of the multilayer graphene (MLG) reinforced Ti fabricated by SPS. The mechanical results show a two-fold increase in the tensile strength value of TMCs with 0.2 wt. % MLG when compared with bare Ti. The interfacial strength of the TMCs was due to the partial reaction of TiC with the MLG. **Mu et al.** [48] further increased the concentration of MLG to 0.8 wt. %. The consolidated samples reveal an increase of 98 % in the tensile strength compared to bare Ti. Also, a 16 % increase in elastic modulus value was reported. **Gürbüz et al.** [49] studied the various effects of sintering parameters involved in the fabrication of graphene nanoplates (GNPs) reinforced pure titanium matrix. GNP′s content of 0.15 % wt. % exhibits results with density (4.36 g/cm^3) and harness (566 HV). Compared to pure Ti (304 HV), an increase in the hardness of 86.18 % was reported. **Lu et al.** [50] and **Mu et al**. [51] successfully overcome the ductility problem in TMCs by incorporating GNPs as reinforcement. The results show an increase in the strength without losing the ductility of the TMCs.

2.2 Wear of titanium matrix composites

In addition to the mechanical properties of the TMCs, wear also plays an important role in their use in various applications. A considerable number of studies have been carried out in recent times to improve the TMC′s wear characteristics. Similar to mechanical properties, various authors started studying the wear properties of ceramic-based TMCs and found positive results. **Prakash et al.** [52] studied the tribological properties of B_4C reinforced TMCs and concluded that with the addition of reinforcement into the Ti6Al4V matrix, its properties enhanced. The wear rate for 10 wt.% of B_4C at 5 N load was approx. 6.5×10^{-7} mm^3/min. while that of unreinforced titanium was 8×10^{-7} mm^3/min. Significant improvement in the coefficient of friction (COF) was also observed for the TMCs. **Attar et al.** [53] produced Ti/TiB composites using selective laser sintering (SLS) route. In their study, they indicated parameters such as the ratio of hardness to reduced modulus and yield pressure to determine the wear resistance of the composites. The ratio of hardness to reduced modulus and yield pressure for the Ti and Ti/TiB composite was 0.025, 0.002 GPa, 0.030, and 0.004 GPa, respectively. The conventional wear test aligned with the anticipated wear pattern, as the weight loss for Ti, measured 0.055 g, whereas that of the Ti/TiB composite was 0.021 g. **Namini et al.** [54] reinforced TiB_2 reinforcement into a pure Ti matrix consolidated by the SPS process. Due to the formation of in situ TiB, an enhanced hardness of the composite was reported. Across all temperature ranges, composite reinforced with TiB_2 shows improved wear characteristics compared to sinter Ti. This is due to the formation of a stable oxide layer in the composite case. Also, hardness plays a major role in improving the wear resistance of the composites. **Saba et al.** [55] studied the effect of various particle sizes of reinforcement (diamond powder) on the tribological properties of the sintered TMCs. Among all the TMCs reinforced with particle size (5 nm, 100 nm, 200 nm, and 3 µm), one with 5 nm particle size shows excellent wear resistance. The wear rate drastically decreases for 5 nm particle size compared to the sintered Ti. However, the wear rate tends to increase as the particle size increases. It was because 5 nm reinforcement could interact with dislocations better than other reinforcement and enhance the mechanical characteristics of the TMC.

Rominiyi et al. [56] revealed that adding nickel (Ni) into Ti could improve the wear resistance of the TMCs. Among all the fabricated TMCs, 10 wt.% of Ni shows the lowest COF. Across all the loading conditions, wear resistance was highest in Ti/10 wt. % Ni. The formation of intermetallic phases Ti_2N and TiN_2 helps to improve the wear resistance in TMCs. **Izui et al.** [57] revealed the tribological behavior of the TMCs reinforced with titanium carbonitrides ($TiC_{0.3}N_{0.7}$, $TiC_{0.7}$ $N_{0.3}$). The TMCs with 10 wt.% of $TiC_{0.3}N_{0.7}$ show the best results among all the samples. Moreover, TiCN rich in nitrogen shows better results than TiCN rich in carbon. The authors also compared both matrix (Ti and Ti6Al4V) and found that Ti shows significant improvement in the wear resistance compared to Ti6Al4V. **Alaneme et al.** [58] investigated the wear properties of the Ti-Nb_2O_5 composites consolidated by SPS. The COF for the TMCs varied in the range of 0.3 - 0.6. The wear resistance increases with the increase in the content of the Nb_2O_5. Most of the wear on sintered TMCs was caused by adhesive and abrasive wear mechanisms. **Ma et al.** [59] concluded that TiC ceramic can improve the wear resistance of the Ti6Al4V alloy. The TiC reinforcement was varied from 0 - 50 wt. % in the step of 10, and it was found that with increasing content of TiC, the wear mass loss decreases. The increase in the wear resistance is due to the rise in the hardness of the TMCs. Compared to Ti6Al4V, TiC with 50 wt. % into the matrix, reduces wear loss by 45.9 %. **Selvakumar et al.** [60] further improve the wear volume for TiB-reinforced TMCs. They revealed that the TMC's wear volume was 0.4368 mm^3 while the wear rate was 0.000276 mm^3 /m. Significant improvements were observed for TMCs with a TiB content of 38.5 wt. %. **Xiong et al.** [61] produced Ti_3AlC_2 and TiC phases using Ti, Al, and C, which were used as reinforcements for Ti-6.5Al-2Zr-1Mo-1V (TA 15). Addition of 1 wt. % of Ti_3AlC_2 into TA 15 decreases the friction coefficient by 20.95 %. This improvement was due to the formation of an oxide layer of the phases. **Jin et al.** [62] attempted to improve the wear resistance of the Ti using TiB_2 as reinforcement fabricated via. SLS. An increase in the wear resistance of 32.6 % was reported for TMCs with 7.5 wt.% of TiB_2 compared to fabricated Ti.

Kumar et al. [63] also reported an increase in the wear resistance of the TMCs reinforced with TiB_2. The increase in wear resistance was achieved using ceramic reinforcement but at the cost of increasing the overall weight of the TMCs. This disadvantage of TMCs restricts their use in various sectors where weight plays an important role. **Song et al.** [64] reported the disadvantage of using ceramics in titanium-based composites. They emphasize that the ceramics reinforcement usually has higher densities than the Ti and Ti alloys. Adding such reinforcement leads to improved wear resistance but at the cost of increased weight of the TMCs. To counter this problem, researchers have started focusing on various alternatives to ceramics. Due to their various popular characteristics, researchers explored carbonaceous reinforcement. **Cao et al.** [45] revealed that TMCs reinforced with these carbonaceous nanomaterials lead to the formation of in-situ TiC, which acts as the load bearer and thus improves the composites' COF and wear resistance properties. Using the SPS process, **Yu et al.** [65] reinforced GNPs into Ti/6Al/2Sn/2Zr/3Mo/1Cr/2Nb/Si (TC21). As the amount of GNPs in the matrix increases, the hardness of GNP/TC21 composites also increases. Also, with the addition of 0.05 wt.% of GNP's reinforcement, the wear loss was decreased by 21 % compared to sintered TC21. **Gürbüz et al.** [66] investigate the mechanical properties and tribological behavior of pure titanium at different concentrations of graphene. Composite with 0.15 wt.% of graphene shows the highest compressive and tensile strength with an improvement of 29 % and 48 %, respectively. Compared to sintered pure titanium (5×10^{-5} mm^3/Nm), the composite with 0.15 wt. % graphene had the lowest wear rate (2.86×10^{-5} mm^3/Nm) at 10 N load.

2.3 Corrosion of titanium matrix composites

Various electrochemical studies were performed to investigate the performance of TMCs in corrosive environments. However, few researchers have focused on studying the corrosion properties of TMCs fabricated via. SPS process. **Anawati et al.** [67] examined the corrosion resistance of Ti- hydroxyapatite composites fabricated using mechanical alloying (MA) and SPS process. Potentiodynamic polarization studies revealed that Ti composites with 0-10% HA had better corrosion resistance than commercially pure Ti (CP-Ti). Increasing HA content (20-30 %) reduces corrosion resistance due to crater-like flaws caused by ceramic particle separation. **Prakash et al.** [68] targeted orthopedics applications by fabricating Ti-Nb(50-x)-HA(x) (x = ¼ 0,10,20 wt %) composites using rapid microwave sintering. Due to the presence of HA reinforcement in the composites, new phases were developed, such as $Ca_3(PO_4)_2$, Ti_5P_3, and CaO. As a result of these phases the corrosion resistance of the fabricated composites improves. An increase in the MA time considerably reduced defect density and enhanced corrosion resistance. Ti-HA composites show potential for biomedical implants due to the formation of a nano-HA layer in bioactivity tests in simulated bodily fluid.

Fojt et al. [69] studied the corrosion properties of Ti-39Nb composites fabricated with different porosities (5 %, 15 %, 24 %, and 33 %) using isostatic pressing at 400 MPa. They concluded that when the TMCs have a 15 % or above porosity, there is a greater risk of experiencing a localized corrosion attack. The behavior of materials with porosity lower than 15 % was analogous to that of a compact alloy when it came to corrosion. While exposing samples with different porosities to an atmosphere containing fluoride ions, a discernible localization of the corrosion process was seen and documented. In addition, macrocells formed on porous materials significantly impacted the material's corrosive behavior. **Yilmaz et al.** [70] produced different porous Ti16Nb composites varying between 4.05 % and 60.79

% using press conventional sintering at 1200 ℃. It was revealed that increasing porosity decreased corrosion resistance due to increased surface area exposed to the electrolyte, heterogeneous oxide film, or insufficient oxide film thickness caused by the difficulty of electrolyte penetration between porosities. **Wang et al.** [71] used the SLS process to produce TMCs with Ti and Nb as starting material, followed by heat treatment. Due to the enhanced chemical homogeneity that can allow the homogenous development of titanium oxides and niobium oxides, heat treatment can further improve the corrosion resistance of as-sintered Ti-35Nb samples. TMCs were showing promising results as compared to their unreinforced counterpart. **Gu et al.** [72] successfully developed TiO_2/Ti-35Nb-2Ta-3Zr anti-corrosion composites with varying TiO_2 particle concentrations using friction stir processing (FSP). The findings demonstrate that the TiO_2/Ti-35Nb-2Ta-3Zr composite has uniform β grains with homogeneous diffuse oxygen on the surface. Composite layers showed reduced passive current density (2.1 A/cm^2) and corrosion current density (22.85 nA/cm^2) with a wider passive range than the substrate.

Mordyuk et al. [73] improve the corrosion resistance of Ti6Al4V by employing a protective layer of alumina powder on its surface. According to the polarization tests in a 0.9 % NaCl medium, the coating has lower corrosion rates and greater corrosion potential than the bare Ti6Al4V alloy, suggesting improved corrosion resistance. Compared to the air-oxidized Ti6Al4V alloy surface, the composite coating's linear polarization resistance, *Rp*, is 7.5 times more, and its protective efficiency is 4-fold. **Zhou et al.** [74] employed the SLS process to fabricate Ti-5wt.% TiN composites The fabricated composite exhibits better corrosive properties than fabricated CP-Ti. In contrast to CP-Ti, the Ti-5 wt% TiN composite exhibits lower corrosion current densities. The Ti-5 wt.% TiN composite has more excellent corrosion resistance than the CP-Ti, even if the immersion period is prolonged to 15 days.

Khiabani et al. [75] studied the corrosion resistance of reduced graphene (rGO) and titanium dioxide (TiO_2) coating on titanium substrate. It was observed through electrochemical measurement of *Rp* via a potentiodynamic polarisation test that there was a substantial increase from 1.88×10^{-5} to 195.3×10^{-5} Ωcm² as the quantity of rGO nanosheets rose to 0.5 gL^{-1}. The Mott-Schottky analysis showed that the integration of rGO nanosheets significantly reduced the donor concentration of the samples. These results demonstrated that adding rGO nanosheets into TiO_2 coatings considerably improved their ability to resist corrosion, indicating a considerable corrosion barrier effect of the coatings. **Singh et al.** [76] reinforced GNPs into HA coatings, which were sprayed on Ti6Al4V substrate. The electrochemical behavior of the coated sample was studied in the simulated body fluids. Adding 1 wt.% and 2 wt.% of GNPs significantly decreased the corrosion rate by 67 % and 87 %, respectively.

2.4 Finishing of titanium matrix composites

Various researchers finished MMCs using a magnetic-based finishing process. **Singh et al.** [77] investigated the potential to achieve precise surface topography on TiNbTaZr (TNTZ) alloy for orthopedic applications using the MRAFF process. Various input parameters such as carbonyl iron particles, (CIPs), rotational speed of tool (N_t), and work gap (G_p) were varied at different levels. The output response, i.e., surface roughness (R_a), is influenced by process variables CIPs, N_t, and G_p with a contribution of 9.39 %, 85.57 %, and 1.12 %, respectively. **Shi et al.** [78] established that with the employment of shot peening (SP) and vibrational finishing (VF) to TC 17 composites, the fatigue strength was improved by 26.7%. **Ghosh et al.** [79] solved the problem of traditionally used MR fluid, i.e., the weaker bonding between CIPs and diamond abrasives, which hinders the transmission of shear force for hard material finishing, leading to poor material removal rate (MRR) and uneven surface polishing. MR fluid was integrated with chemical etchants that create an oxide layer, resulting in a higher finishing rate than conventional MR fluid. **Tian et al.** [80] finished Ti6Al4V using MAF, where the authors used multiple pole tips on the finishing tool. Significant improvement upto 0.073 µm from 1.195 µm in the R_a value was achieved. The finishing parameters used to attain these results were 900 rpm spindle rotational speed and 160 rpm rotary table speed with a working gap of 0.7 mm. The total improvement in the R_a value accounts for 94 %. **Parameswari et al.** [81] studied the effect of MRF process parameters on the percentage change in R_a. It was revealed that the overall polishing rate was significantly influenced by the surface roughness of the original workpiece, R_a (about 61%). The concentration of abrasives followed behind, accounting for around 33% of the total. Achieving a minimum R_a value of 0.049 µm was quite noteworthy. In the finishing processes employing magnets (permanent, electromagnetic), a non-uniform magnetic field results in the uneven distribution of finishing forces over the workpiece surface. As a result, surface roughness obtained on the finished surface is non-uniform. The AFF process overcomes such shortcomings.

Sankar et al. [29] investigate the MRR during the finishing of the AMCs using the AFF process. The SiC reinforced AMCs were finished to a minimum R_a value of 0.25 ± 0.05 µm from an initial value of 0.6 ± 0.1 µm. Optimize parameters for the finishing process were also concluded, such as extrusion pressure (6 MPa) and wt.% of processing oil (10 wt.%). **Mali et**

al. [82] employed the Taguchi method to study the R_a properties of Al/15 wt.% SiC MMCs. In their research, it was established that abrasive mesh size and wt. % of abrasive particles are the most important parameters influencing R_a and were improved by nearly 80 %. **Sankar et al.** [31] developed a new media (styrene polymer (SP), plasticizer (hydrocarbon processing oil), and abrasive particles (SiC with mesh size 220) for finishing AMCs using AFF. The authors concluded that the change in surface roughness (ΔR_a) for 10 wt.% reinforcement is higher than that of AMCs finished with 15 wt.% of reinforcement. The experimental data shows that the ΔR_a increases with increasing media viscosity and begins to decrease with increasing plasticizer. **Sankar et al.** [83] concluded that media plays a vital role in defining the final R_a of AMCs among all the process parameters. Their research concluded that the wt.% of soft styrene polymer is mainly responsible for determining the ΔR_a. **Sushil et al.** [84] finished the rough surface obtained after the EDM process. They varied the wt.% of reinforcement (SiC) from 20 % to 60 %. MRR in the finishing operation was varied between 1.9 and 9.3×10^{-6} g/s. The range of ΔR_a values was between 0.40 and 1.70. **Sudhakara et al.** [85] finished Al7075/SiC MMCs fabricated via the stir casting process. The effect of extrusion pressure on MRR and R_a was studied. The authors reported that with the increase in the extrusion pressure and wt.% of SiC, the MRR increased, and the R_a value decreased. A similar trend was observed for the number of cycles.

2.5 Research gaps

Titanium and its alloys find their vast application in the aerospace, automobile, and biomedical industries but still need attention to meet the ever-increasing demand for improved material properties and life span. In recent decades, the powder metallurgy route for fabricating titanium metal matrix composites has evolved. Recently, a few researchers have developed and studied MLG based titanium composites by SPS process with improved mechanical and tribological properties. However, some areas of improvement and limitations based on the literature review are discussed below:-

1. MLG plays a vital role in improving the mechanical properties of Ti6Al4V. However, limited work has been done to study the mechanical, tribological, and corrosion characterization of Ti6Al4V/MLG nanocomposites fabricated using the SPS process.
2. Minimal work shows the detailed parametric study investigating the individual and interactive effect of sintering temperature and wt. % of MLG on the mechanical, tribological, and corrosion properties of Ti6Al4V.

3. The published work does not report the finishing of the Ti6Al4V/MLG nanocomposites by the abrasive flow finishing (AFF) process.

2.6 Objectives of the present research work

Based on the exhaustive literature review, the following are the broad objectives of the current research work:-

1. To fabricate the graphene-reinforced titanium metal matrix composites using the SPS process.
2. To investigate the effect of various process parameters on the mechanical properties of sintered composites, such as hardness and elastic modulus. To study the characterization of fabricated composites via SEM, XRD, EDS, etc.
3. To study the wear and corrosion of sintered composites under various process parameters.
4. To study the surface roughness of composites finished by the AFF process.

2.7 Organization of thesis chapters

Chapter 1 gives the introduction of the various matrix composites. Also, in this chapter, a detailed discussion about TMCs is carried out. The various techniques to fabricate TMCs (conventional and advanced) and their application were discussed explicitly.

Chapter 2 discusses the existing literature review about the various mechanical, tribological, corrosion, and finishing properties of TMCs. This literature reports the advancements and gaps that motivated the current thesis work. The research objectives of the present work are reported at the end of this chapter.

Chapter 3 discusses the steps involved in the fabrication of TMCs, and also this chapter highlights various testing methodologies involved in carrying out the present research work. Lastly, this chapter discusses the design of the in-house developed abrasive flow finishing setup.

Chapter 4 discusses the parametric results of various input parameters (sintering temperature and wt.% of MLG) on the output responses (hardness, elastic modulus, wear rate, and corrosion current density). Also, this chapter deals with the effect of various input parameters of abrasive flow finishing (no. of cycle, wt.% of abrasive particle, and mesh size of the abrasive particle) on the surface roughness profile of the sintered nanocomposites.

Chapter 5 provides the conclusions and significant outcomes from the present research work and defines the scope for future work.

CHAPTER 3

METHODOLOGY

3.1 Introduction

This chapter deals with the detailed methodological procedure followed to accomplish the research objectives. In accordance with the research objectives, this chapter starts with the fabrication technique employed for consolidating TMCs. After that, various characterization (microstructural, physical, mechanical, tribological, and finishing) methods were discussed in detail.

3.2 Fabrication of titanium matrix composites

The following section discusses the detailed selection procedure of raw materials followed by the steps involved in consolidating TMCs using those raw materials.

3.2.1 Material selection

The material selection was based on the exhaustive literature review carried out while considering the recent trends and needs of industrial sectors. Recently, titanium and its alloys have been extensively in demand for their wide use of applications in various sectors. Therefore, Ti6Al4V (Ti64) was chosen as the base matrix for developing the TMCs. As mentioned in the previous chapter (Chapter 2: Literature review), most studies focus on exploring ceramics as reinforcement. Also, some of them highlighted the potential of graphene as reinforcement to improve the properties of the TMCs. Therefore, multilayer graphene (MLG) was taken as the reinforcement for the present work. The physical and elemental composition of the Ti6Al4V and graphene powders is given in Table 3.1, and the SEM images for the same are shown in Fig. 3.1.

Table 3.1 Physical properties and elemental composition of powders.

Powder	Physical properties		
	Average particle size (µm)	Thickness (nm)	No. of Layers
Ti6Al4V	30	-	-
MLG	5 (Diameter)	2.5	4

Powder	Elemental composition (wt. %)							
	Ti	Al	V	Fe	O	N	H	C
Ti6Al4V	87.6-91	5.5-6.75	3.5-4.5	≤0.40	≤0.20	≤0.050	≤0.015	
MLG	-	-	-	-	-	-	-	100

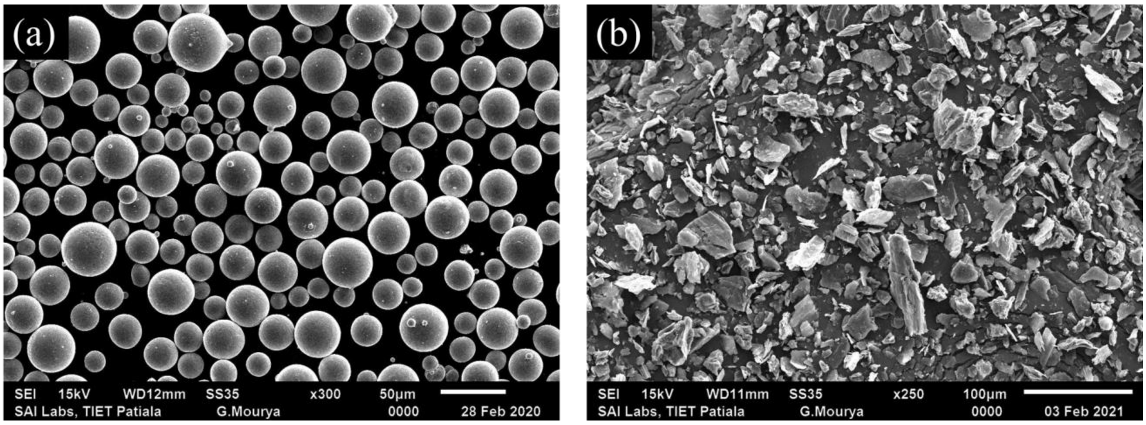

Fig. 3.1 SEM images of **(a)** Ti6Al4V and **(b)** MLG powders.

3.2.2 Mixing of raw powders using a ball milling apparatus

To harness the true potential of reinforcement, i.e., MLG, it was necessary to disperse the MLG uniformly into the titanium matrix. Many researchers have reported that the mechanical ball milling process is an effective method for the uniform dispersion of the reinforcement into the matrix. Therefore, the present work employed a ball milling apparatus to distribute MLG uniformly into Ti6Al4V. Fig. 3.2 shows the image of the ball milling apparatus facility present at Thapar Institute of Engineering and Technology, Patiala.

Fig. 3.2 Ball milling apparatus, Courtesy: TIET, Patiala.

The required powders were mixed proportionately with steel balls in the ball milling apparatus for 8 hrs. The ball-to-powder ratio was taken as 5:1. Fig. 3.3 shows the mixed powder's SEM image with its area mapping. It is clear from the area mapping images that the MLG reinforcement was uniformly dispersed into the Ti6Al4V matrix.

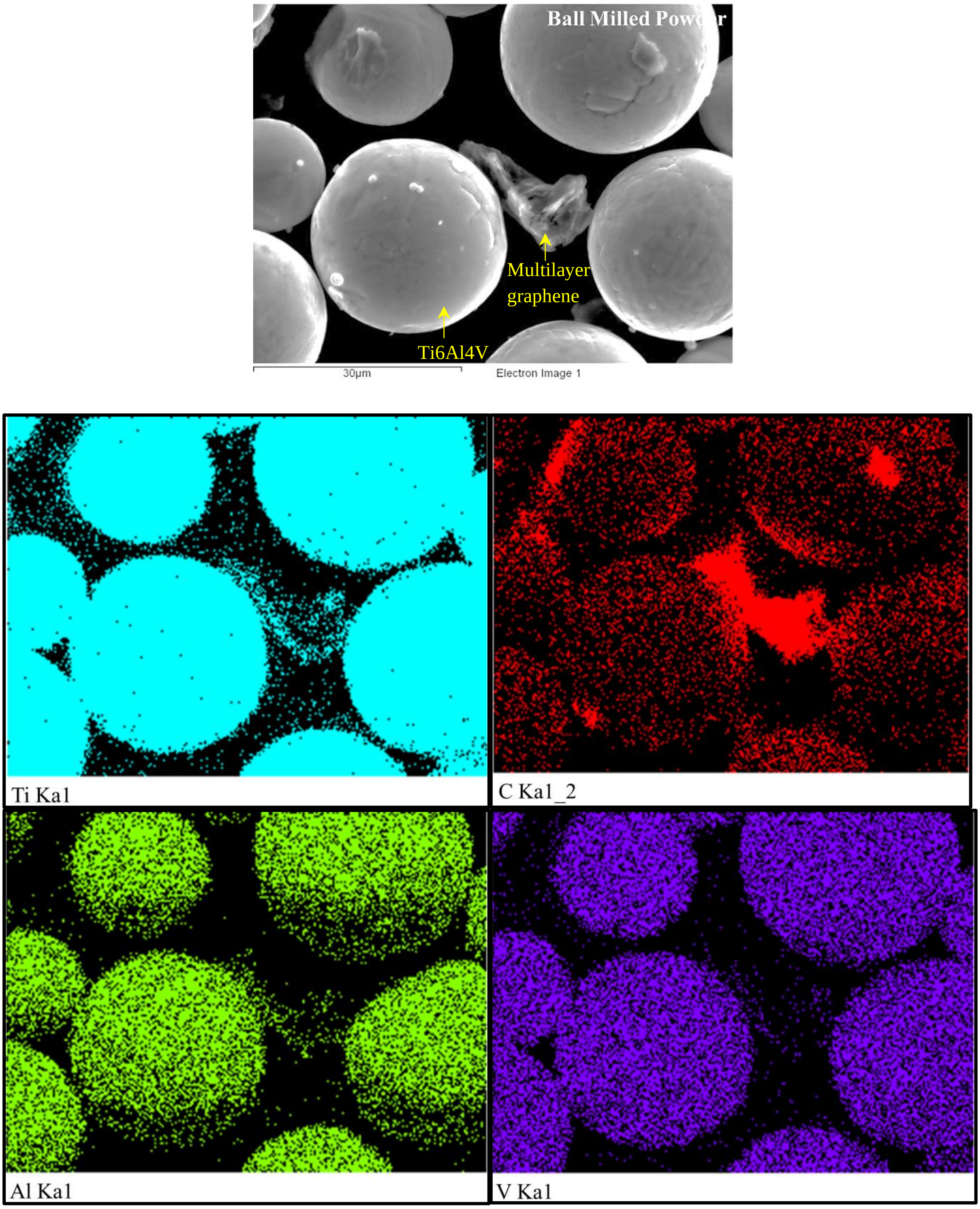

Fig. 3.3 SEM image and area mapping of mixed powder containing Ti6Al4V and multilayer graphene.

3.2.3 Consolidation using spark plasma sintering

The consolidation of Ti6Al4V nanocomposites was done using the SPS process (Model SPS-625, SPS Syntex INC., Japan), as shown in Fig. 3.4. The ball-milled powder was put into a high density graphite die (Ø25.5 mm × 60 mm) and consolidated at different input sintering temperatures. The heating rate for the SPS process was 100°C / min., and the pressure applied for the sintering was 50 MPa with 5 minute holding time in a vacuum chamber.

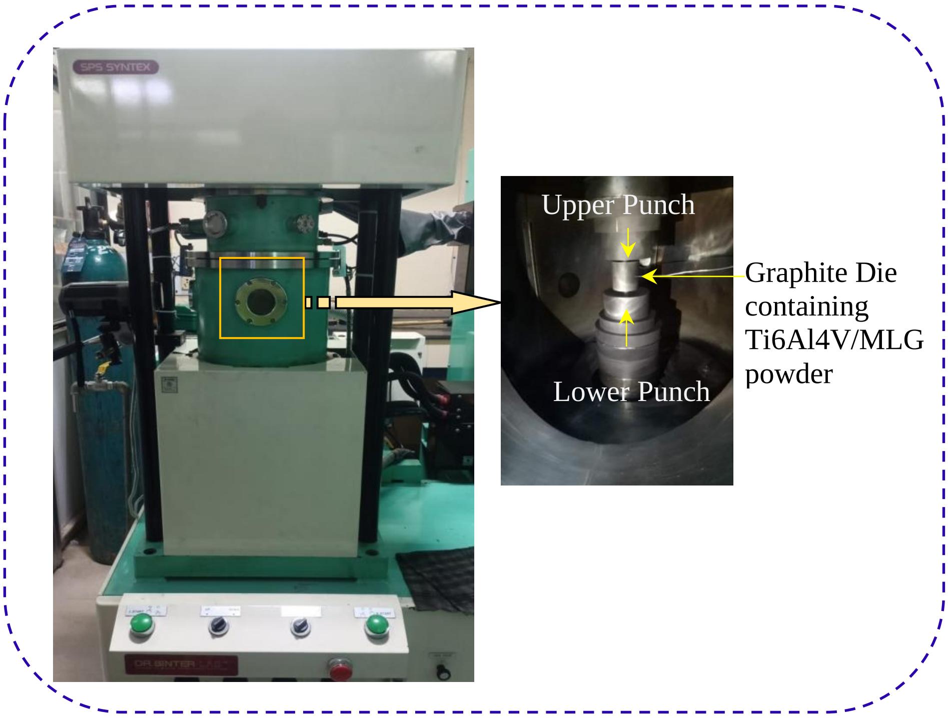

Fig. 3.4 Image of the spark plasma sintering setup, Courtesy: IIT, Kanpur.

3.3 Design of abrasive flow finishing setup

3.3.1 Design methodology

An AFF experimental setup has been developed by keeping the process's primary mechanism and basic needs as the base. Strength criteria were utilized throughout the design process for various essential components, along with key design ideas and some assumptions. The vital components of the AFF setup are the hydraulic cylinder, medium cylinder, piston, and workpiece fixture. Before designing the setup, the following are some design considerations that were taken to calculate the specifications of various components:-

1. The setup is under static loading.
2. The individual weights of the components are not taken into account.
3. The setup design was done with strength as the primary criterion.

In addition, the following criteria serve as the foundation for the design of the entire setup:

1. Maximum working pressure: 12 MPa.
2. Maximum stroke length is 140 mm.
3. The inner diameter of the medium cylinder is 40 mm.

3.3.2 Medium cylinder

The medium cylinder is responsible for storing an adequate quantity of the abrasive media. Secondly, it directs the media through the workpiece fixture past the workpiece surface using the piston's extrusion pressure-induced motion. The medium cylinder performs both of these significant roles. Since the medium cylinder is fabricated via casting, it contains few casting defects. Also, the inner surface over which the media slides is very rough. To overcome such problems, stainless steel cylindrical liners are used at the medium cylinder's inner surface. The material for the medium cylinder was grey cast iron with an ultimate tensile strength $\boldsymbol{\sigma}_{um}$ of 150 MPa (as per IS 210: 1993). The factor of safety, *FS,* is taken as 5. A high factor of safety is to address its non-homogeneous nature.

Thickness of medium cylinder

The thin cylinder theory is used to calculate the thickness of the medium cylinder. The equation that governs the thickness in thin cylinder theory is [86]:-

$$t_m = \frac{Pd_{im}}{2\sigma_{dm}} \tag{3.1}$$

where,

t_m = medium cylinder's thickness

P = internal pressure on the cylinder, 12 MPa

d_{im} = medium cylinder's internal diameter, 40 mm

σ_{dm} = design stress for medium cylinder

Now, σ_{dm} is given as:-

$$\sigma_{dm} = \frac{\sigma_{um}}{FS} \tag{3.2}$$

$$= \frac{150}{5} = 30 \text{ MPa}$$

So, equation 3.1 gives t_m as:-

$$t_m = \frac{12 \times 40}{2 \times 30} = 8 \text{ mm}$$

Now, the total thickness of medium cylinder = t_m + thickness of stainless steel liner + thickness for reconditioning

$$= 8 + 1 + 3.5 = 12.5 \text{ mm}$$

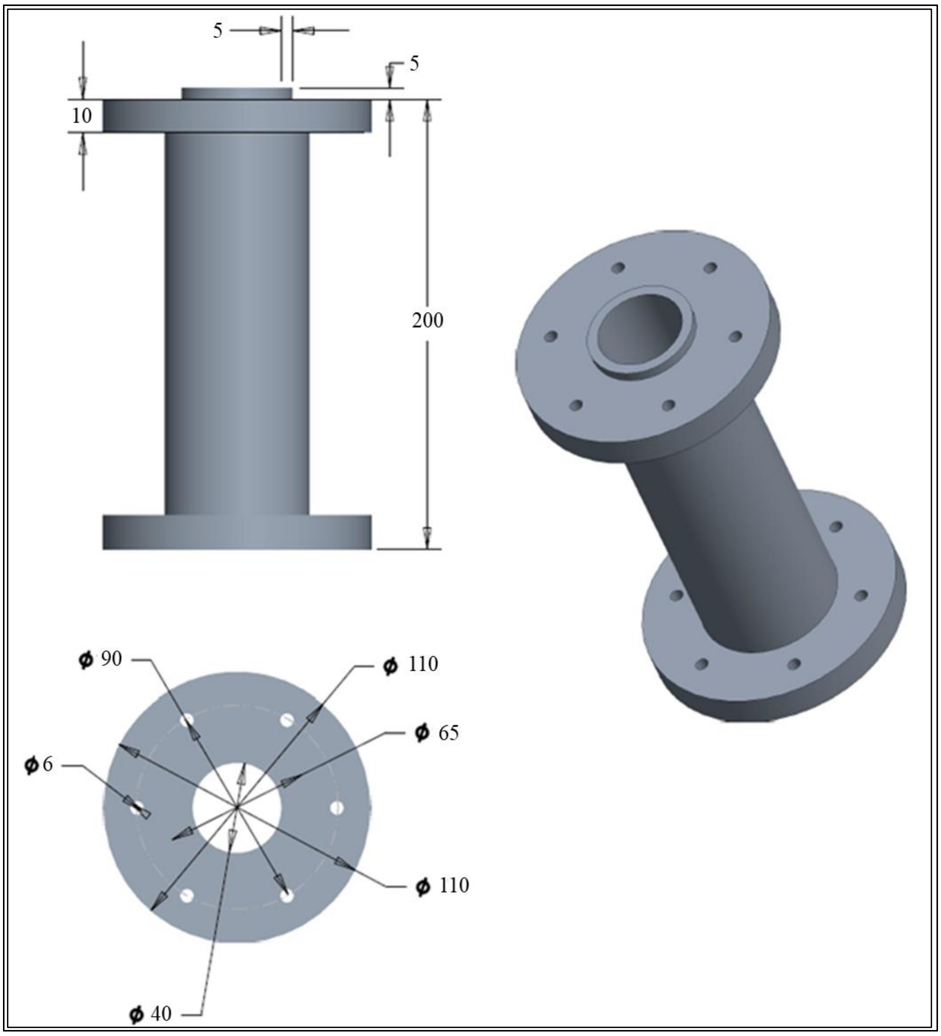

Fig. 3.5 Schematic design of medium cylinder (All dimensions are in mm).

Therefore, the outer diameter of the medium cylinder, d_{om} is:-

$$d_{om} = 40 + 2(12.5) = 65 \text{ mm} \quad (3.3)$$

Length of the medium cylinder

Length of medium cylinder, L_m = piston length + stroke length + allowance (3.4)

$$= 60 + 140 + 5 = 205 \text{ mm}$$

Flange dimensions

Medium cylinder flange contains 6 holes of 6 mm diameter (d_{hm}) for attaching medium cylinder to supporting plate. The pitch circle diameter (PCD) (d_{pm}) for the same is calculated as [87]:-

$$d_{pm} = d_{im} + 2(t_m) + 3d_{hm} \quad (3.5)$$

$$= 40 + (2 \times 12.5) + (3 \times 6) = 83 \text{ mm}$$

For safe design, the PCD in the setup was taken as 90 mm.

The outside diameter, d_{om} and thickness of the flange, t_{fm} is calculated as [87]:-

$$d_{om} = d_{pm} + 3d_{hm} \tag{3.6}$$

$$= 90 + (3 \times 6) = 108 \text{ mm}$$

Also,

$$t_{fm} = 1.25 \times d_{hm} \text{ to } 1.5 \times d_{hm} = 1.25 \times 6 \text{ to } 1.5 \times 6 \tag{3.7}$$

$$= 7.5 \text{ mm to } 9 \text{ mm}$$

In the current design, d_{om} and t_{fm} are taken as 110 and 10 mm, respectively. Fig. 3.5 shows the medium cylinder drawing with all the specifications.

3.3.3 Piston

The primary objective of the piston is to transmit the extrusion force of the hydraulic cylinder to the abrasive media. The AFF setup contains two medium cylinders, both of which have pistons. The piston helps in the to and fro motion of the media through the workpiece. The current setup needed a piston made of a material that has good strength and should also be lightweight. Therefore, the aluminum alloy was chosen to fabricate the piston for the AFF setup. Fig. 3.6(b-d) shows the geometrical specification for the piston assembly.

Material: Aluminum alloy

Yield strength: 275 MPa

Factor of safety: 5

Piston nut thickness

Piston nut thickness, t_{hp} is calculated using Grashoff's formula given below [87]:-

$$t_{hp} = \sqrt{\frac{3pd_{im}^2}{16\sigma_{dp}}} \tag{3.8}$$

where,

p = internal pressure on medium cylinder =12 MPa,

d_{im} = internal diameter of the medium cylinder = 40 mm,

σ_{dp} = design stress for piston material.

Now,

$$\sigma_{dp} = \frac{\sigma_{yp}}{FS} \tag{3.9}$$

$$= \frac{275}{5} = 55 \text{ MPa}$$

So,

$$t_{hp} = \sqrt{\frac{3 \times 12 \times 40^2}{16 \times 55}} = 8.09 \text{ mm}$$

In the current design, t_{hp} is taken as 10 (Fig. 3.6(c)).

Teflon piston ring

The piston head is likely to leak abrasive media in the working condition of the AFF setup. Consequently, the piston head is attached to a piston ring in order to address this issue. Due to its excellent tribological properties, the material selected for the piston ring was Teflon. The empirical relation that governs the radial thickness of the piston ring, t_{rp} is given as [87]:-

$$t_{rp} = \frac{d_{im}}{25} \times FS \tag{3.10}$$

$$= \frac{40}{25} \times 6 = 9.6 \text{ mm } \cong 10 \text{ mm}$$

The *FS* for the teflon ring is taken as 6. The high *FS* is due to the soft material of teflon rings. Therefore, the axial thickness of the ring is given as [87]:-

$$t_{ap} = \frac{\boldsymbol{d_{im}}}{10 \times n_r} \times FS \tag{3.11}$$

$$= \frac{40}{10 \times 1} \times 6 = 24 \text{ mm}$$

In the above equation, n_r denotes the number of rings. Fig. 3.6(d) represents the drawing specifications for Teflon rings.

Total length of the piston

The empirical relation for the total piston length is given as [87]:-

$$l_p = d_{im} \text{ to } 1.5 \ \times d_{im} \tag{3.12}$$

$$= 40 \text{ to } 60 \text{ mm}$$

For safe design, the length is 60 mm (Fig. 3.6(b)).

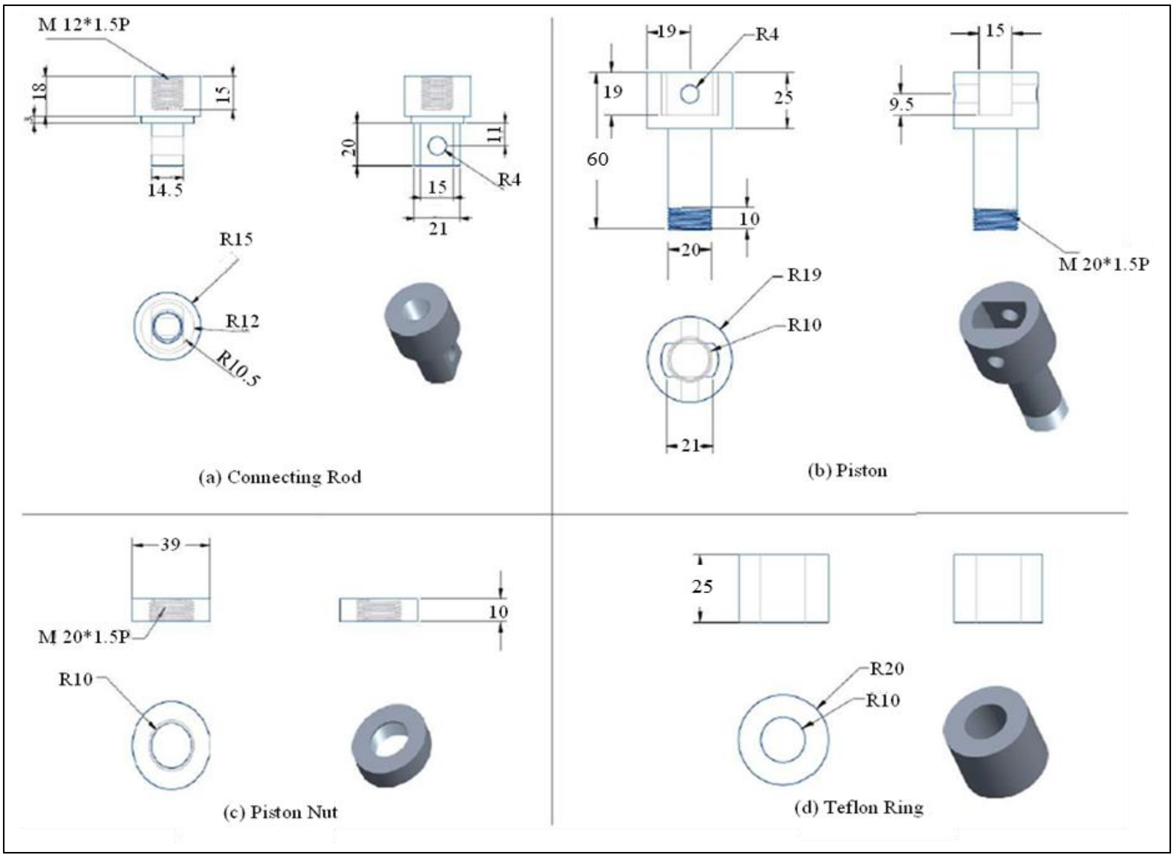

Fig. 3.6 Schematic diagram of **(a)** Connecting rod **(b)** Piston **(c)** Piston nut **(d)** Teflon ring (All dimensions are in mm).

Connecting rod

The hydraulic cylinder piston rod and the medium cylinder piston are connected via a connecting rod. M 12 x 1.5P threads comprise the hydraulic cylinder piston rod's constituent parts. Therefore, the hole must be the same size at the end of the connecting rod that faces the hydraulic cylinder. Thus, the dimension of the hole at the rod end of the hydraulic cylinder is M 12 x 1.5P (Fig. 3.6(a)).

The empirical relation for the outer diameter of the connecting rod, d_{ocr} is as follows [87]:-

$$d_{ocr} = 1.5\ to\ 2\ times\ inner\ hole\ diameter \tag{3.13}$$

$$= 1.5 \times 12 \text{ to } 2 \times 2 = 18\ to\ 24\ mm.$$

In the current design, it is considered to be 30 mm.

Also, the hole diameter in the connecting rod at the medium cylinder piston end is 8 mm.

So the width of that section, C_w is given as:-

$$C_w = 2 \times \text{hole diameter} = 2 \times 8 = 16 \text{ mm.} \tag{3.14}$$

In the present case, it is 21 mm, so the design is safe.

3.3.4 Workpiece fixture

The workpiece fixture consists of lower and upper parts, as shown in Fig. 3.7. Proper slots are provided in both the tooling parts for holding the TMCs in place during the AFF process. Also, the workpiece fixture is made of a conic profile to ensure a smooth flow of AFF media from the medium cylinder to the workpiece without any back pressure. A detailed drawing of the tooling is shown in Fig. 3.7.

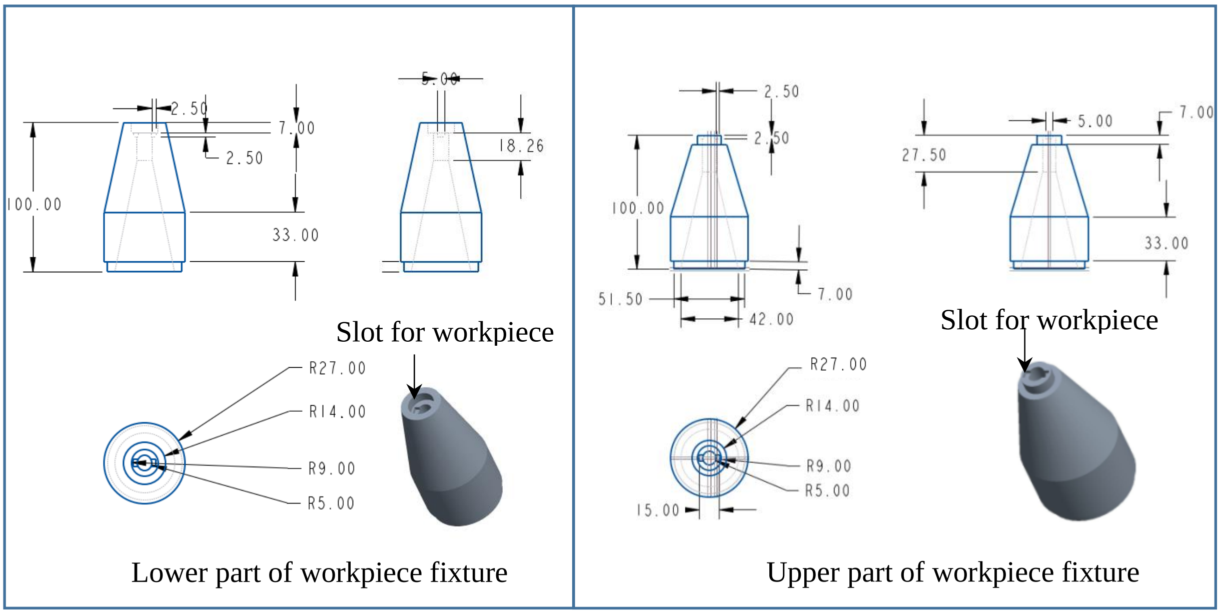

Fig. 3.7 Schematic diagram of workpiece fixture.

3.4 Characterization of sintered nanocomposites

The sintered titanium nanocomposites were subjected to various characterization techniques to study the physical, microstructural, mechanical, tribological, and corrosion changes compared to bare Ti6Al4V. These were carried out to evaluate the percentage change in their properties compared to sintered Ti6Al4V and to determine the effects of SPS input parameters on various output responses.

3.4.1 Microstructure and surface morphology

A scanning electron microscope (SEM) (JSM-6510LV, JOEL Ltd) was used to study the microstructure characterization of fabricated nanocomposites. Samples were polished and later exposed to an etchant to study the microstructure of Ti6Al4V/MLG nanocomposites. The SEM was equipped with energy-dispersive X-ray spectroscopy (EDS) to determine the elemental composition of polished nanocomposites. X-ray Diffraction (XRD) was employed to reveal the phases of fabricated samples. The scanning angle was varied between 20° to 90° at a rate of 4°/min. The phases of peaks obtained from XRD results were matched using

X'Pert Highscore software. Fig. 3.8 shows the images of SEM/EDS and XRD equipment used to study the microstructure of the sintered nanocomposites.

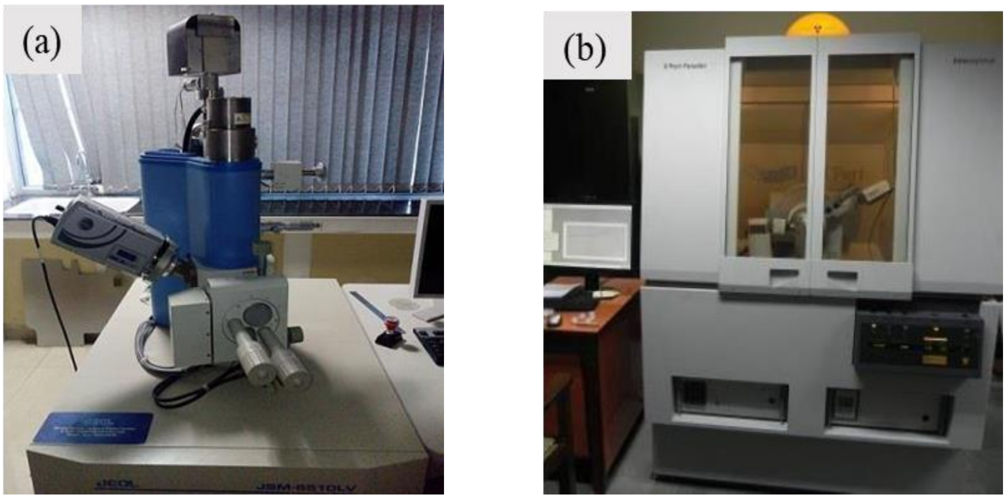

Fig. 3.8 Images of **(a)** SEM/EDS and **(b)** XRD equipment, Courtesy: TIET, Patiala.

A surface roughness tester (Mitutoyo model SJ-400, Germany) is used to study the surface morphology of the sintered nanocomposites. A tracing length of 0.08 mm was used for analysis. After performing the test 4 times for each sample, an average reading was taken out. Fig. 3.9 shows the surface roughness tester used to evaluate the surface roughness of the finished nanocomposites.

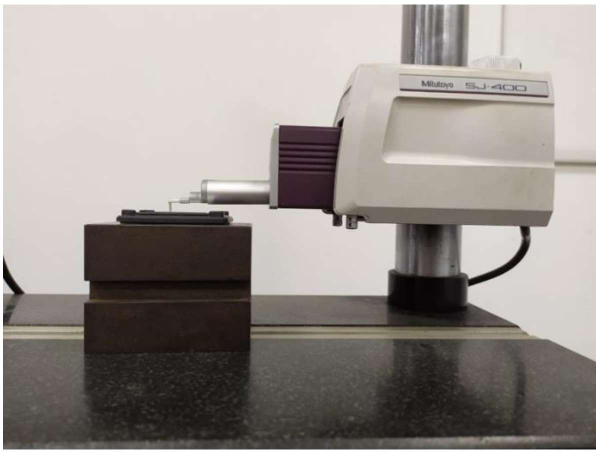

Fig. 3.9 Image of the surface roughness tester, Courtesy: TIET, Patiala.

3.4.2 Physical and mechanical characterization

Using a nanoindenter tester (Hyistron T1 950), sintered nanocomposites' mechanical properties, viz. nanohardness (*H*) and elastic modulus (*E*), were examined. Indentations were made at polished surfaces of nanocomposites using a 2000 μN force and a dwell time of 20 seconds. Five measurements were made for each sample to ensure the findings' accuracy and dependability. Fig. 3.10 shows the nanoindenter tester used to evaluate the mechanical characteristics of the sintered nanocomposites.

Fig. 3.10 Image of nanoindenter tester, Courtesy: IIT Ropar.

3.4.3 Tribological and corrosion characterization

Wear tests were performed on Ducom Instruments (TR-20 CH-400). The wear monitoring setup uses a pin on disk rotary tests using samples prepared according to ASTM G99 standards. EN31 steel disc (165 mm dia. and 8 mm thickness) was used as a rotating disc on which nanocomposites wear specimens slides. Fig. 3.11 shows the image of the tribometer used to carry out the wear test of the sintered nanocomposites.

Fig. 3.11 Image of tribometer setup, Courtesy: TIET, Patiala.

Corrosion studies were performed using three electrode cells (make: GAMRY instruments). Fig. 3.12 shows the corrosion setup used to evaluate the corrosive properties of fabricated nanocomposites. Ti6Al4V-MLG nanocomposites serve as the working electrode. The reference electrode is of Ag/AgCl, while a platinum wire makes the counter electrode. Experiments were performed by using 3.5 wt. % NaCl solution as electrolyte. Corrosion studies include potentiodynamic polarization (electrode potential range is -1 V to 1.5 V with a scan rate of 1 mv/s) and electrochemical impedance spectroscopy (EIS). EIS is carried out with an AC signal of 3 mV amplitude in the 0.01 Hz to 10,000 Hz frequency range.

Fig. 3.12 Image of corrosion setup, Courtesy: TIET, Patiala.

3.4.4 Finishing of the nanocomposites

Fig. 3.13 shows the image AFF setup, which has been fabricated in-house to perform finishing operations on the sintered titanium nanocomposites.

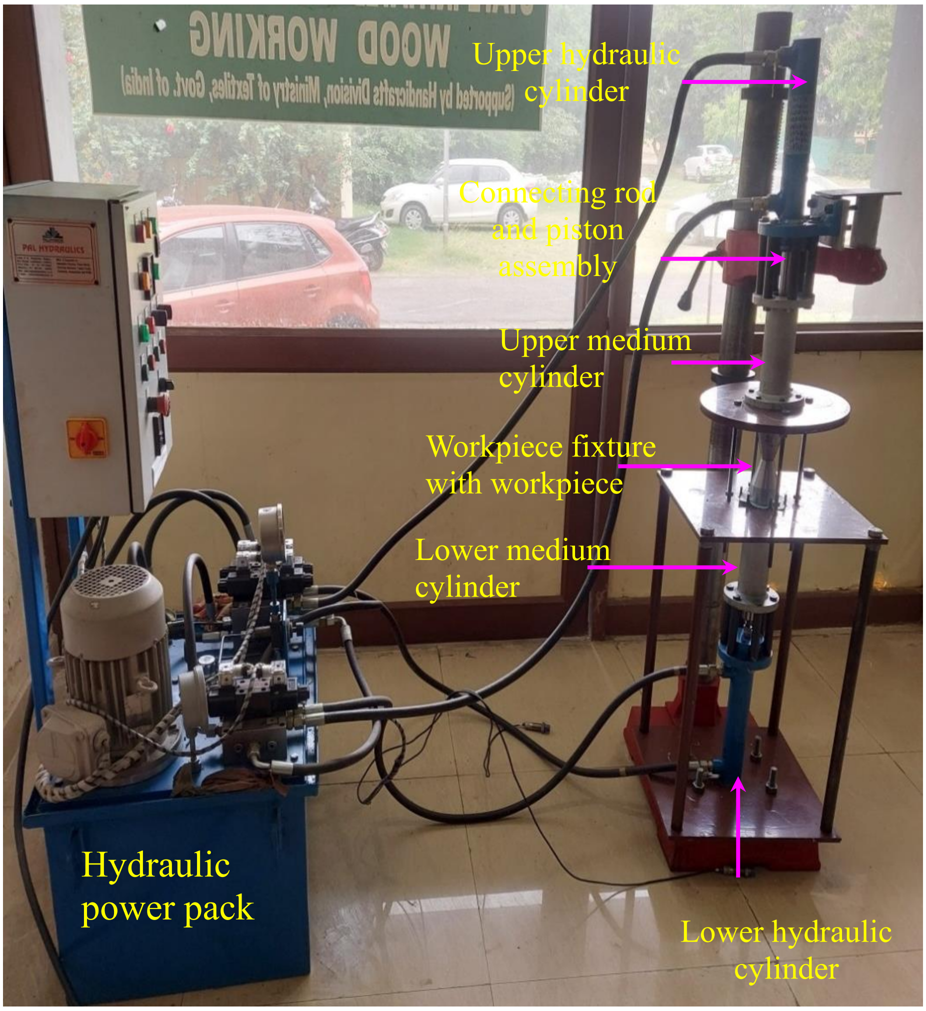

Fig. 3.13 Image of the AFF setup.

CHAPTER 4

RESULTS AND DISCUSSION

In this chapter, various results obtained after microstructural, physical, mechanical, tribological, and corrosion characterization that has been carried out on the fabricated TMCs are discussed. Also, the sintered TMCs undergo the finishing via the AFF process. The analysis of the individual testing characteristics has been discussed in detail in the current section. Furthermore, the parametric study is carried out to study the effect of the wt. % of MLG and sintering temperature on the output responses.

4.1 Preliminary experiments

Preliminary experiments were conducted firstly to validate the authenticity of the present work and secondly to find the suitable ranges of input parameters for improving the output responses of the fabricated nanocomposites. The sintering temperature was kept constant during the preliminary experiments at 1150 ℃, and wt. % of MLG was varied from 0 to 1.2 with a step size of 0.4. Its effects were studied on the mechanical properties, i.e., hardness and elastic modulus.

4.1.1 Densification of sintered nanocomposites

Theoretical density, experimental density, relative density, and porosity of fabricated TMCs are shown in Table 4.1. The theoretical density of Ti6Al4V and MLG was taken as 4.429 g/cm^3 [88] and 2.234 g/cm^3 [89], respectively. The theoretical density, $\rho_{T,}$ of sintered nanocomposites is calculated using the rule of mixture given in equation 4.1. Experimental density, $\rho_{E,}$ is calculated using the Archimedes principle.

$$\rho_T = \frac{1}{\frac{w_m}{\rho_m} + \frac{w_{MLG}}{\rho_{MLG}}} \tag{4.1}$$

Where w_m is the wt. % of the matrix, ρ_m is the density of the matrix. Similarly, w_{MLG} and ρ_{MLG} represent the wt. % and density of MLG reinforcement.

After that, % porosity is calculated using equation 4.2 [90].

$$\% \, Porosity = \frac{Theoritical\ density - Experimental\ density}{Theoritical\ density} \times 100 \tag{4.2}$$

Experimental densities were taken three times for various samples to maintain accuracy in the results, and their average value was reported. Table 4.1 shows the % porosity for sintered bare Ti6Al4V and Ti6Al4V/MLG nanocomposites. The porosity of the sintered composites decreases with the increase in MLG content. This improvement in the densification of the nanocomposites is due to the high electrical and thermal conductivity of MLG reinforcement. Due to MLG's high electrical and thermal conductivity, the composite powder is subjected to uniform current and heat distribution during consolidation. This uniform powder heating tends to improve nanocomposites' sintering and densification.

Table 4.1 Comparative analysis of theoretical and experimental densities.

Workpiece composition	**Theoretical density (g/cm^3)**	**Experimental density (g/cm^3)**	**Relative density (%)**	**Porosity (%)**
Ti6Al4V	4.430	4.367	98.57	1.42
Ti6Al4V/0.4 wt. % MLG	4.421	4.390	99.29	0.70
Ti6Al4V/0.8 wt. % MLG	4.412	4.395	99.61	0.38
Ti6Al4V/1.2 wt. % MLG	4.403	4.391	99.72	0.27

4.1.2 Load-displacement and depth-time curves of the sintered nanocomposites

The load-displacement curves of the TMCs comprising of various content of MLG, when subjected to indentation load of 2000 µN, are shown in Fig. 4.1. As evident from Fig. 4.1, similar loading and unloading behaviors were observed in both sintered Ti6Al4V alloy and MLG reinforced nanocomposites. Elastic plastic deformation behavior can be depicted from the load-displacement curves. The maximum penetration depth occurs in sintered Ti6Al4V alloy followed by Ti6Al4V/0.4 wt. % MLG, Ti6Al4V/0.8 wt. % MLG and Ti6Al4V/1.2 wt. % MLG nanocomposites. This may be due to the presence of MLG, which improves the resistance of Ti6Al4V/MLG nanocomposites to plastic deformation.

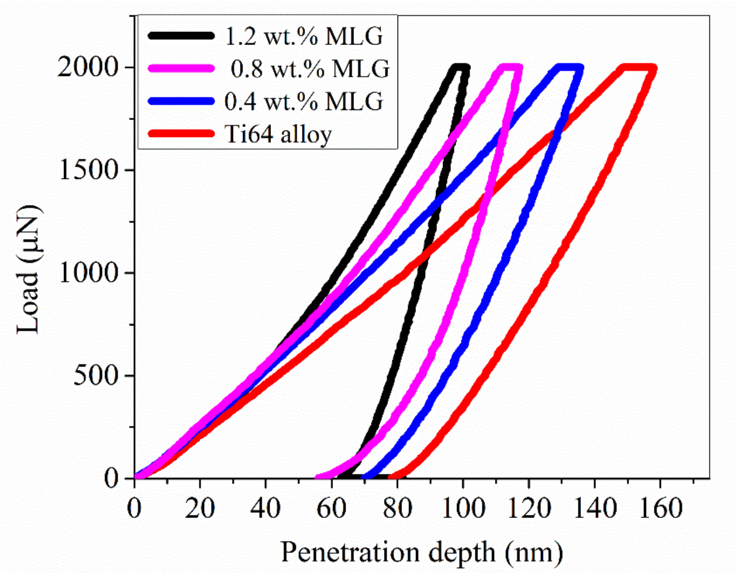

Fig. 4.1 Penetration depth vs. load of sintered Ti6Al4V alloy and Ti6Al4V/MLG nanocomposites.

Fig. 4.2 depicts the penetration depth with time of the sintered Ti6Al4V and Ti6Al4V/MLG nanocomposites comprising various MLG content when subjected to indentation of 2000 µN. A considerable amount of plastic deformation occurs in the sintered TMCs subjected to a load of 2000 µN. The penetration of sintered Ti6Al4V, Ti6Al4V/0.4 wt. % MLG, Ti6Al4V/0.8 wt. % MLG and Ti6Al4V/1.2 wt. % MLG nanocomposites at 2000 µN are 157 nm, 135 nm, 116 nm, and 97 nm, respectively. This improvement in the mechanical properties with the increased content of MLG is due to the load transfer mechanism of the titanium matrix to the reinforcement [91].

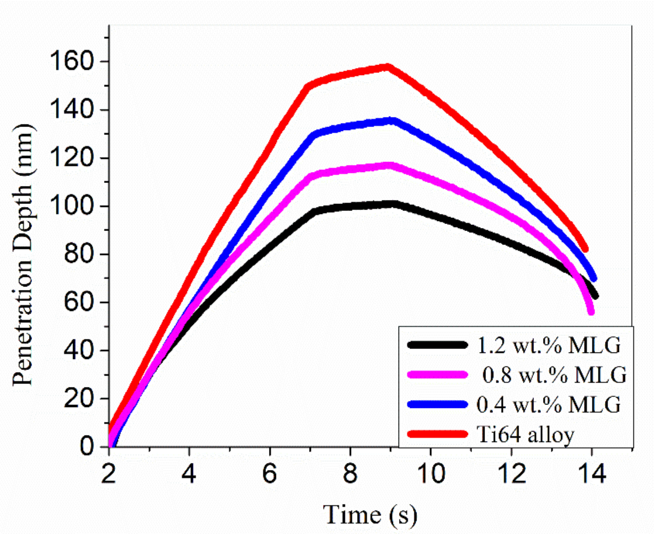

Fig. 4.2 Penetration depth vs. time of sintered Ti6Al4V alloy and Ti6Al4V/MLG nanocomposites.

4.1.3 Nanohardness and elastic modulus of the sintered nanocomposites

The nanohardness and elastic modulus of the sintered Ti6Al4V and the Ti6Al4V/MLG nanocomposites are shown in Fig. 4.3.

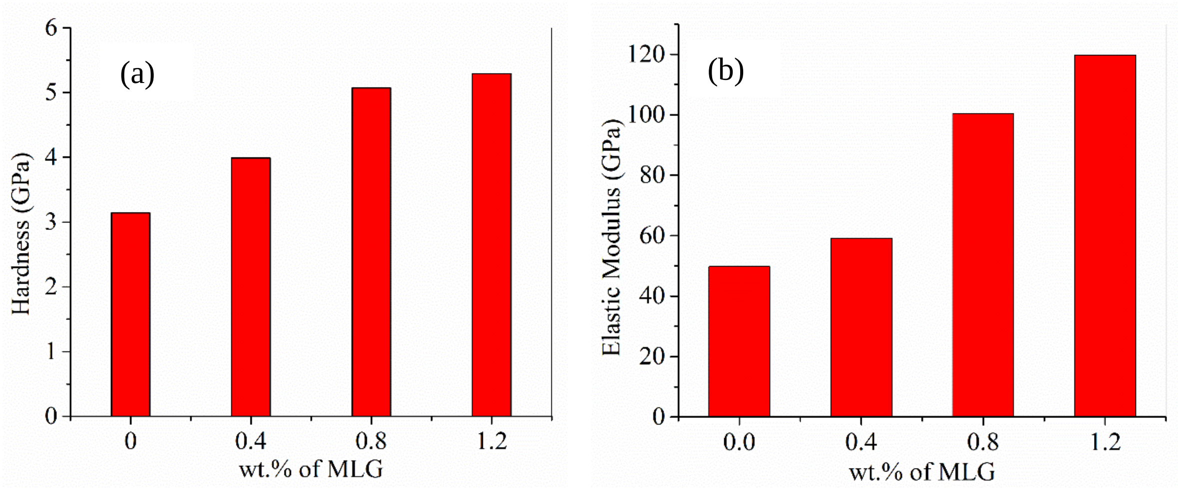

Fig. 4.3 (a) Hardness **(b)** Elastic modulus value for various wt. % of MLG.

The value of the nanohardness improves with the increase in the MLG concentration in the titanium matrix. The nanohardness of sintered Ti6Al4V alloy was 3.14 GPa, and Ti6Al4V nanocomposites with 1.2 wt. % MLG concentration has a nanohardness of 5.29 GPa. This corresponds to a maximum of 68.4 % increase in nanohardnes of sintered Ti6Al4V compared to bare Ti6Al4V. Ti6Al4V with MLG reinforcement of 0.4 wt. % and 0.8 wt. % has nanohardness values of 3.99 GPa and 5.07 GPa, respectively. The increase in hardness of nanocomposites can be due to:-

a) Solution strengthening of carbon (C) atoms from MLG.
b) Grain refinement of titanium matrix.
c) Dispersion strengthening of TiC particles formed due to in-situ reaction.
d) Load transferring effect from matrix to reinforcement.

A binary phase diagram can depict the solubility of the C atom in the titanium matrix at room temperature, which is nearly 0.05 wt. % [92]. When the amount of carbon in the matrix exceeds the solubility limit during sintering, carbon tends to react with titanium to form TiC. Average grain size diameter after refinement has inverse effects on the strengthening of the matrix. In the present study, as the weight concentration of MLG increases, the grain size of the matrix reduces effectively. Therefore, grain refinement can improve the nanohardness of the titanium matrix. The in-situ reaction of C and Ti leads to dispersion strengthening due to the formation of TiC particles. The in-situ reaction between Ti and C forms a strong bond between TiC particle and Ti, making a weak bond between MLG and Ti matrix into a strong, stable chemical bond [93]. Hence, both TiC particles and unreacted Ti in the matrix will play a critical role in bearing load transfer, eventually increasing the nanohardness of the nanocomposites. Fig. 4.4 shows the FESEM image of the interface of Ti6Al4V and MLG, and it is evident that the interface formed is clean and strong. The EDS results in Fig. 4.4 show the presence of Ti and C peaks, confirming their strong bonding.

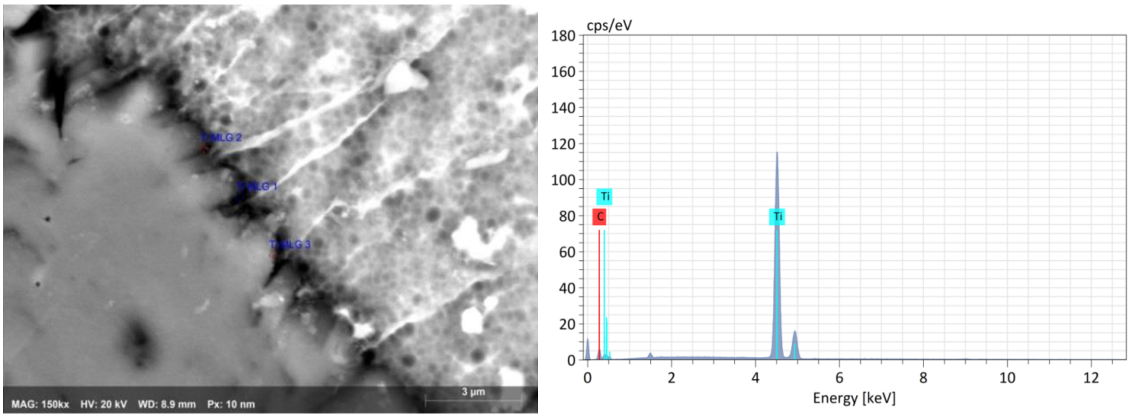

Fig. 4.4 FESEM and EDS image of Ti6Al4V/MLG nanocomposite interface.

The improvement was also observed in the elastic modulus of nanocomposites. This indicates that the samples were elastically resisted from linear compression of the indenter. Furthermore, with the increase in the MLG concentration, the nanocomposites' elastic modulus increased. The elastic modulus value of sintered Ti6Al4V alloy was 49.8 GPa. Compared to Ti6Al4V, Ti6Al4V-MLG nanomaterial with 1.2 wt. % MLG has the maximum elastic modulus of 119.8 GPa, showing an improvement of 140.5 % compared to Ti6Al4V alloy. Ti6Al4V nanomaterial with MLG reinforcement of 0.4 and 0.8 wt. % has an elastic modulus value of 59.2 GPa and 100.4 GPa, respectively. These results indicated that the presence of the MLG in the sintered nanocomposites enhanced the stiffness of the materials. This improvement in the elastic modulus of the reinforced titanium nanocomposites may be due to the formation of a secondary carbide phase (TiC), which improved mechanical properties. Table 4.2 shows the present work's comparative study with some relevant available literature.

Table 4.2 Comparative analysis of present work with published literature.

S. No	Authors	Material	% increase in hardness	% increase in elastic modulus
1.	Present Study	Ti6Al4V/MLG	68.5%	140.5%
2.	Wang et al. [94]	Ti6Al4V/GNP	18%	-
3.	Song et al [95]	Ti/MLG	71.38%	6.39%
4.	Gürbüz et al [49]	Ti/GNP	50.4%	-
5.	Yan et al [96]	Ti6Al4V/GNS	9.45%	52.63%
6.	Cao et al [97]	Ti/GNP	49%	-

Using the above results of sintered Ti6Al4V/MLG nanocomposites, mechanical behavior, and wear properties were evaluated. Elastic recovery index W_e/W_t, plasticity index W_p/W_t, nanohardness to elastic modulus ratio *H/E*, and yield pressure H^3/E^2 were studied to determine the material's elastic, plastic, and wear properties. W_e and W_p represent the elastic energy and plastic energy, respectively, and these can be calculated from the area under the load-displacement curve. Also, W_t represents the total work done by the indenter and can be expressed as equation 4.3.

$$W_t = W_e + W_p \tag{4.3}$$

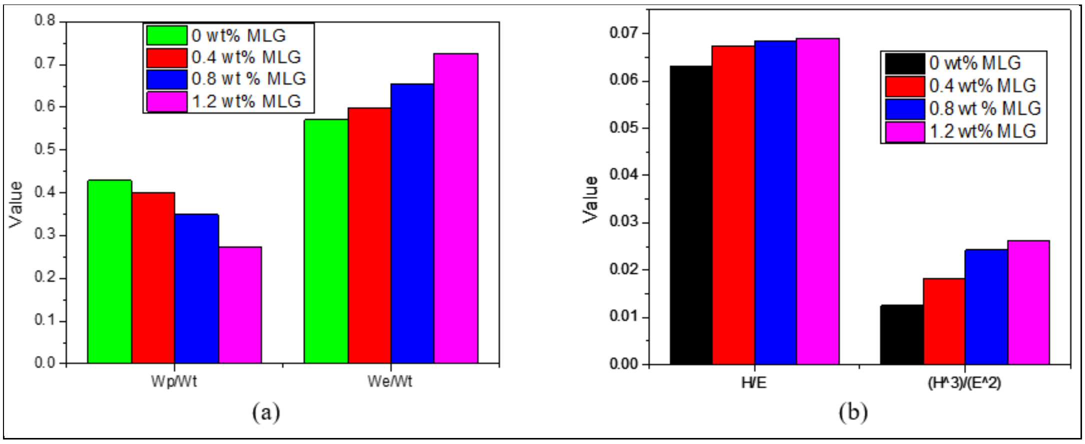

Fig. 4.5 (a) Plasticity index and elastic recovery **(b)** Nanohardness to elastic modulus ratio and yield pressure of sintered nanocomposites.

Fig. 4.5 (a) displays the elastic recovery index and plasticity index of Ti6Al4V alloy and Ti6Al4V/MLG nanocomposites. The elastic recovery index reveals the energy released by the material under loading conditions, whereas the plasticity index reveals the innate plastic behavior of the material. Therefore, with the increase in the MLG concentration of the nanocomposites, the value of the elastic recovery index increases, and the plasticity index decreases. The value of the elastic recovery index was maximum for 1.2 wt. % MLG followed by 0.8, 0.4, and 0 wt. % of MLG concentration. The maximum value for the plasticity index was found to be for sintered Ti6Al4V alloy, and it decreases with the increase in MLG content in the nanocomposites. These results indicate that adding MLG reinforcement into the titanium matrix improves the nanocomposite's resistance to plastic deformation, previously shown in nanohardness and elastic modulus results. The ratio of nanohardness to elastic modulus determines the resistance to elastic strain to failure. This effect increases with an increase in MLG concentration (Fig. 4.5 (b)). The yield pressure value of unreinforced titanium alloy was the lowest compared to its counterpart MLG-reinforced nanocomposites. The improvement in these results implies the excellent material resistance under impact loading and wear of the sintered titanium nanocomposites [98].

4.2 Design of experiments

In the present study, experiments were designed using the central composite rotatable design (CCRD) method to evaluate the impact of SPS parameters (wt. % of MLG and sintering temperature) on the various output responses (Hardness, elastic modulus, wear rate, and corrosion current density). The statistical data and the regression model were generated with the help of design expert (version 6.1) software. The range for the input parameter, i.e., wt. % of MLG was kept in conformity with the preliminary experiments, whereas the range for sintering temperature was kept after considering the various published literature. Table 4.3 shows input parameters and their corresponding values that are varied at five levels.

Table 4.3 Process parameters and their ranges for the SPS process.

Symbol	Variable	Levels				
		-1.414	-1.000	0.000	1.000	1.414
A	Sintering temperature (°C)	787	850	1000	1150	1212
B	wt. % of MLG (%)	0.23	0.40	0.80	1.20	1.36

The experimental runs for the designed problem can be calculated using equation 4.4.

$$N = 2^n + 2n + n_c \tag{4.4}$$

Where, N is the number of the experimental run, n is the number of input process parameters, and n_c is the number of repeated runs at the center point. The total number of runs for the experimentation in the present work was 13. The analysis of variance (ANOVA) is conducted on the designed model by the statistical tool. The F-test is conducted to determine the significance of the developed models. ANOVA is performed to find the significant SPS input parameters and their % contribution to output responses.

4.2.1 Mechanical characterization

4.2.1.1 Analysis of variance for hardness and elastic modulus of sintered nanocomposites

The experimental design with corresponding outputs, i.e., hardness and elastic modulus, is shown in Table 4.4. Comparative analysis between the experimental results and the results obtained by the regression equation 4.6 and equation 4.7 shows the maximum % error of 7.79 % for hardness and -18.24 % for elastic modulus, which is given as:-

$$\% \, Error = \frac{\text{Experimental value} - \text{Numerical value}}{\text{Experimental value}} \times 100 \tag{4.5}$$

Table 4.4 Experimental design with corresponding outputs.

Run	Factors		Hardness (GPa)		Elastic modulus (GPa)		% error	
	ST (°C)	WT (%)	Experimental	Numerical	Experimental	Numerical	Hardness	Elastic modulus
1	1000	0.8	5.37	5.29	138.9	132.78	1.49	4.41
2	1000	0.23	3.59	3.36	74.1	61.20	6.41	17.41
3	1000	0.8	5.18	5.29	130.1	132.78	-2.12	-2.06
4	1150	1.2	5.29	5.14	119.8	119.12	2.84	0.57
5	850	0.4	3.21	3.46	51.5	59.98	-7.79	-16.47
6	1150	0.4	3.99	4.10	59.2	70.00	-2.76	-18.24
7	787	0.8	3.81	3.67	64.2	61.94	3.67	3.52
8	1000	0.8	5.15	5.29	127.1	132.78	-2.72	-4.47
9	1000	0.8	5.41	5.29	136.7	132.78	2.22	2.87
10	850	1.2	3.74	3.72	85.6	82.60	0.53	3.50
11	1212	0.8	5.07	5.12	100.4	94.86	-0.99	5.52
12	1000	1.36	4.14	4.28	108.6	113.47	-3.38	-4.48
13	1000	0.8	5.32	5.29	131.1	132.78	0.56	-1.28

ST: Sintering temperature, WT: wt. % of MLG

The ANOVA table for the hardness and elastic modulus of the designed model are shown in Table 4.5 and Table 4.6, respectively. From the response model for hardness and elastic modulus, the F-values are 43.78 and 32.97. The high "model F-value" could not be attributed to noise because the probability of this happening is only 0.01 %. In the present work, model F-value > critical F value confirms that both models are significant [99]. A small *P*-value (Prob. > F) implies that the associated coefficient is more important, so its contribution to the response variable is also significant. The significance of the model term can be predicted by analyzing the F-values for the hardness and elastic modulus model. Input parameters coefficients with a P-value less than 0.05 (significance level, α for 95 % confidence interval) significantly contribute towards the output responses. It is evident from Table 4.5 and Table 4.6 that both sintering temperature and % wt. of MLG were found to be significant for the models. The % contribution of sintering temperature ($A + A^2$) and wt. % of MLG ($B + B^2$) was 42.15 % and 55.40 %, respectively for hardness. Also, the % contribution for the elastic modulus was 49.24 % for sintering temperature and 48.61 % for wt. % of MLG. The interaction effect of the input parameters (AB) is insignificant, with a % contribution of 1.81 % and 1.39 % in deciding the hardness and elastic modulus. In the present study, the lack of fit test is within the non-significant range compared to pure error, indicating that both models fit the experimental data well.

Table 4.5 ANOVA table for hardness.

Source	**Sum of squares**	D_f	**Mean square**	***F*-value**	***P*-value Prob. >*F***		**% contri-bution**
Model	7.73	5	1.55	43.78	0.0001	significant	
A	2.11	1	2.11	59.82	0.0001	significant	25.41
B	0.85	1	0.85	24.06	0.0017	significant	10.24
A^2	1.39	1	1.39	39.30	0.0004	significant	16.74
B^2	3.75	1	3.75	106.16	0.0001	significant	45.16
AB	0.15	1	0.15	4.20	0.0797	not significant	1.81
Residual	0.25	7	0.035				
Lack of Fit	0.19	3	0.065	4.85	0.0806	not significant	
Pure Error	0.053	4	0.013				0.64
Cor Total	7.98	12					

A: Temperature, B: % wt. of MLG

Table 4.6 ANOVA table for elastic modulus.

Source	**Sum of squares**	D_f	**Mean square**	**F-value**	**P-value Prob. >F**		**% contri-bution**
Model	11562.23	5	2312.45	32.97	0.0001	significant	
A	1083.32	1	1083.32	15.44	0.0057	significant	8.57
B	2573.69	1	2573.69	36.69	0.0005	significant	20.35
A^2	5142.93	1	5142.93	73.32	0.0001	significant	40.67

B^2	3573.58	1	3573.58	50.94	0.0002	significant	28.26
AB	175.56	1	175.56	2.50	0.1577	not significant	1.39
Residual	491.03	7	70.15				
Lack of Fit	395.94	3	131.98	5.55	0.0656	not significant	
Pure Error	95.09	4	23.77				0.75
Cor Total	12053.26	12					

A: Temperature, B: % wt. of MLG

Table 4.7 shows the statistical parameters of the model. Using R^2 (coefficient of determination), the reduction in response variability for hardness and elastic modulus was calculated to be 0.9690 and 0.9593, respectively. This indicates that the experiment variables contribute 96.90 % and 95.93 % to the total variance in the hardness and elastic modulus measurement. The model is the best fit for data as the value of R^2 is close to 1. The hardness model's standard deviation (SD) is 0.19, while that of elastic modulus is 8.38. A lower SD and the value of R^2 close to 1 result in a better model. 0.9469 and 0.9302 correspond to the adjusted R^2 value for the hardness and elastic modulus measurement, implying that there is no need for any additional term in the regression equation model. The values of adequate precision for the model are 15.110 and 12.795 which shows that the model is fit. Adequate precision tells us about the signal-to-noise ratio of the model. The desired value for adequate precision is greater than 4 [100]. It can be calculated by dividing the maximum and minimum predicted response difference by the average SD value of all predicted values.

Table 4.7 Statistical parameters of the model equation as obtained from the ANOVA model of hardness and elastic modulus

Type of variable	**Hardness model**	**Elastic modulus model**
Standard deviation (SD)	0.19	8.38
Mean	4.56	102.10
R^2	0.9690	0.9593
Adjusted R^2	0.9469	0.9302
Predicted R^2	0.8167	0.7541
Adequate precision	15.110	12.795

The regression equation for predicting the hardness and elastic modulus of sintered nanocomposites as a function of sintering temperature (A) and wt. % of MLG (B) is represented in equation 4.6 and equation 4.7, respectively.

$$Hardness = -19.01843 + 0.040571A + 4.94911B - 0.0000198556A^2 - 4.58906B^2 + 0.00320833AB \quad (4.6)$$

$$Elastic\ Modulus = -1191.44248 + 2.40613A + 161.07407B - 0.00120844A^2 - 141.65625B^2 + 0.11042AB \quad (4.7)$$

4.2.1.2 The normal probability plot of residuals for hardness and elastic modulus

Fig. 4.6 (a) and (b) show the relationship between the actual response vs. predictive response plots (hardness) and the normal plot of the residuals (hardness), respectively. These relationships are used to assess the suitability of the developed model. It can be seen from the graph that predictive values from the model and the actual values from the experimentation are very close to each other. This closeness of values signifies that the model generated is accurate. For the hardness responses, it was found that the plot's model ensured a relatively uniform distribution of values along the fit line. This was supported by the results obtained for adjusted R^2 (0.9469) and R^2 (0.9690), which are close to 1. These values ensure that the model is fit to the experimental data. The studentized residuals' normal probability plot further confirms the regression model's adequacy. The residuals on the normal probability plot form a straight line, implying that the errors form a normal distribution and the output responses are correctly predicted in an unbiased manner. A similar trend was followed for the elastic modulus, as shown in Fig. 4.7 (a) and (b).

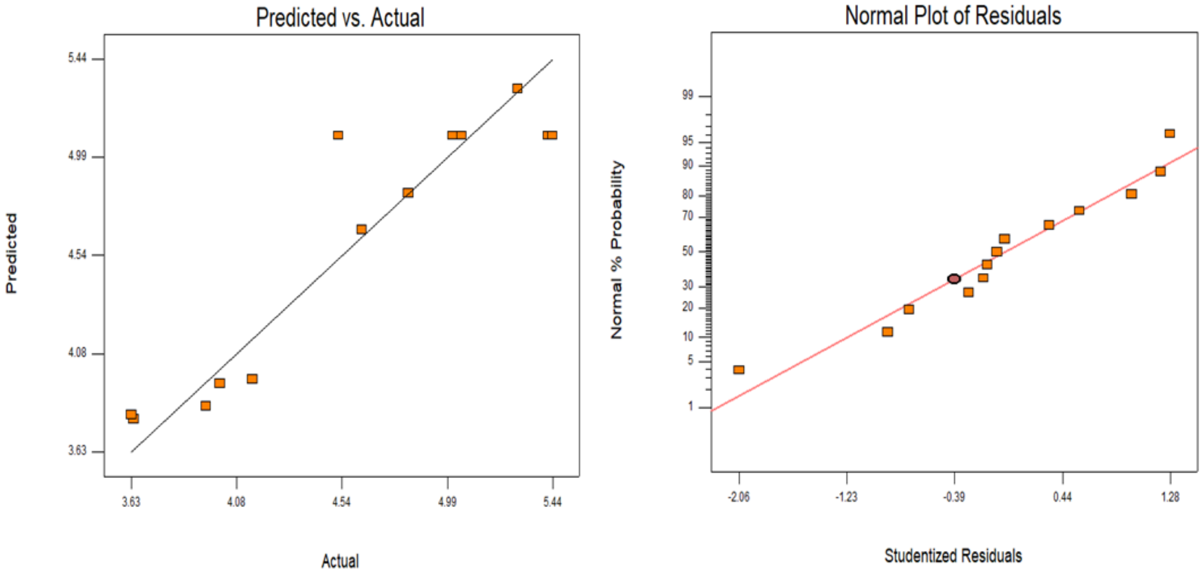

Fig. 4.6 (a) Actual response vs. predictive response plots for hardness **(b)** Normal plot of the residuals for hardness.

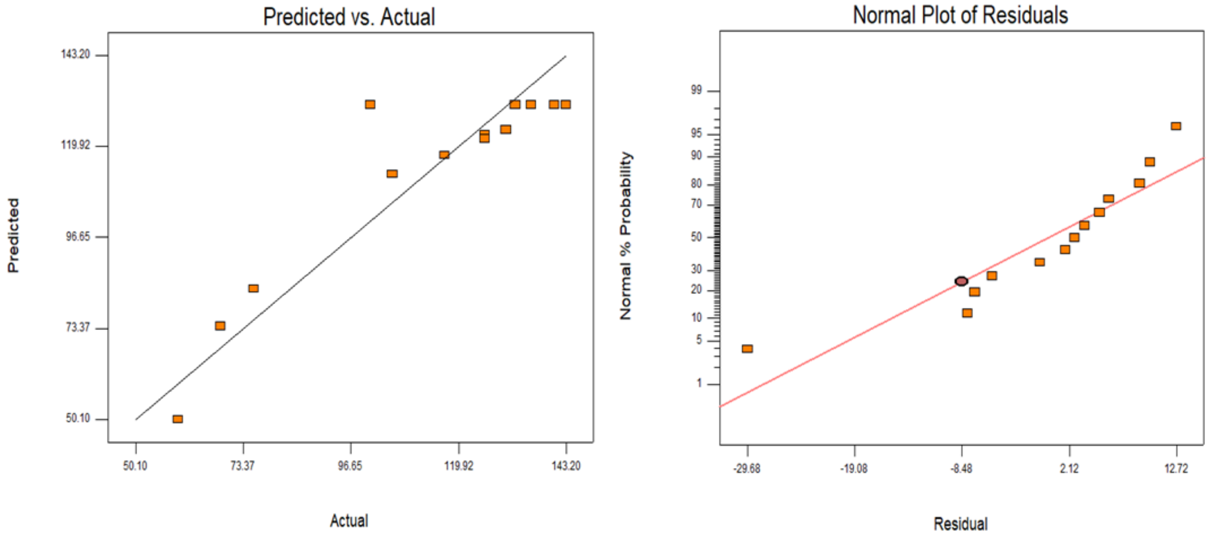

Fig. 4.7 (a) Actual response vs. predictive response plots for elastic modulus **(b)** Normal plot of the residuals for elastic modulus.

4.2.1.3 Effect of sintering temperature on hardness and elastic modulus of sintered nanocomposites

Fig. 4.8 (a) and (b) show the relationship between sintering temperature vs. hardness and sintering temperature vs. elastic modulus, respectively. There is an increase in the hardness value, and elastic modulus is nearly upto 1100 °C and 1020 °C. Thereafter, the value of hardness and elastic modulus decreases. The increase in the hardness and elastic modulus values due to the change in sintering temperature is attributed to the higher density of the nanocomposites [101]. Due to the higher diffusion rate at higher sintering temperatures, a denser structure is formed.

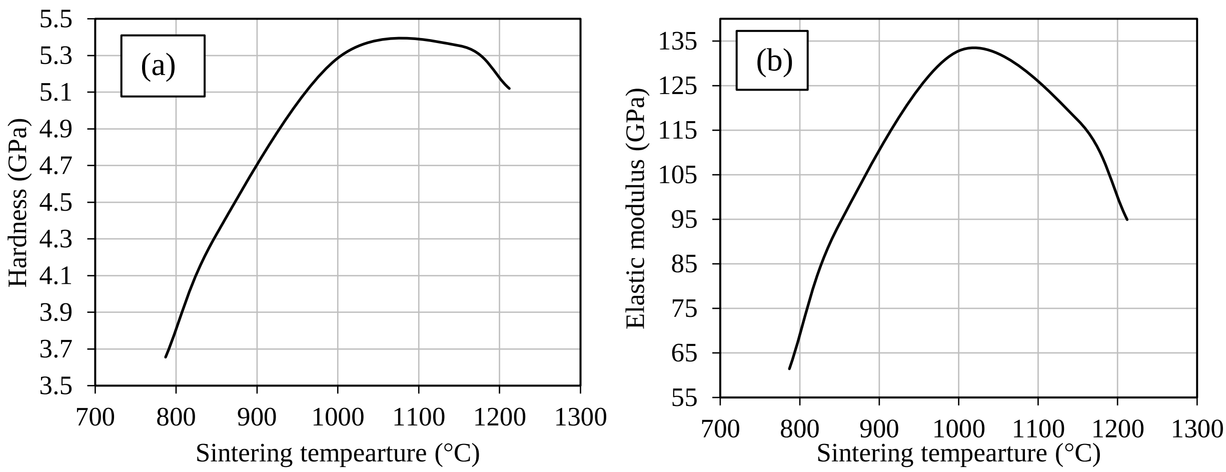

Fig. 4.8 (a) Sintering temperature vs. hardness **(b)** Sintering temperature vs. elastic modulus

Theoretical density, experimental density, relative density, and % porosity of fabricated TMCs are shown in Table 4.8.

Table 4.8 Comparative analysis of theoretical and experimental densities.

Workpiece composition	Sintering temperature (°C)	Theoretical density (g/cm^3)	Experimental density (g/cm^3)	Relative density (%)	Porosity (%)
Ti6Al4V/0.8 wt. % MLG	787	4.412	4.297	97.39	2.60
Ti6Al4V/0.8 wt. % MLG	1000	4.412	4.367	98.97	1.01

The hall patch relation can explain the decreasing trend in response to further increasing the sintering temperature. The grain growth beyond certain sintering temperatures results in a decrease in response values [102]. To study the reason for the reduction of hardness value beyond 1100 °C, the average grain size of nanocomposite was calculated using image J software. The average grain size of the nanocomposite for 1212 °C at 0.8 wt. % was found to be 6.250 $\pm$ 1.86 µm. This average grain size is 24 % higher than the average grain size of 1000 °C/0.8 wt. % nanocomposites. Table 4.9 shows the average grain size of both the nanocomposites. The SEM image used to calculate the average grain size is shown in Fig. 4.9.

Table 4.9 Average grain size diameter of fabricated nanocomposites.

Workpiece composition	Sintering temperature (°C)	Average grain size diameter (µm)	% increase of average grain size diameter (µm)
Ti6Al4V/0.8 wt. % MLG	1000	5.040 $\pm$ 2.30	-
Ti6Al4V/0.8 wt. % MLG	1212	6.250 $\pm$ 1.86	24 %

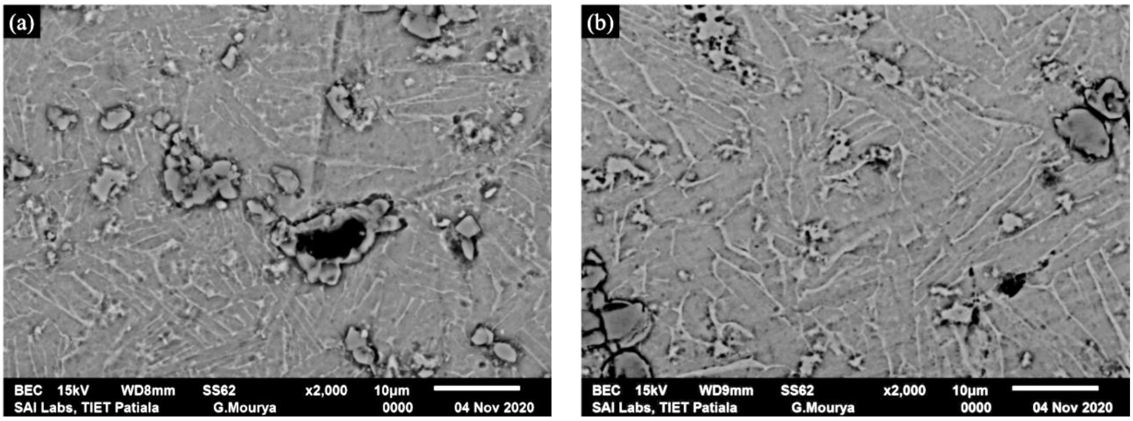

Fig. 4.9 SEM image of nanocomposite **(a)** 1000 °C **(b)** 1212 °C fabricated with 0.8 wt. % of MLG.

4.2.1.4 Effect of wt. % of MLG on hardness and elastic modulus of sintered nanocomposites

Fig. 4.10 (a) and (b) shows the relationship between wt. % of MLG vs. hardness and wt. % of MLG vs. elastic modulus, respectively. As shown in both the figures, hardness, and elastic modulus increases with an increase in the MLG content. However, beyond a threshold, the values of responses decrease. The formation of titanium carbides (TiC) in the nanocomposites due to the in-situ reaction of Ti and C during sintering increases the response value [103]. The confirmation of TiC was done with the help of XRD results. The peak for titanium carbide was detected in the nanocomposites. Fig. 4.11 (a) shows the XRD pattern of nanocomposite fabricated at 1000 °C and 0.8 wt. % of MLG. The other peaks in the results correspond to Ti, Al, V, and C. The decrease in the response values beyond the particular MLG reinforcement content may be attributed to the agglomeration in the matrix [104]. As shown in Fig. 4.11 (b), agglomeration of the MLG occurs in TMCs with 1.36 wt.% of MLG. This results in an increase in porosity, lower density, and hardness values.

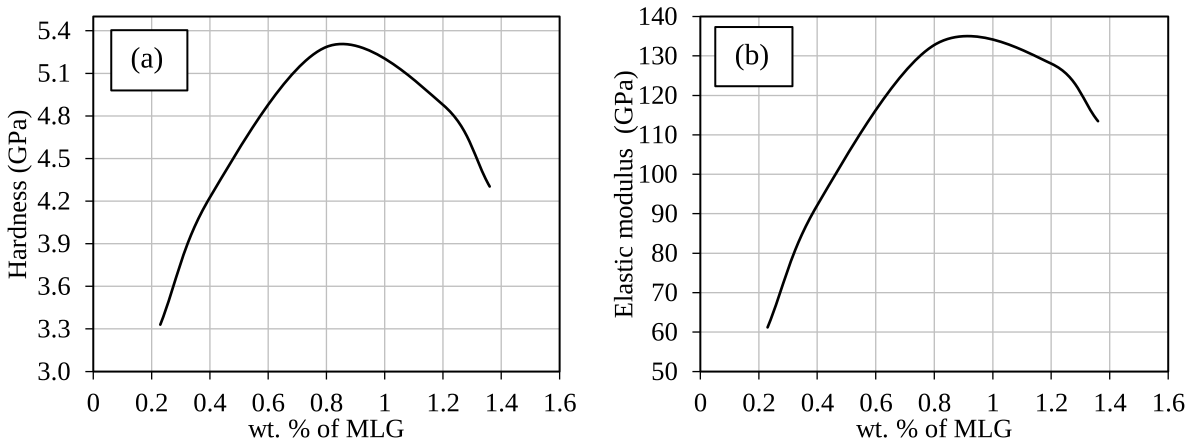

Fig. 4.10 (a) wt. % of MLG vs. hardness **(b)** wt. % of MLG vs. elastic modulus.

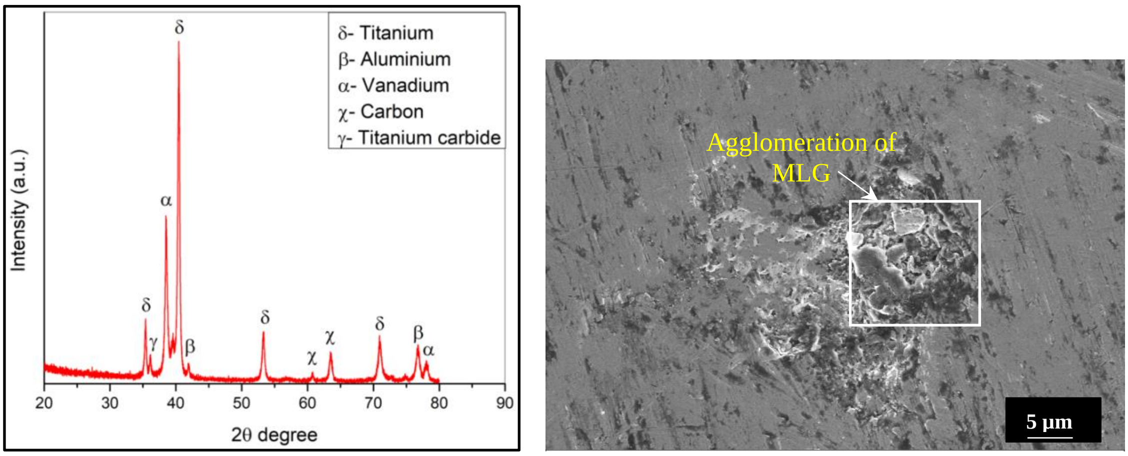

(a) **(b)**

Fig. 4.11 (a) XRD pattern of sintered nanocomposite **(b)** SEM image of nanocomposite fabricated at 1000 °C with 1.36 wt. % of MLG.

4.2.2 Tribological characterization

4.2.2.1 Analysis of variance for wear of sintered nanocomposites

A total of 13 experiments are designed using the CCRD method. Table 4.10 provides a detailed plan of experiments, along with the associated output response, i.e., wear rate (average of 3 readings). Also, a bare Ti6Al4V sample is fabricated to compare the properties with Ti6Al4V/MLG nanocomposite. The wear rate of the Ti6Al4V is 31.80 $\times 10^{-6}$ g/m.

Table 4.10 Detailed experimental design with wear rate.

Run	**Factors**		**Wear rate $\times 10^{-6}$ (g/m)**		**% error**
	Sintering temperature (°C)	wt. % of MLG	Experimental	Numerical	
1	1000	0.8	15.80	15.16	- 4.55
2	1000	0.23	24.00	24.51	- 2.13
3	1000	0.8	14.70	15.16	- 3.13
4	1150	1.2	15.20	16.25	- 6.91
5	850	0.4	25.00	24.09	3.64
6	1150	0.4	22.00	22.39	- 1.77
7	787	0.8	23.30	24.20	- 3.86
8	1000	0.8	15.30	15.16	0.92
9	1000	0.8	14.50	15.16	4.05
10	850	1.2	23.50	23.25	1.06
11	1212	0.8	19.00	17.99	5.32
12	1000	1.36	20.00	19.34	3.30
13	1000	0.8	15.51	15.16	2.26

ANOVA is used to estimate the percentage contribution of sintering temperature of SPS and wt.% of MLG content in establishing the wear rate of the nanocomposites. ANOVA for wear rate is shown in Table 4.11. The model p-value, Prob. > F for the response is < 0.0001, i.e., less than 0.05 (significance level, α for 95% confidence interval), implying that the model is significant. As shown in Table 4.11, during determining the wear rate of nanocomposites, wt. % of MLG ($B+B^2$) has the highest contribution of 48.72 %, followed by 46.22 % contribution of sintering temperature ($A+A^2$).

Table 4.11 ANOVA table for wear rate.

Source	Sum of squares ($\times 10^{-11}$)	D_f	Mean square ($\times 10^{-11}$)	F-value	P-value Prob. >F		% contri-bution
Model	19.30	5	3.87	49.04	< 0.0001	Significant	
A	3.78	1	3.77	47.87	0.0002	Significant	17.71
B	2.43	1	2.43	30.86	0.0009	Significant	11.42
A^2	6.08	1	6.08	77.08	< 0.0001	Significant	28.51
B^2	7.95	1	7.95	100.83	< 0.0001	Significant	37.30
AB	0.70	1	0.70	8.90	0.0204	Not significant	3.29
Residual	0.55	7	0.079				
Lack of Fit	0.43	3	0.14	4.80	0.0817	Not significant	1.78
Pure Error	19.89	4	0.03				
Cor Total	1.98	12					

A:Sintering temperature, B: wt. % MLG

Table 4.12 shows the statistical parameters of the model equations developed for wear rate. The developed model adequately explains the variation in the wear rate, which is 0.972, as given by R^2 (coefficient of determination). This implies that the experimental variables account for 97.20 % of the total variance in the measurement of wear rate. The adjusted R^2 value for wear rate is 0.952, indicating no need for additional terms in the model. The desired value for adequate precision is greater than 4.

Table 4.12 Statistical parameters of the model equation obtained from the ANOVA wear rate model.

Type of variable	Wear rate model
R^2	0.972
Adjusted R^2	0.952
Predicted R^2	0.836
Adequate precision	15.297

Results obtained after the parametric analysis of the SPS process during the fabrication of the TMCs are discussed in the present section. All the model terms upto 2nd order are considered in the regression model. The regression equation for wear rate in terms of input responses, i.e., Sintering temperature (A), and wt. % MLG (B) is as follows:-

$$Wear\ rate = 16.0395\text{x}10^{-5} - 2.59618\text{x}10^{-7}A - 1.60932\text{x}10^{-5}B$$
$$-2.21\text{x}10^{-8}AB + 1.314\ \text{x}10^{-10}A^2 + 2.11344\text{x}10^{-5}B^2 \qquad (4.8)$$

4.2.2.2 The normal probability plot of residuals for wear rate

Fig. 4.12 (a) shows the relationship between the actual response vs. the predictive response plot (wear rate). The values from the experimentation and prediction from the model are within acceptable limits. This confirms that the model is significant. The values of adj. R^2 (0.952) and R^2 (0.972) well justify the wear rate values distribution along the fit line. These values ensure that the model is fit to the experimental data. As shown in Fig. 4.12 (b) by the normal plot of residuals, most residuals fall on the straight line, implying that errors are normally distributed.

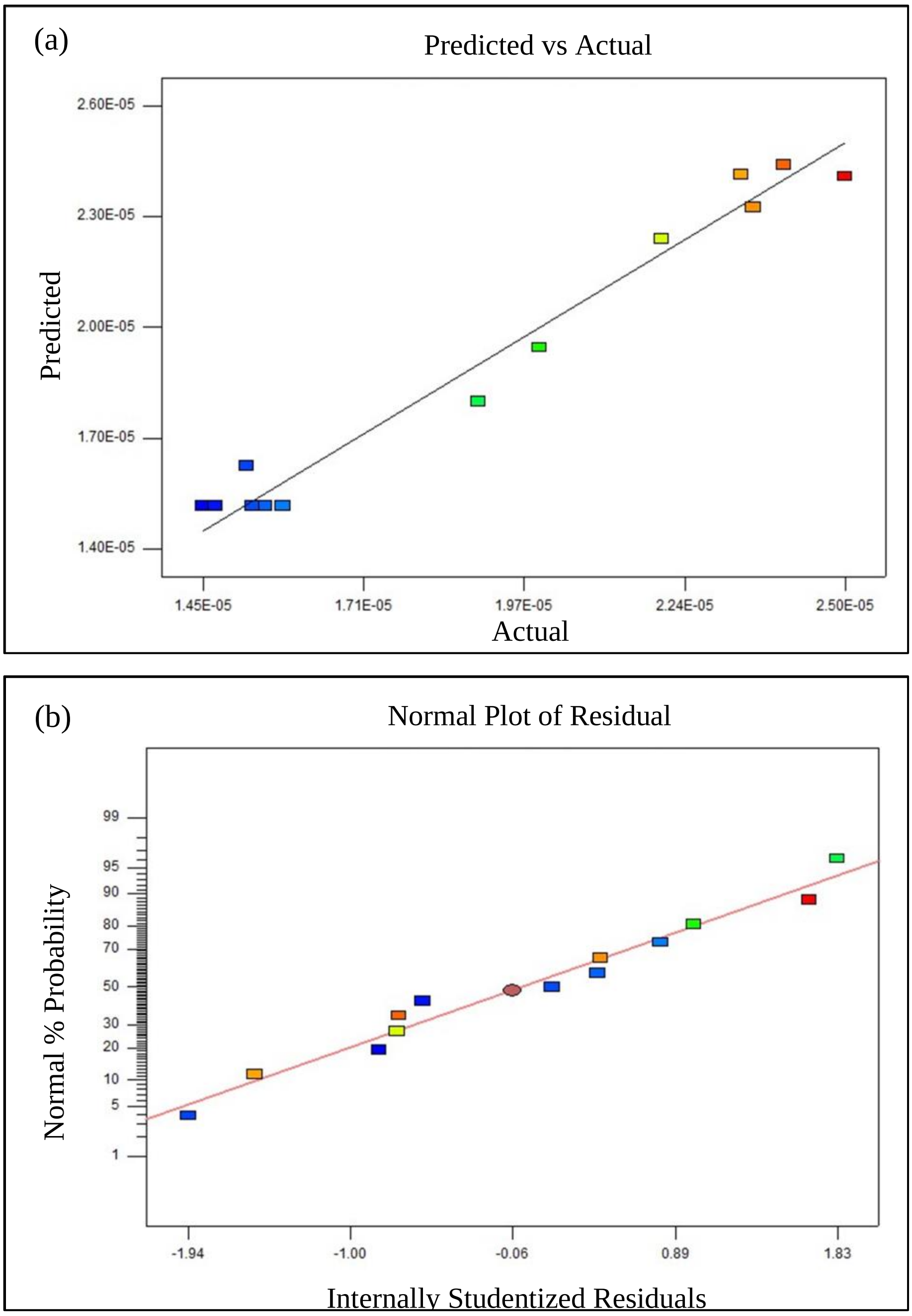

Fig. 4.12 (a) Actual response vs predictive response plots for wear rate **(b)** Normal plot of the residuals for wear rate.

4.2.2.3 Effect of sintering temperature on wear of sintered nanocomposites

The experimental studies revealed that as the sintering temperature of the nanocomposites increases, the wear rate gradually decreases (Fig. 4.13). The lowest wear rate of 14.50×10^{-6} g/m is obtained for nanocomposite sintered at 1000 °C. The primary cause for the nanocomposite's wear resistance improvement is the hardness enhancement of MLG-reinforced composites [105]. According to the Archad equation, the total volume of wear debris produced, *Q*, is inversely proportional to the hardness of the material, *H*, and is given as:-

$$Q = \frac{KWL}{H} \tag{4.9}$$

The variables *K*, *W*, and *L* in the above equation represent dimensionless constant, total normal load, and sliding distance. However, the wear rate tends to increase beyond a threshold value of sintering temperature (nearly 1050 °C). This increase in the wear rate value can be accounted for by the decrease in hardness due to the increase in grain size at an elevated sintering temperature. Fig. 4.14 shows the FESEM image of nanocomposites fabricated at 787 °C and 1000 °C with 0.8 wt. % MLG. The wear rate predominates more in nanocomposite fabricated at 787 °C when compared to its counterpart fabricated at 1000 °C. Fig. 4.14(a) shows more crater and wider grooves compared to Fig. 4.14(b), demonstrating a relatively softer surface that is more susceptible to wear.

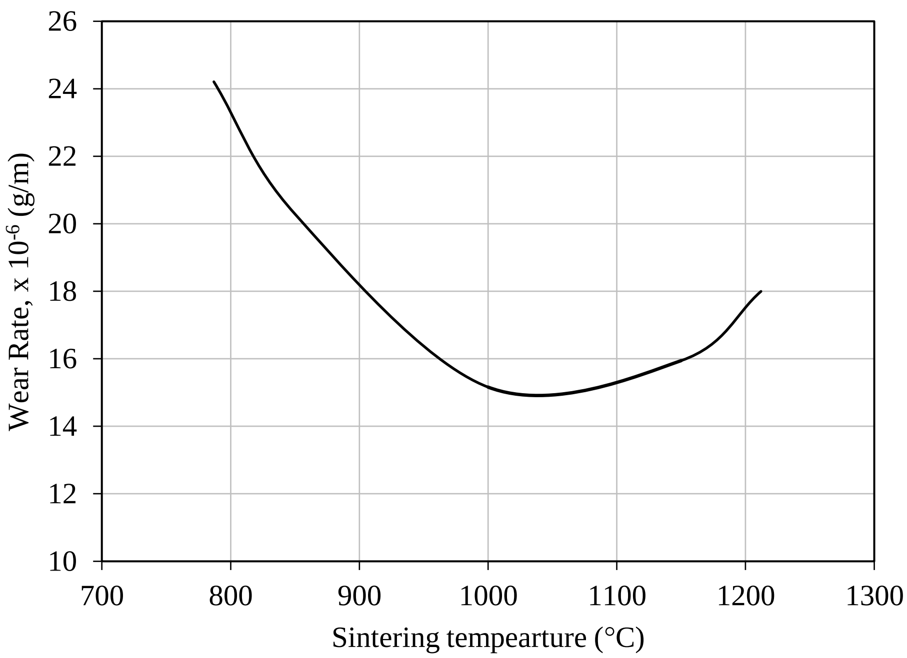

Fig. 4.13 Variation in wear rate with sintering temperature.

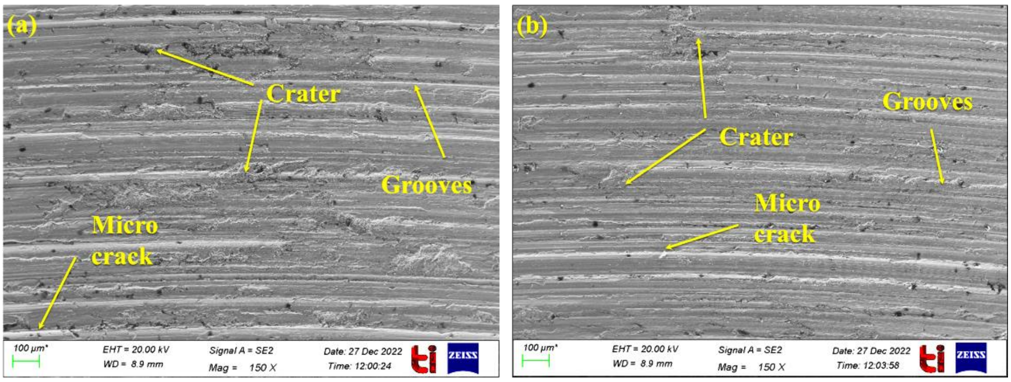

Fig. 4.14 FESEM image of nanocomposites fabricated at **(a)** 787° C and **(b)** 1000° C with 0.80 wt. % MLG.

4.2.2.4 Effect of wt. % of MLG on wear of sintered nanocomposites

As shown in Fig. 4.15, using MLG as reinforcement in TMCs results in a lower wear rate for a given applied load and sliding distance. For a constant applied load-sliding distance and various concentrations of MLG reinforcements, Ti6Al4V/0.8 wt.% of MLG nanocomposite exhibits superior wear characteristics compared to TMCs with lesser MLG content. Firstly, it is due to the better hardness of the TMCs with more MLG content. Additionally, due to the relatively higher hardness of Ti6Al4V/0.8 wt.%, the mechanical mix layer (MML) is more stable. Secondly, MLG has a lower density (2.52 g/cm^3) than Ti6Al4V (4.72 g/cm^3) and comprises more particles at a given reinforcing amount. Dislocations are created on the worn surface while sliding against the counter surface. However, they cannot advance because of the secondary particles. Due to the constraint imposed by intermetallic compounds or strengthened carbon particles, dislocations tend to accumulate around these particles, increasing strain hardening, plastic deformation resistance, and a decrease in wear rate.

The SEM/EDS images of wear tracks for sintered Ti6Al4V/0.23 wt.% MLG and Ti6Al4V/0.8 wt.% MLG nanocomposites tested at 5 kg loading conditions are shown in Fig. 4.16. The worn-out surfaces of TMCs exhibit delaminated areas, craters, and grooves. In comparison to fabricated nanocomposites with 0.8 wt.% of MLG, the one with 0.23 wt.% of MLG exhibits severe surface damage, likely due to a relatively larger number of micro-cracks and less stability of MML. The grooves on worn surfaces indicate the entrapment of wear debris underneath. Three-body abrasive wear is caused by the entrapment of wear particles that plow the worn surface with hardened wear debris. The EDS results further prove the less stability of MML in the case of nanocomposites with 0.23 wt.% of MLG, as the iron (Fe) content is less in Fig. 4.16(a) than in Fig. 4.16(b). The presence of Fe, however, confirms the transfer of material from the counter body to the material in both cases.

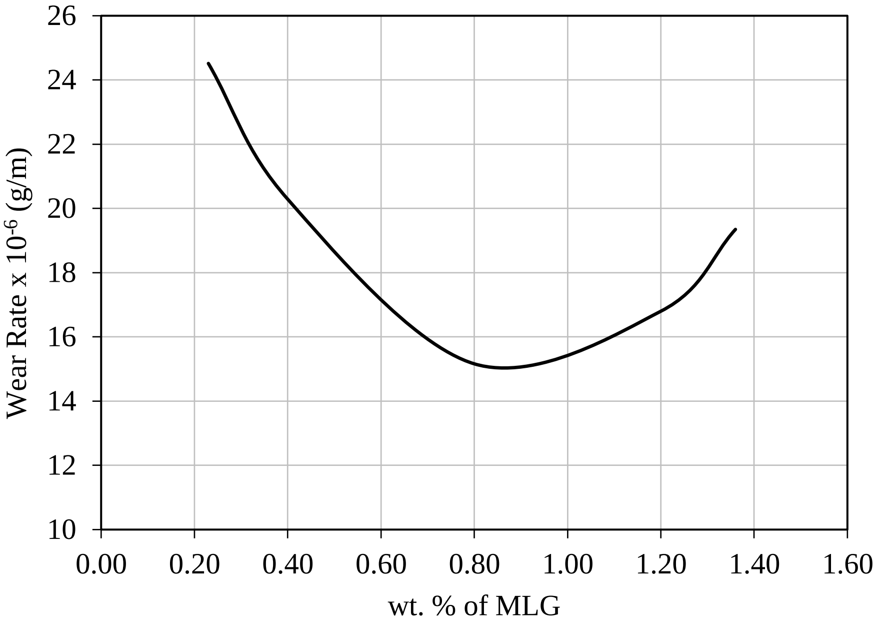

Fig. 4.15 Variation in wear rate with MLG content.

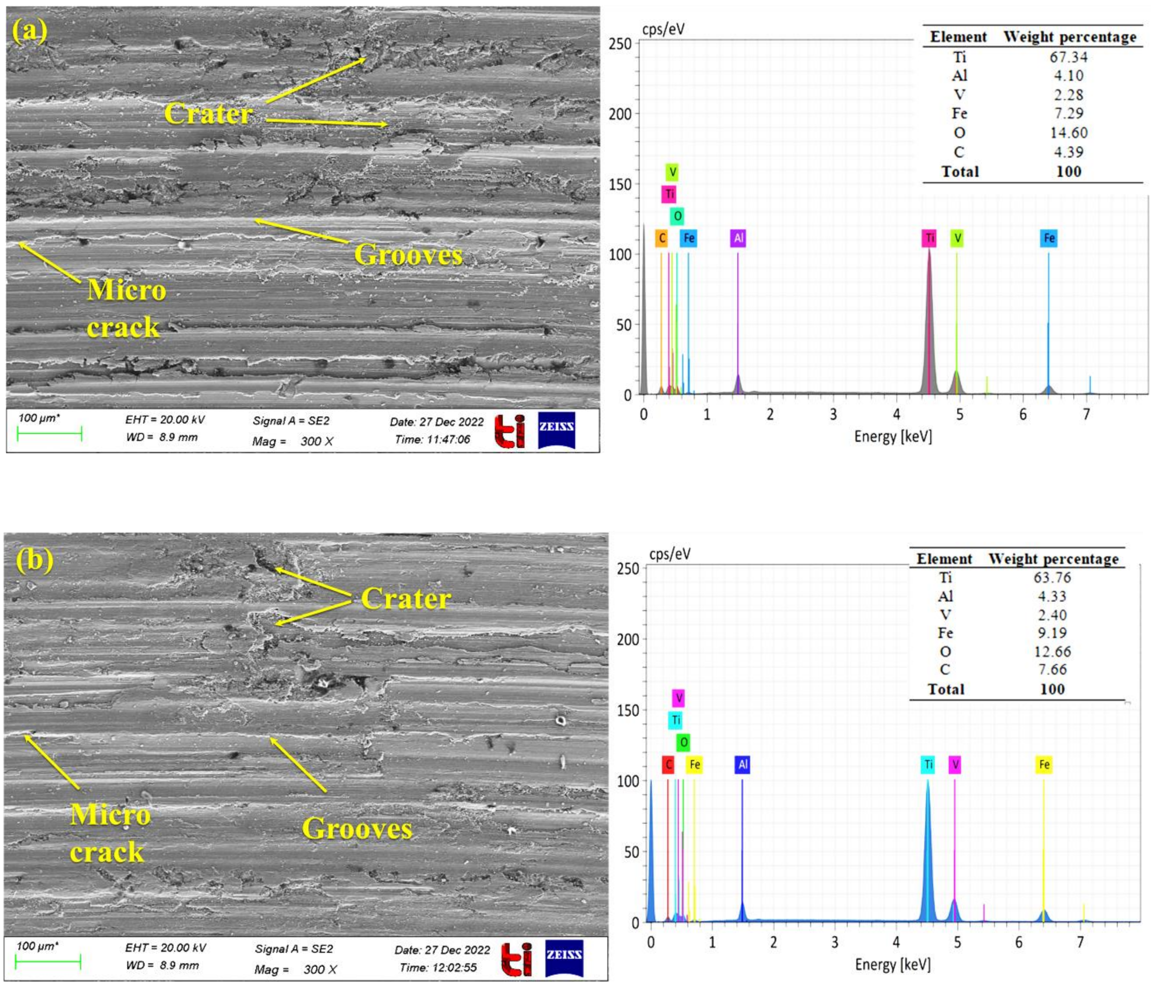

Fig. 4.16 FESEM with EDS image of nanocomposites fabricated at different MLG wt. % **(a)** 0.23 and **(b)** 0.80 at a sintering temperature of 1000 ° C.

4.2.3 Corrosion characterization

4.2.3.1 Analysis of variance for corrosion of sintered nanocomposites

Table 4.13 displays the experimental design together with the corresponding output response, i.e., corrosion current density. In addition, the corrosion current density of bare Ti6Al4V is 3.14 µAcm$^{-2,}$ which is reduced to a minimum of 1.45 µAcm$^{-2,}$ corresponding to a 53.82 % improvement for Ti6Al4V/0.8 wt. % MLG fabricated at 1000 °C. Table 4.14 shows the ANOVA table for the developed model's corrosion current density. According to the response model, the *F*-value is 34.89, and the corresponding P-value is < 0.0001, which suggests the model is significant. Therefore, the high "model F-value" could not be attributed to noise, and the quadratic model is significant at the 95 % confidence level.

Table 4.13 Detailed experimental design with output responses for corrosion current density.

Run	**Factors**		**Corrosion current density**		**% error**
	Sintering temperature (°C)	wt. % of MLG	Experimental	Numerical	
1	1000	0.8	1.47	1.52	-3.40
2	1000	0.23	2.58	2.65	-2.71
3	1000	0.8	1.60	1.52	5.00
4	1150	1.2	1.50	1.56	-4.00
5	850	0.4	2.80	2.64	5.71
6	1150	0.4	2.15	2.16	-0.47
7	787	0.8	2.30	2.47	-7.39
8	1000	0.8	1.62	1.52	6.17
9	1000	0.8	1.45	1.52	-4.83
10	850	1.2	2.46	2.34	4.88
11	1212	0.8	1.65	1.57	4.85
12	1000	1.36	1.99	2.01	-1.01
13	1000	0.8	1.49	1.52	-2.01

Furthermore, it can be seen from the ANOVA table that the sintering temperature and the wt. % of MLG was found to be crucial parameters in deciding the output response. While determining the corrosion current density of the sintered nanocomposites, the contribution of sintering temperature ($A + A^2$) and wt. % of MLG ($B + B^2$) was 43.44 % and 54.75 %, respectively. Further, the lack of fit value of 4.44 implies that it is insignificant relative to pure error, showing that the models accurately accounted for the experimental data. The regression equation for predicting the corrosion current density, I_{corr} of sintered nanocomposites as a function of sintering temperature (A) and wt. % of MLG (B) is given as:-

$$Corrosion\ current\ density = 15.73307 - 0.0232A - 3.3172B - 0.00129AB + 1.10611\text{x}10^{-5}A^2 + 2.524219B^2 \quad (4.10)$$

Table 4.14 ANOVA table for corrosion current density.

Source	Sum of squares	D_f	Mean square	F-value	P-value		% contri-bution
Model	2.64	5	0.53	34.89	< 0.0001	Significant	
A	0.80	1	0.80	52.70	0.0002	Significant	28.08
B	0.42	1	0.42	27.42	0.0012	Significant	14.60
A^2	0.43	1	0.43	28.40	0.0011	Significant	15.10
B^2	1.13	1	1.13	74.79	< 0.0001	Significant	39.85
AB	0.02	1	0.02	1.58	0.2486	Not significant	0.84
Residual	0.11	7	0.02				
Lack of Fit	0.08	3	0.03	4.44	0.0919	Not significant	
Pure Error	0.02	4	0.01				0.21
Cor Total	2.75	12					

The statistical parameters for the model equations are shown in Table 4.15. Using R^2 (coefficient of determination), the reduction of response variability for corrosion current density was calculated to be 0.961. This indicates that the experimental input parameters account for 96.14 % of the total variance in measuring corrosion current density.

Table 4.15 Statistical parameters of the model equation obtained from the ANOVA model of corrosion current density.

Type of variable	Corrosion current density model
Standard deviation (SD)	0.123
Mean	1.928
R^2	0.961
Adjusted R^2	0.934
Predicted R^2	0.775
Adequate precision	13.507

The model best fits the data because the R^2 value is near to 1. The corrosion current density measurement model's standard deviation (SD) is 0.123. The value of 0.934, which corresponds to the adjusted R^2 for the corrosion current density measurement, indicates no requirement for any additional term in the regression equation model. The model's value of adequate precision, 13.507, demonstrates that it is fit.

4.2.3.2 The normal probability plot of residuals for corrosion current density

Fig. 4.17 (a) shows the relationship between the actual response vs. predictive response plots, and Fig. 4.17 (b) shows the normal plot of the residuals for corrosion current density. The experimental and model-predicted values exhibit remarkable closeness, validating the significance of the model. The adjusted R-squared value of 0.934 and the R-squared value of 0.961 strongly support the assertion that wear rate values are uniformly distributed along the fitted line. These values prove that the model is well-suited to the experimental data. In addition, the unbiased nature of the predicted corrosion current density is demonstrated by the normally distributed residual plot.

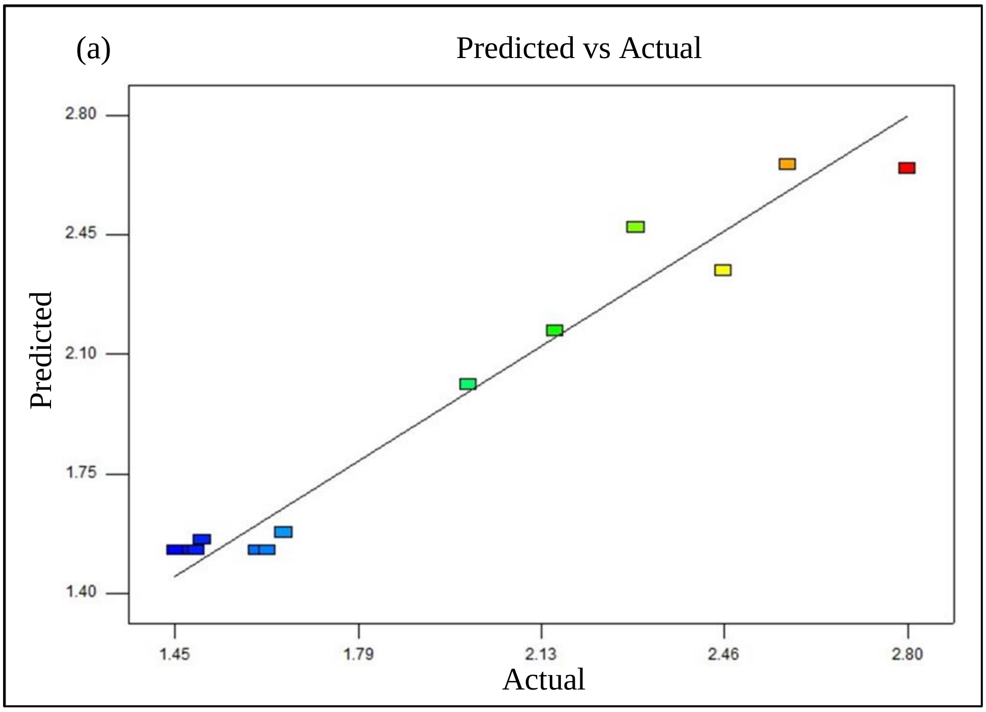

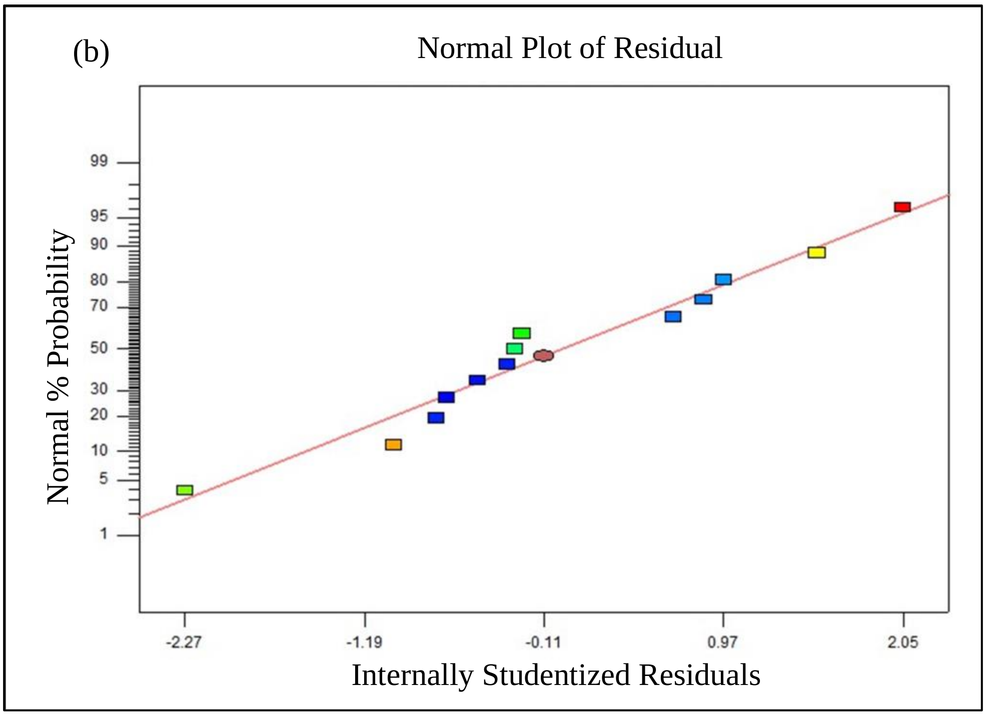

Fig. 4.17 (a) Actual response vs. predictive response plots for corrosion current density **(b)** Normal plot of the residuals for corrosion current density.

4.2.3.3 Effect of sintering temperature on corrosion of sintered nanocomposites

Fig. 4.18 illustrates the relationship between sintering temperature and corrosion current density, indicating that the corrosion current density decreases with temperature until it reaches nearly 1100 °C, thereafter, it starts increasing. This decrease in corrosion current density indicates improved resistance of the fabricated composites against the corrosion. As the sintering temperature increases, the nanocomposite's hardness improves. Nanocomposites with high hardness tend to have lower corrosion current density, indicating a lower corrosion rate. This is because harder materials often possess a more compact and dense microstructure, which provides better resistance against corrosive reactions. Also, it was evident that with the increase in the sintering temperature beyond 1100 ℃, there is a slight increase in the corrosion current density. It is primarily due to the increased grain size of the nanocomposite, which adversely affects its hardness as well as corrosion resistance.

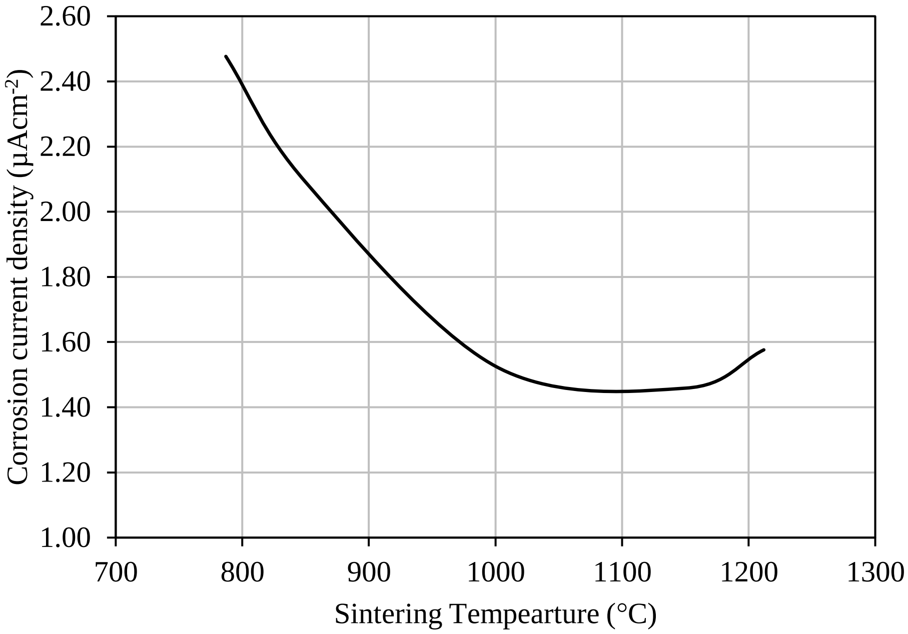

Fig. 4.18 Variation in corrosion current density with sintering temperature.

Fig. 4.19 shows the potentiodynamic polarization curves of Ti6Al4V/0.8 wt. % MLG nanocomposites sintered at 787 °C and 1000 °C. The corrosion potential, E_{corr}, and corrosion current density estimated from these curves is -163 mV, 2.30 µAcm^{-2} for nanocomposites with sintering temperature 787 °C, while -273.10 mV, 1.62 µAcm^{-2} for nanocomposite fabricated at 1000 °C (Table 4.16). This indicates more stable passive oxide film formation on the nanocomposite surface with higher sintering temperatures [106]. Therefore, the corrosion rate of Ti6Al4V/0.8 wt. % MLG nanocomposite sintered at 1000 °C is 0.014 mm/year, while that of nanocomposite sintered at 787 °C is 0.020 mm/year.

Table 4.16 Corrosion parameters obtained for Ti6Al4V/MLG nanocomposites from polarization curves

Nanocomposite	**ST (°C)**	E_{corr} ***(mV)***	I_{corr} **(µAcm^{-2})**	**Corrosion rate (mm/year)**
Ti6Al4V/0.8 wt. % MLG	787	-163	2.30	0.014
Ti6Al4V/0.8 wt. % MLG	1000	-273.10	1.62	0.020

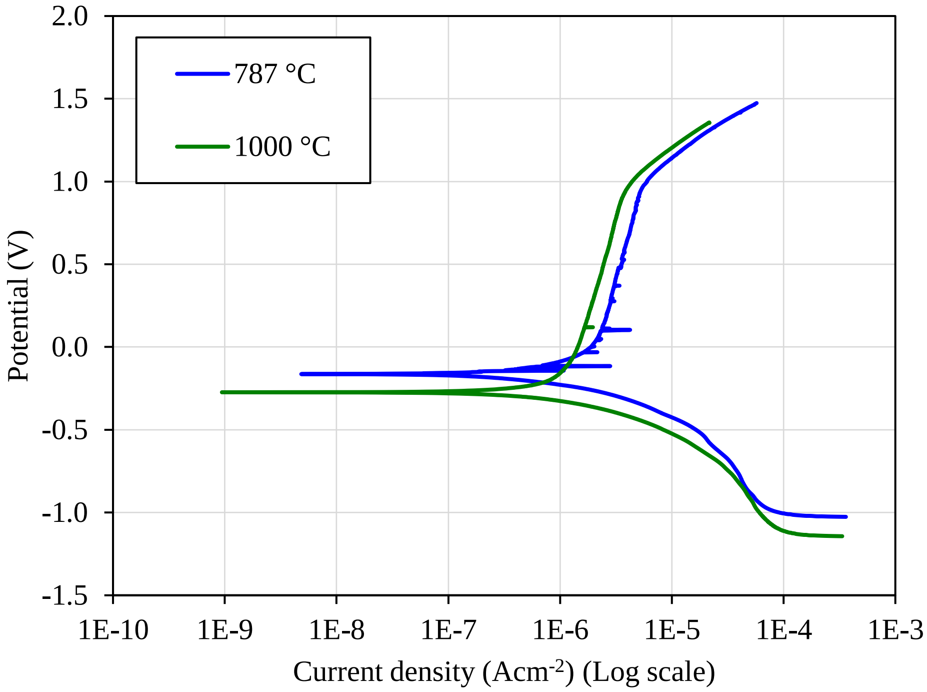

Fig. 4.19 Potentiodynamic polarization curves for 0.80 wt.% MLG nanocomposites sintered at 787 °C and 1000 °C.

4.2.3.4 Effect of wt. % of MLG on corrosion of sintered nanocomposites

Fig. 4.20 shows the effect of varying wt. % of MLG on corrosion current density. Increasing the MLG content to nearly 0.8 wt. % leads to a decline in corrosion current density with a minimum value of around 1.45 μAcm^{-2}. However, beyond 0.8 wt. %, the corrosion current density starts to increase. The decrease in the corrosion current density, or in other words, the improvement in the corrosion properties of nanocomposites, is due to the formation of the carbide phase with the addition of reinforced graphene. The formation of titanium carbides (TiC) in the nanocomposites due to the in-situ reaction of Ti and C during sintering increases the value of responses. TiC is highly corrosion resistant, and its content increases with the increase in wt. % of MLG [107]. Uniform dispersion of MLG into the matrix results in better corrosive properties of nanocomposites. However, after a threshold MLG content in the Ti6Al4V matrix, its agglomeration occurs, increasing the corrosion current density in nanocomposites. As shown in Fig. 4.21 (a), the corrosion is more dominant on the Ti6Al4V/0.23 wt. % MLG nanocomposite compared to the improved corrosion resistance offered by the Ti6Al4V/0.80 wt. % MLG nanocomposite (Fig. 4.21 (b)).

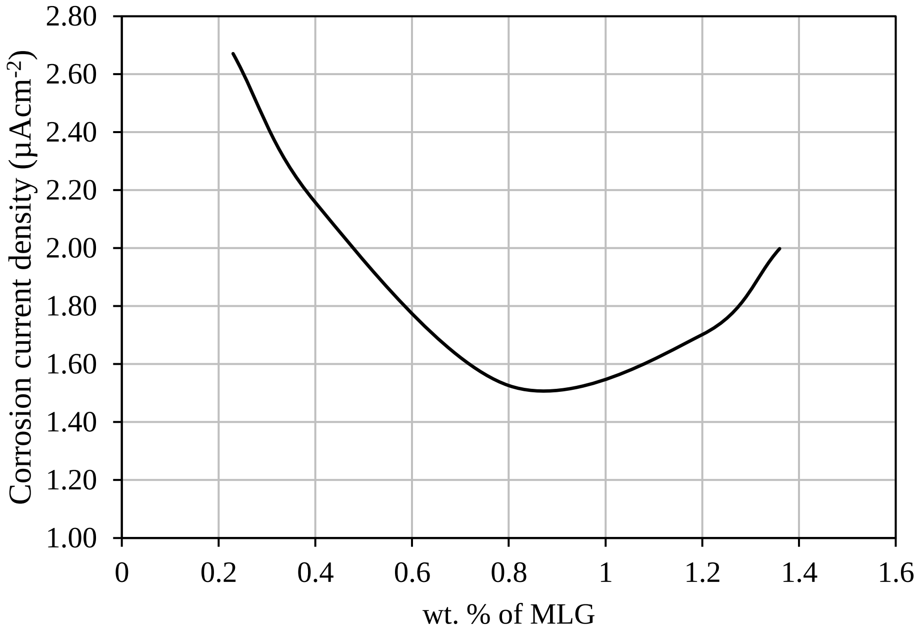

Fig. 4.20 Variation in corrosion current density with MLG content.

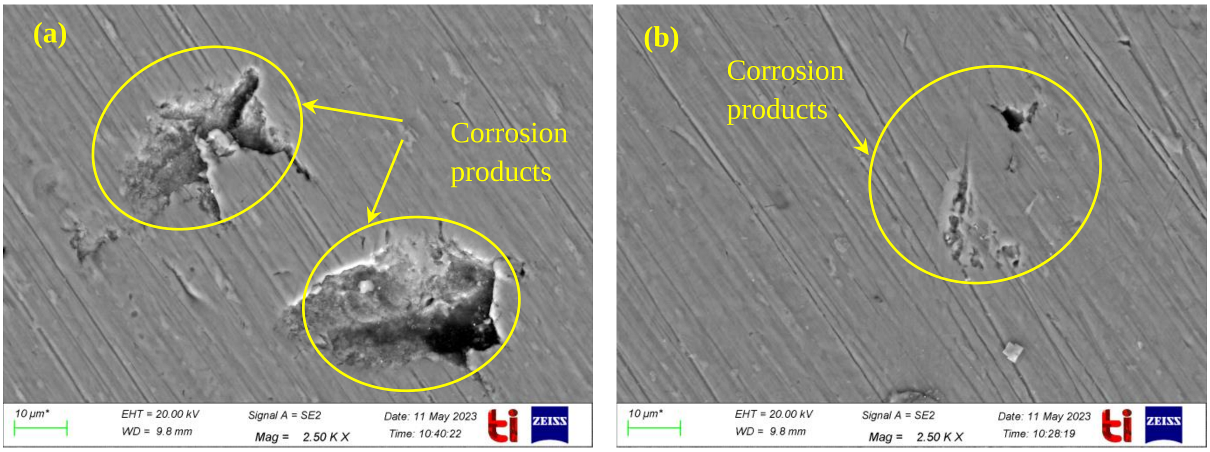

Fig. 4.21 FESEM image of nanocomposite surface after corrosion for different MLG wt. % **(a)** 0.23 and **(b)** 0.80 at a sintering temperature of 1000 °C.

Electrochemical impedance spectroscopy (EIS) results in Fig. 4.22 show a comparison between the Ti6Al4V/0.23 wt. % MLG and Ti6Al4V/0.80 wt. % MLG nanocomposite. Nanocomposite with 0.80 wt. % of MLG possesses higher impedance with a maximum of 6×10^4 Ω, compared to nanocomposite with a 0.23 wt. % of MLG. In addition, high capacitive behavior with a maximum phase angle close to – 68°, indicating superior corrosion resistance is demonstrated by Ti6Al4V/0.80 wt. % MLG nanocomposite Fig. 4.22 (b).

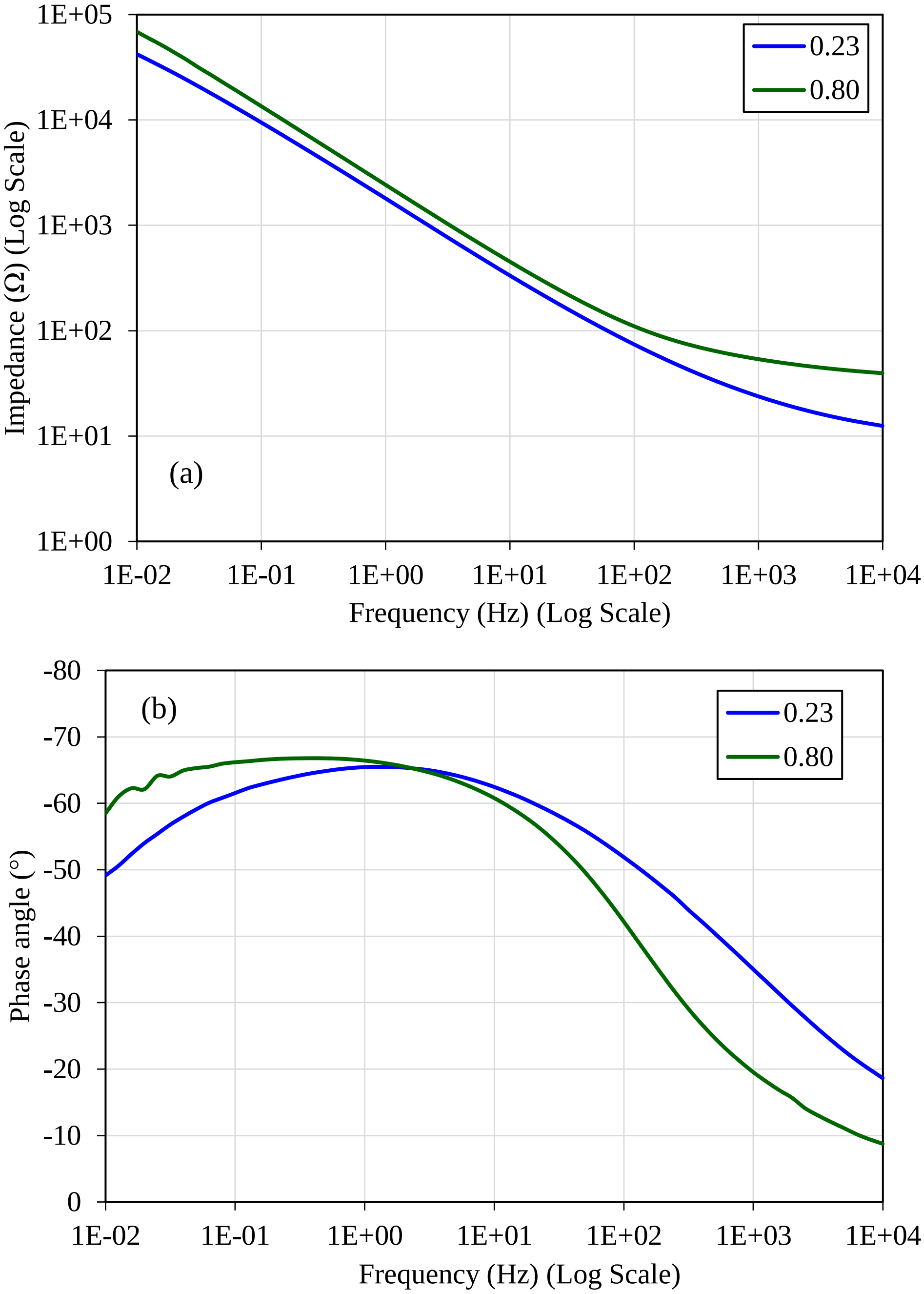

Fig. 4.22 Bode plot for Ti6Al4V/MLG nanocomposite **(a)** Frequency vs. impedance **(b)** Frequency vs. phase angle.

Table 4.17 Comparative analysis of present work with published literature.

S. No.	Authors	Material	% Decrease in Wear Rate	% Decrease in I_{corr}
1.	Present Study	Ti6Al4V/MLG	54.40 %	53.82 %
2.	Gürbüz et. al. [49]	Ti/GNP	32.10 %	-
3.	Izui et. al. [57]	Ti6Al4V/$TiC_{0.7}N_{0.3}$	~ 35 %	-
4.	Mordyuk et. al. [73]	Ti6Al4V/Al_2O_3/TiO_2	-	47.36 %
5.	Anawati et. al. [67]	Ti/HA	-	19.04

Table 4.17 shows the comparative study of wear rate and corrosion current density in the present study with that of reported in various literature.

4.2.4 Finishing of nanocomposites

Various researchers have studied the effects of surface finishing on the wear properties of composites. Their study revealed that surface finishing can significantly improve their surface characteristic, especially surface roughness, R_a, thereby enhancing their functionality [108]. For example, fine surface roughness on the nanocomposite's surface improves the frictional resistance between the nanocomposite material and its contact surface during relative motion. As a result, the wear rate decreases, and the material's lifespan increases. Experimental studies showed the mechanical, wear, and corrosion properties of the Ti6Al4V/0.8 wt. % MLG nanocomposite with a sintering temperature of 1000 °C was better compared to its counterpart. Therefore, considering this as the best fabricated TMC, surface finishing was done on the same using the abrasive flow finishing (AFF) process. The initial surface roughness of the workpiece is in the range of 3.75 ± 0.15 μm. The effect of percentage change in the surface roughness, % ΔR_a, was evaluated with respect to various input parameters of the AFF process (number of cycles, wt.% of the abrasive particle, and mesh size of abrasive material) and is given as:-

$$\% \, \Delta R_a = \frac{Initial\ surface\ roughness - Final\ surface\ roughness}{Initial\ surface\ roughness} \times 100 \qquad (4.11)$$

The current study uses an economically developed AFF media to conduct AFF experiments. The AFF medium is primarily viscoelastic. It serves as a matrix to contain the abrasive particles that shear the peaks of surface roughness. Using a two-roll mill set-up, all of the media's ingredients are appropriately combined. Two chromium-plated rollers with a tiny space between them make up the two-roll mill. Repetitive passage of media constituents across the gap occurs as soon as the rollers begin rolling. First, properly mixing the polymers constitutes the base media is done. Subsequently, the mixture is mixed with abrasive particles and different additives in the proper amounts (Fig. 4.23).

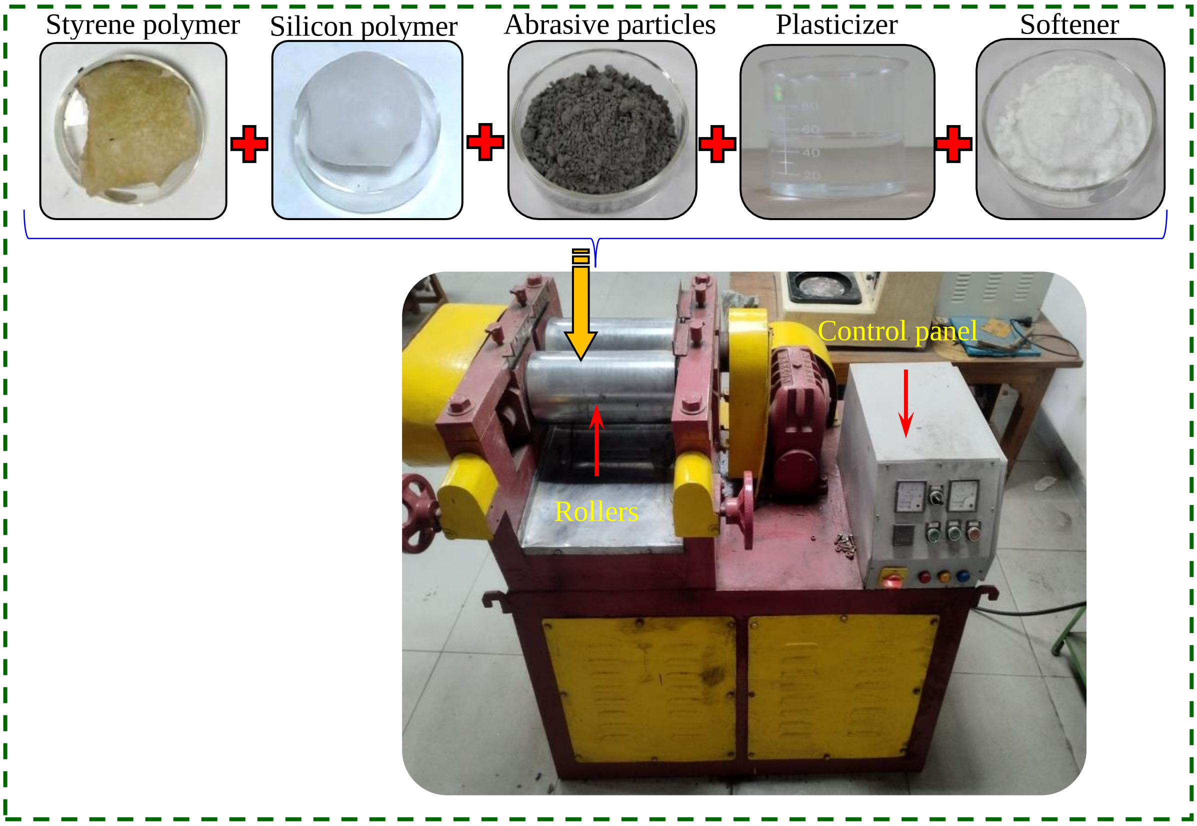

Fig. 4.23 Various ingredients with two-roll mill machine used for developing AFF media.

In the current thesis, styrene-butadiene polymer (SBP) and silicon polymer (SP) act as the viscoelastic matrix of the developed media. Later, various additives (plasticizers and softeners) and abrasive particles are added to the AFF media. Five different compositions of the media are prepared with varying wt. % of abrasive particles (Table 4.17).

Table 4.18 Various AFF media compositions (wt. %) prepared for finishing TMC.

Media composition	SBP	SP	Abrasive particles	Plasticizers	Softeners
1.	20.00	35.00	30.00	8.00	7.00
2.	18.57	32.50	35.00	7.43	6.50
3.	17.14	30.00	40.00	6.86	6.00
4.	15.71	27.50	45.00	6.29	5.50
5.	14.29	25.00	50.00	5.71	5.00

4.2.4.1 Effect of number of cycles on surface roughness of nanocomposites

The number of cycles in AFF refers to the number of times the abrasive media is passed through the workpiece during the finishing process. As the AFF cycles increase, the frequency of the abrasive particles to shear the roughness peaks increases. As a result, increasing the number of cycles, the $\% \Delta R_a$ of the TMCs increases (Fig. 4.24). A significant increase in the $\% \Delta R_a$ of the TMCs was observed for the number of AFF cycles up to 75. Thereafter, the increase in the $\% \Delta R_a$ was inconsequential. The impact of temperature on the media's shear viscosity is primarily responsible for reducing the rate of change in $\% \Delta R_a$ [109]. At high AFF cycles, there is a considerable increase in the finishing time during which heat is generated due to continuous shearing of the surface roughness peaks and the friction between the media and the TMC surface. Polymer based viscoelastic media becomes less viscous at high temperatures and loses its capacity to hold the abrasive particles effectively. Thus, the finishing capability of the media reduces at high temperatures.

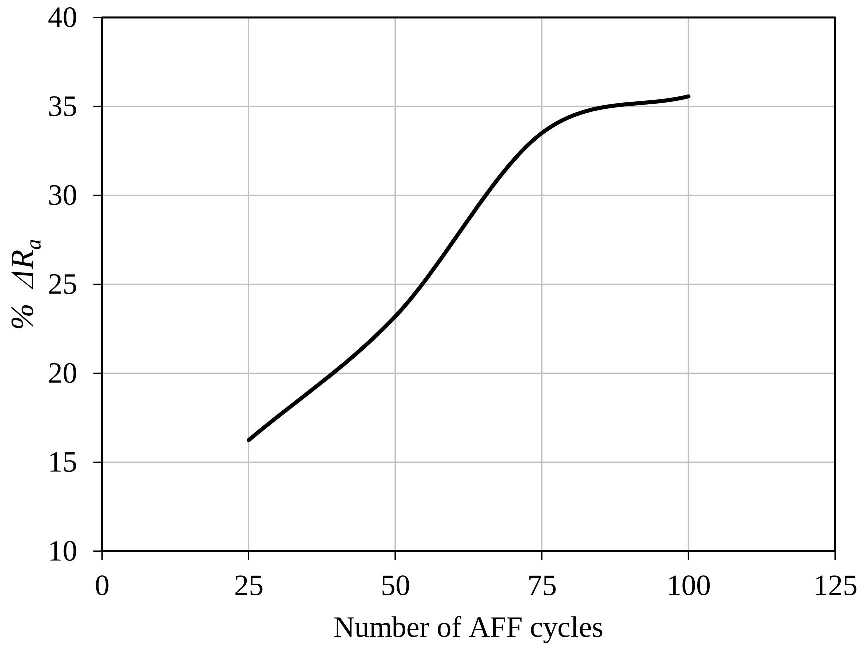

Fig. 4.24 Variation of the percentage improvement in surface roughness value with the number of cycles (30 wt. % of abrasive particles, 600 mesh size).

Fig. 4.25 shows the 2D surface profile of TMC after finishing at various numbers of AFF cycles. As the number of AFF cycles increases, the height of high roughness peaks decreases. Thus, it is evident that the surface roughness improves with the increase in AFF cycles.

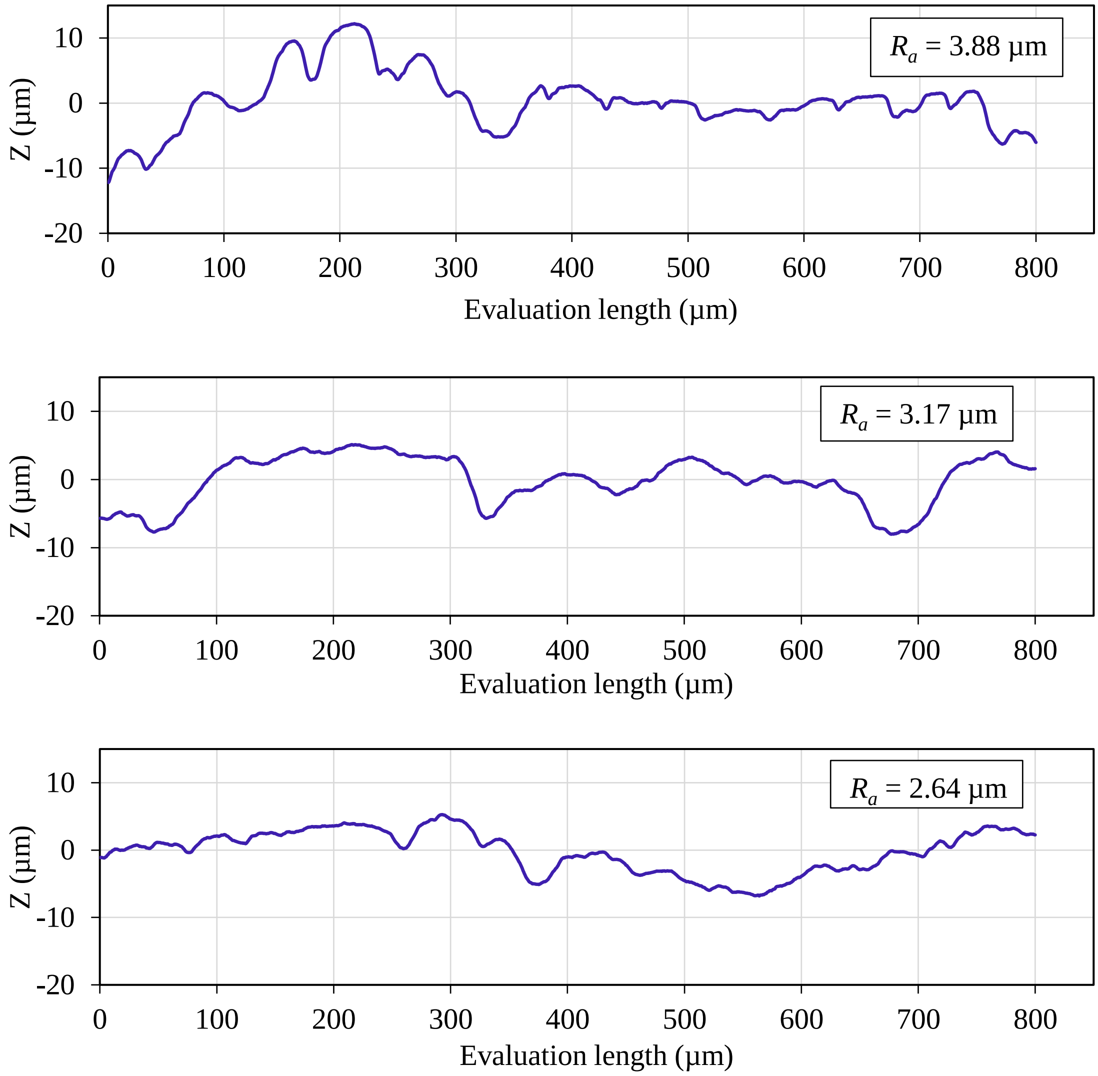

Fig. 4.25 2D surface profiles for various AFF cycles **(a)** Initial **(b)** 25 **(c)** 75.

4.2.4.2 Effect of wt.% of the abrasive particle on surface roughness of nanocomposites

The abrasive particles help finish the TMC's surface by shearing the surface roughness peaks. Higher the wt. % of the abrasive particles in the media more are the abrasive particles per unit time taking part in the shearing of the roughness peaks. Therefore, as shown in Fig. 4.26, an increase in the wt.% of abrasive particles results in the improvement of $\% \Delta R_a$. However, as the wt. % of abrasive particles is increased beyond a threshold, i.e., 45 %, $\% \Delta R_a$ declines. This is primarily because at high wt. % of abrasive particles, the amount of base polymer decreases, and there won't be enough polymer chains to hold the abrasive particles effectively. Thus, the finishing forces generated in the media are not effectively transferred by the polymer chains to the abrasive particles that shear the surface roughness peaks.

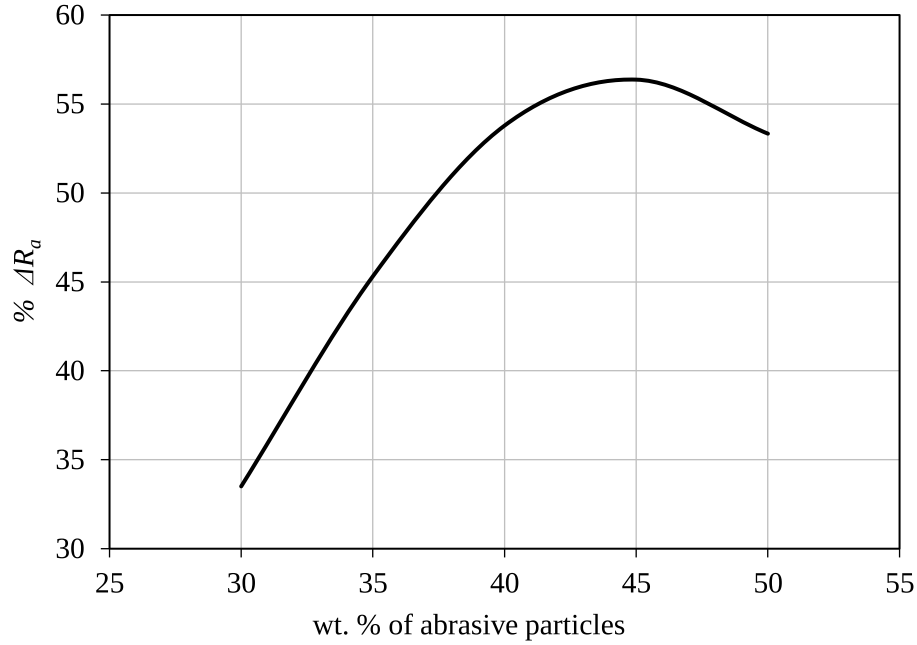

Fig. 4.26 Variation of the percentage improvement in surface roughness with wt. % of the abrasive particles (75 AFF cycles, 600 mesh size).

Fig. 4.27 shows that TMC finished with 45 wt. % abrasive media has a more fine finished 2D surface roughness profile compared to that of TMC finished with 35 wt. % abrasive media.

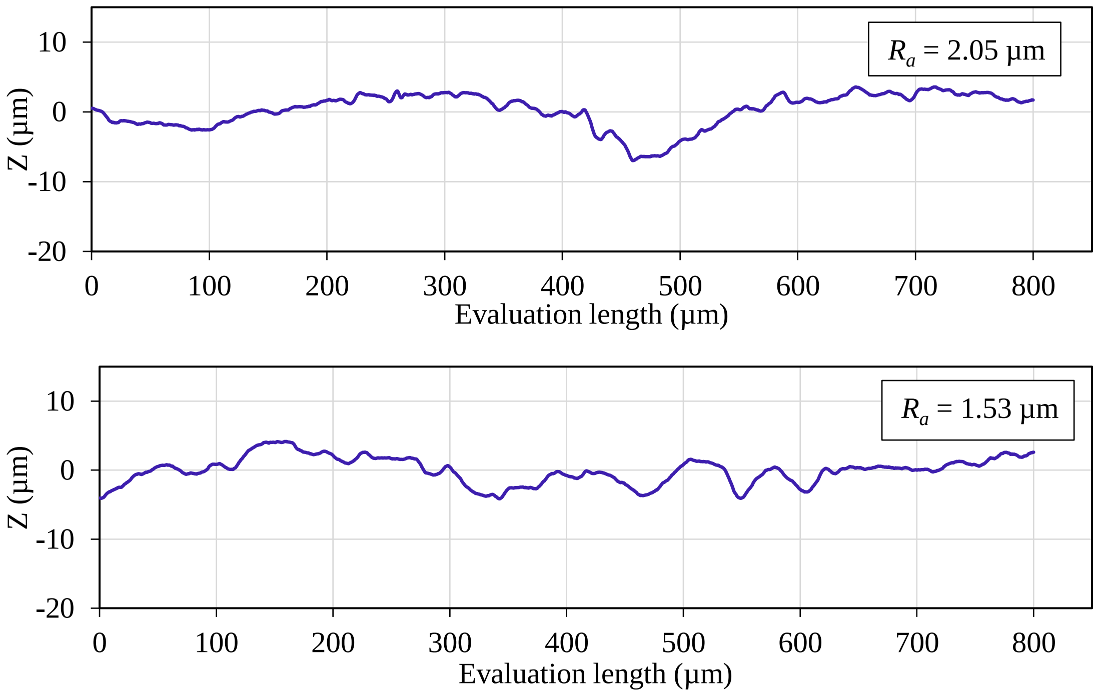

Fig. 4.27 2D surface profiles for wt.% of abrasive particles **(a)** 35 **(b)** 45.

4.2.4.3 Effect of mesh size of abrasive material on surface roughness of nanocomposites

The mesh size of the abrasive particle plays a vital role in deciding the final roughness of the workpiece's surface. The relation between mesh size, *M*, and abrasive particle size, R_{ap}, radius of the abrasive particle) is given as [110]:-

$$R_{ap} = \frac{7.62}{M} \tag{4.12}$$

As shown in Fig. 4.28, with the decrease in the mesh size of the abrasive particle, the $\% \Delta R_a$ of the TMCs increases. As the mesh size increases, the size of the abrasive particles decreases. As a result, the abrasive particle's penetration depth and width into the workpiece surface decreases. Therefore, the improvement in R_a is less for the higher mesh size abrasive particles. According to the findings of the experiments, the greater the size of the abrasive particle, the more efficiently it shears the surface roughness peak. A maximum improvement of 73.20 % corresponds to a minimum 0.94 µm R_a of the TMC by finishing it with 220 mesh size abrasive particles is achieved (Fig. 4.29).

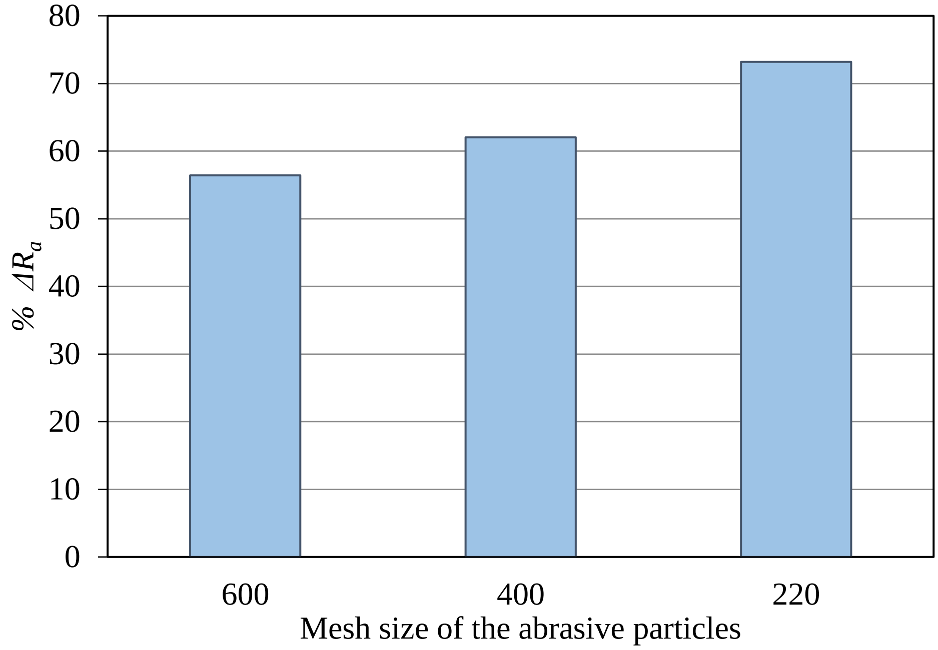

Fig. 4.28 Variation of the percentage improvement in surface roughness with mesh sizes of the abrasive particles (75 AFF cycles, 45 wt. % of abrasive particles).

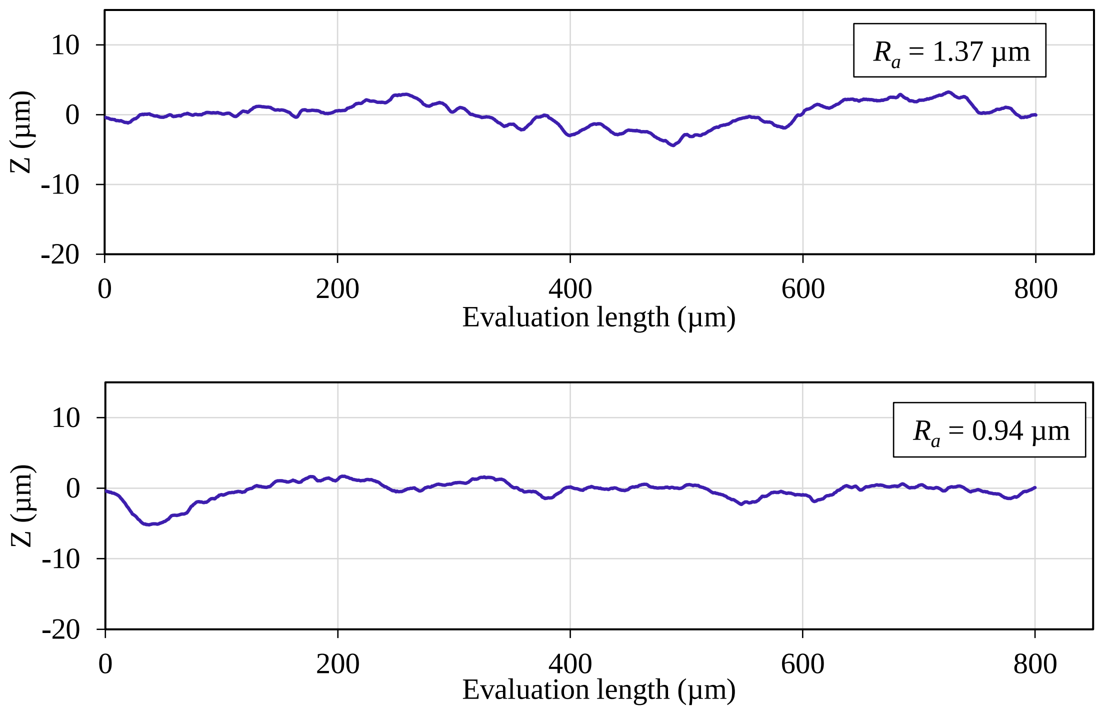

Fig. 4.29 2D surface profiles for mesh size of abrasive particles **(a)** 400 **(b)** 220.

CHAPTER 5

CONCLUSIONS AND FUTURE SCOPE

TMCs have been fabricated using the SPS process in the reported thesis work. Various input parameters were varied to study their effect on different output responses. The metallographic characterization, mechanical testing, wear, and corrosion finishing study were conducted on various TMC samples. The major conclusion of the current research work, along with the future scope, is listed in this chapter.

5.1 Conclusions drawn from microstructural and mechanical characterization

1. In the current work, TMCs with enhanced mechanical properties were successfully fabricated by using the SPS process. It can be concluded that MLG plays a vital role in improving the mechanical properties of TMCs.
2. Sintered nanocomposites' hardness and elastic modulus increase with increasing sintering temperature and MLG content. The improved mechanical properties can be accredited to the enhanced density, grain refinement, and formation of TiC.
3. Grain growth at an elevated temperature around 1100 °C leads to a decline in hardness and elastic modulus. Also, at higher wt. % of MLG (i.e., around 0.9 %), its agglomeration occurs, which results in a decline in mechanical properties.
4. The parametric study of the SPS process shows that sintering temperature and wt.% of MLG contribute 42.15 % and 55.40 %, respectively, in determining the hardness of the fabricated nanocomposites.
5. The ANOVA shows that sintering temperature and wt. % of MLG have almost the same contribution, viz. 49.24 % and 48.61% in deciding the elastic modulus of nanocomposites.

5.2 Conclusions drawn from tribological and corrosion characterization

1. Nanocomposites' tribological and corrosive properties were enhanced with increased wt.% of MLG and sintering temperature. However, a decline in the properties is observed beyond a threshold value.
2. Densification of nanocomposites, grain refinement, and the formation of TiC were the primary reasons for the improved properties.
3. A minimum wear rate of 14.50 $x10^{-6}$ g/m and corrosion current density of 1.45 μAcm^{-2} is achieved for the Ti6Al4V/0.8 wt.% MLG nanocomposite sintered at

1000 °C. This corresponds to a 54.40 % and 53.82 % improvement compared to bare Ti6Al4V.

4. ANOVA concluded that wt. % of MLG is the dominating input parameter. It contributes 48.72 % and 54.75 % in determining wear rate and corrosion current density, respectively.
5. Sintering temperature contributes 46.22 % and 43.44 % to influencing sintered nanocomposites' wear rate and corrosion current density, respectively.

5.3 Conclusions drawn from finishing characterization

1. There is a considerable change in $\% \Delta R_a$ of around 34 % till finishing with 75 AFF cycles.
2. As the wt. % of the abrasive particles in the AFF media increases, there is an improvement in $\% \Delta R_a$. However, beyond a threshold, i.e., 45 wt. %, $\% \Delta R_a$ decreases due to the insufficient polymer chains in the media to hold the abrasive particles.
3. A decrease in the mesh size of the abrasive particles results in an improvement of $\% \Delta R_a$. This is primarily due to the bigger cutting edges of the smaller mesh size abrasive particles that help in effectively shearing the roughness peaks.
4. Significant improvement in the surface roughness of TMCs was achieved. A maximum $\% \Delta R_a$ of 73.20 % was recorded for 75 AFF cycles, 45 wt. % of 220 mesh size abrasive particles.

5.4 Future scope of the present thesis work

In addition to the present work, the fabricated TMCs can be tested for tribological and corrosion testing under simulated body fluids to confirm their application in biomedical. Also, a numerical model can be developed to simulate the SPS process. A developed numerical model can replace expensive and time-consuming experiments if it can accurately predict the effect of input parameters on the output responses. In the current work for the design of AFF setup various assumptions and higher FOS was taken. In future the design of the setup can be done using any design software to make it more accurate and economical.

List of Publications

Following are the SCI journal published from current work:-

1. **D. Sharma**, V.K. Singla, S. Singh, Effect of multilayer graphene on microstructure and mechanical properties of titanium-based composites, Proc IMechE Part C: J Mechanical Engineering Science. 236 (2022) 8542-8551.

2. **D. Sharma,** V.K. Singla, S. Singh, Parametric Study of the Spark Plasma Sintering Process on the Mechanical Properties of Multilayer Graphene Reinforced Ti6Al4V Nanocomposites. Trans Indian Inst Met. 76, (2023) 1015–1025.

3. **D. Sharma,** V.K. Singla, S. Singh, Mechanical and wear characteristics of spark plasma sintered titanium/multilayer graphene nanocomposites. Proc IMechE Part E: J Process Mechanical Engineering. 0 (2023) 1-10.

Communicated

1. **D. Sharma**, S. Singh, V.K. Singla, Parametric study on Wear and Corrosion Properties of MultiLayer Graphene reinforced Titanium Alloy (Ti64) Composite. (Under Review)

References

[1] E. Omrani, A.D. Moghadam, P.L. Menezes, P.K. Rohatgi, New Emerging Self-lubricating Metal Matrix Composites for Tribological Applications, Ecotribology. (2015) 63-103.

[2] I. Aatthisugan, A. Razal Rose, D. Selwyn Jebadurai, Mechanical and wear behaviour of AZ91D magnesium matrix hybrid composite reinforced with boron carbide and graphite, J. Magnes. Alloy. 5 (2017) 20–25.

[3] D.K. Rajak, D.D. Pagar, R. Kumar, C.I. Pruncu, Recent progress of reinforcement materials: A comprehensive overview of composite materials, J. Mater. Res. Technol. 8 (2019) 6354–6374.

[4] A.K. Sharma, R. Bhandari, A. Aherwar, R. Rimašauskiene, C. Pinca-Bretotean, A study of advancement in application opportunities of aluminum metal matrix composites, Mater. Today Proc. 26 (2020) 2419–2424.

[5] B. Parveez, M.I. Kittur, I.A. Badruddin, S. Kamangar, M. Hussien, M.A. Umarfarooq, Scientific Advancements in Composite Materials for Aircraft Applications: A Review, Polymers (Basel). 14 (2022) 5007.

[6] S. Siengchin, A review on lightweight materials for defence applications: Present and future developments, Def. Technol. 24 (2023) 1–17.

[7] S.K. Sharma, K.K. Saxena, A.K. Dixit, R. Kishore, K.A. Mohammed, Role of additive manufacturing and various reinforcements in MMCs related to biomedical applications, Adv. Mater. Process. Technol. 00 (2022) 1–18.

[8] A. Kumar, A. Patnaik, I.K. Bhat, Investigation of nickel metal powder on tribological and mechanical properties of Al-7075 alloy composites for gear materials, Powder Metall. 60 (2017) 371–383.

[9] V. Mohanavel, M. Ravichandran, S. Suresh Kumar, Tribological and mechanical properties of Zirconium Di-boride (ZrB2) particles reinforced aluminium matrix composites, Mater. Today Proc. 21 (2020) 862–864.

[10] B. Chen, K. Kondoh, J.S. Li, M. Qian, Extraordinary reinforcing effect of carbon nanotubes in aluminium matrix composites assisted by in-situ alumina nanoparticles, Compos. Part B Eng. 183 (2020) 107691.

[11] Y. Say, O. Guler, B. Dikici, Carbon nanotube (CNT) reinforced magnesium matrix composites: The effect of CNT ratio on their mechanical properties and corrosion resistance, Mater. Sci. Eng. A. 798 (2020) 139636.

[12] I. Dinaharan, S.C. Vettivel, M. Balakrishnan, E.T. Akinlabi, Influence of processing route on microstructure and wear resistance of fly ash reinforced AZ31 magnesium matrix composites, J. Magnes. Alloy. 7 (2019) 155–165.

[13] F. Chen, J. Ying, Y. Wang, S. Du, Z. Liu, Q. Huang, Effects of graphene content on the microstructure and properties of copper matrix composites, Carbon N. Y. 96 (2016) 836–842.

[14] S.I. Hussein, A.M. Abd-Elnaiem, T.B. Asafa, H.I. Jaafar, Effect of incorporation of conductive fillers on mechanical properties and thermal conductivity of epoxy resin composite, Appl. Phys. A Mater. Sci. Process. 124 (2018) 475.

[15] S.C. Tjong, K.C. Lau, Tribological behaviour of SiC particle-reinforced copper matrix

composites, Mater. Lett. 43 (2000) 274–280.
[16] M. Balazic, J. Kopac, M. J Jackson, W. Ahmed, Titanium and Titanium Alloy Applications in Medicine, Int. J. Nano Biomater. 1 (2007) 3–34.
[17] P. Bocchetta, L.Y. Chen, J.D.C. Tardelli, A.C. Dos Reis, F. Almeraya-Calderón, P. Leo, Passive layers and corrosion resistance of biomedical ti-6al-4v and β-ti alloys, Coatings. 11 (2021) 487.
[18] C. Veiga, J.P. Davim, A.J.. Loureiro, Properties and applications of titanium alloys: A brief review, Rev. Adv. Mater. Sci. 32 (2012) 133–148.
[19] M. Łępicka, M. Grądzka-Dahlke, D. Pieniak, K. Pasierbiewicz, K. Kryńska, A. Niewczas, Tribological performance of titanium nitride coatings: A comparative study on TiN-coated stainless steel and titanium alloy, Wear. 422–423 (2019) 68–80.
[20] Y. Pan, W. Li, X. Lu, M.D. Hayat, L. Yin, W. Song, X. Qu, P. Cao, Microstructure and tribological properties of titanium matrix composites reinforced with in situ synthesized TiC particles, Mater. Charact. 170 (2020) 110633.
[21] J. Wozniak, M. Petrus, T. Cygan, A. Jastrzębska, T. Wojciechowski, W. Ziemkowska, A. Olszyna, Silicon carbide matrix composites reinforced with two-dimensional titanium carbide – Manufacturing and properties, Ceram. Int. 45 (2019) 6624–6631.
[22] B.P. Sahoo, D. Das, A.K. Chaubey, Strengthening mechanisms and modelling of mechanical properties of submicron-TiB2 particulate reinforced Al 7075 metal matrix composites, Mater. Sci. Eng. A. 825 (2021) 141873.
[23] Höganäs, Production of Sintered Components 2, Höganäs Handbook, 2013.
[24] M. Penchal Reddy, R.A. Shakoor, A.M.A. Mohamed, M. Gupta, Microwave rapid sintering of al-metal matrix composites: A review on the effect of reinforcements, microstructure and mechanical properties, Metals. 6 (2016) 143.
[25] G. Molénat, L. Durand, J. Galy, A. Couret, Temperature Control in Spark Plasma Sintering: An FEM Approach, J. Metall. 2010 (2010) 145431.
[26] F. Pusavec, J. Kenda, The transition to a clean, dry, and energy efficient polishing process: An innovative upgrade of abrasive flow machining for simultaneous generation of micro-geometry and polishing in the tooling industry, J. Clean. Prod. 76 (2014) 180–189.
[27] B. Duan, J. Zhou, Y. Liu, C. Wang, Y. Zhang, Investigation on surface roughness in chemical mechanical polishing of TiO2 thin film, J. Semicond. 35 (2014) 063006.
[28] V. Kumar, R. Sharma, K. Dhakar, Y.K. Singla, K. Verma, Experimental evaluation of magnetic abrasive finishing process with diamond abrasive, Int. J. Mater. Prod. Technol. 58 (2019) 55–70.
[29] M.R. Sankar, J. Ramkumar, V.K. Jain, Experimental investigation and mechanism of material removal in nano finishing of MMCs using abrasive flow finishing (AFF) process, Wear. 266 (2009) 688–698.
[30] V.K. Jain, Nanofinishing science and technology: Basic and advanced finishing and polishing processes, CRC Press, 2016.
[31] M. Ravi Sankar, V.K. Jain, J. Ramkumar, Y.M. Joshi, Rheological characterization of styrene-butadiene based medium and its finishing performance using rotational abrasive flow finishing process, Int. J. Mach. Tools Manuf. 51 (2011) 947–957.
[32] S. Singh, M.R. Sankar, Rheological study of the developed medium and its correlation

with surface roughness during abrasive flow finishing of micro-slots, Mach. Sci. Technol. 24 (2020) 882–905.

[33] S. Singh, A.S.A. Raj, M.R. Sankar, V.K. Jain, Finishing force analysis and simulation of nanosurface roughness in abrasive flow finishing process using medium rheological properties, Int. J. Adv. Manuf. Technol. 85 (2016) 2163–2178.

[34] H. Pan, L. Ding, Y. Xu, L. Li, J. Chen, S. Wang, P. Jiang, Microstructure, mechanical and thermal properties of titanium matrix composites with different reinforcements, Mater. Res. Express. 9 (2022) 096512.

[35] S. Li, K. Kondoh, H. Imai, B. Chen, L. Jia, J. Umeda, Microstructure and mechanical properties of P/M titanium matrix composites reinforced by in-situ synthesized TiC-TiB, Mater. Sci. Eng. A. 628 (2015) 75–83.

[36] M.A. Lagos, I. Agote, G. Atxaga, O. Adarraga, L. Pambaguian, Fabrication and characterisation of Titanium Matrix Composites obtained using a combination of Self propagating High temperature Synthesis and Spark Plasma Sintering, Mater. Sci. Eng. A. 655 (2016) 44–49.

[37] S. Pouzet, P. Peyre, C. Gorny, O. Castelnau, T. Baudin, F. Brisset, C. Colin, P. Gadaud, Additive layer manufacturing of titanium matrix composites using the direct metal deposition laser process, Mater. Sci. Eng. A. 677 (2016) 171–181.

[38] O.E. Falodun, B.A. Obadele, S.R. Oke, O.O. Ige, P.A. Olubambi, M.L. Lethabane, S.W. Bhero, Influence of spark plasma sintering on microstructure and wear behaviour of Ti-6Al-4V reinforced with nanosized TiN, Trans. Nonferrous Met. Soc. China. 28 (2018) 47–54.

[39] M. Sribalaji, B. Mukherjee, S.R. Bakshi, P. Arunkumar, K. Suresh Babu, A.K. Keshri, In-situ formed graphene nanoribbon induced toughening and thermal shock resistance of spark plasma sintered carbon nanotube reinforced titanium carbide composite, Compos. Part B Eng. 123 (2017) 227–240.

[40] Y. Liu, L. Dong, J. Lu, W. Huo, Y. Du, W. Zhang, Y. Zhang, Microstructure and mechanical properties of SiC nanowires reinforced titanium matrix composites, J. Alloys Compd. 819 (2019) 152953.

[41] B. Chen, J. Shen, X. Ye, H. Imai, J. Umeda, M. Takahashi, K. Kondoh, J. Shen, X. Ye, H. Imai, J. Umeda, M. Takahashi, K. Kondoh, Solid-state interfacial reaction and load transfer efficiency in carbon nanotubes (CNTs)-reinforced aluminum matrix composites, Carbon. 114 (2017) 198–208.

[42] L. Wei, X. Liu, Y. Gao, X. Lv, N. Hu, M. Chen, Synergistic strengthening effect of titanium matrix composites reinforced by graphene oxide and carbon nanotubes, Mater. Des. 197 (2021) 109261.

[43] K. Kondoh, Titanium metal matrix composites by powder metallurgy (PM) routes, Elsevier Inc., 2015.

[44] W.Z. Yang, W.M. Huang, Z.F. Wang, F.J. Shang, W. Huang, B.Y. Zhang, Thermal and mechanical properties of graphene-titanium composites synthesized by microwave sintering, Acta Metall. Sin. (Engli. Lett.) 29 (2016) 707–713.

[45] Z. Cao, X. Wang, J. Li, Y. Wu, H. Zhang, J. Guo, S. Wang, Reinforcement with graphene nanoflakes in titanium matrix composites, J. Alloys Compd. 696 (2017) 498–502.

[46] K.S. Munir, Y. Zheng, D. Zhang, J. Lin, Y. Li, C. Wen, Improving the strengthening efficiency of carbon nanotubes in titanium metal matrix composites, Mater. Sci. Eng. A. 696 (2017) 10–25.
[47] X.N. Mu, H.N. Cai, H.M. Zhang, Q.B. Fan, F.C. Wang, Z.H. Zhang, Y. Wu, Y.X. Ge, S. Chang, R. Shi, Y. Zhou, D.D. Wang, Uniform dispersion of multi-layer graphene reinforced pure titanium matrix composites via flake powder metallurgy, Mater. Sci. Eng. A. 725 (2018) 541–548.
[48] X.N. Mu, H.N. Cai, H.M. Zhang, Q.B. Fan, Z.H. Zhang, Y. Wu, Y.X. Ge, D.D. Wang, Interface evolution and superior tensile properties of multi-layer graphene reinforced pure Ti matrix composite, Mater. Des. 140 (2018) 431–441.
[49] M. Gürbüz, T. Mutuk, Effect of process parameters on hardness and microstructure of graphene reinforced titanium composites, J. Compos. Mater. 52 (2018) 543–551.
[50] J. Lu, L. Dong, Y. Liu, Y. Fu, W. Zhang, Y. Du, Y. Zhang, Y. Zhao, Simultaneously enhancing the strength and ductility in titanium matrix composites via discontinuous network structure, Compos. Part A Appl. Sci. Manuf. 136 (2020) 105971.
[51] X.N. Mu, H.N. Cai, H.M. Zhang, Q.B. Fan, X.W. Cheng, F.C. Wang, Z.H. Zhang, Y.X. Ge, S. Chang, Y.N. Liu, L. Liu, H.Q. Duan, The role of interfacial reaction on dynamic mechanical response in graphene nano-flake/Ti composites, Carbon. 152 (2019) 986–990.
[52] K. Soorya Prakash, P.M. Gopal, D. Anburose, V. Kavimani, Mechanical, corrosion and wear characteristics of powder metallurgy processed Ti-6Al-4V/B4C metal matrix composites, Ain Shams Eng. J. 9 (2018) 1489–1496.
[53] H. Attar, S. Ehtemam-Haghighi, D. Kent, I. V. Okulov, H. Wendrock, M. Bönisch, A.S. Volegov, M. Calin, J. Eckert, M.S. Dargusch, Nanoindentation and wear properties of Ti and Ti-TiB composite materials produced by selective laser melting, Mater. Sci. Eng. A. 688 (2017) 20–26.
[54] A. Sabahi Namini, S.A.A. Dilawary, A. Motallebzadeh, M. Shahedi Asl, Effect of TiB2 addition on the elevated temperature tribological behavior of spark plasma sintered Ti matrix composite, Compos. Part B Eng. 172 (2019) 271–280.
[55] F. Saba, F. Zhang, S. Liu, T. Liu, Reinforcement size dependence of mechanical properties and strengthening mechanisms in diamond reinforced titanium metal matrix composites, Compos. Part B Eng. 167 (2019) 7–19.
[56] A.L. Rominiyi, M.B. Shongwe, E.N. Ogunmuyiwa, B.J. Babalola, P.F. Lepele, P.A. Olubambi, Effect of nickel addition on densification, microstructure and wear behaviour of spark plasma sintered CP-titanium, Mater. Chem. Phys. 240 (2020) 122130.
[57] H. Izui, K. Hattori, Y. Komiya, Dry sliding wear resistance characterization of titanium matrix composites reinforced with titanium carbonitrides, Mech. Eng. J. 7 (2020) 20-00029.
[58] K.K. Alaneme, O.P. Adu, S.R. Oke, O.E. Falodun, P.A. Olubambi, Densification characteristics, microstructure and wear behaviour of spark plasma sintering processed titanium-niobium pentoxide (Ti-Nb2O5) based composites, J. King Saud Univ. - Eng. Sci. 34 (2022) 282–289.
[59] G. Ma, C. Yu, B. Tang, Y. Li, F. Niu, D. Wu, G. Bi, S. Liu, High-mass-proportion

TiCp/Ti6Al4V titanium matrix composites prepared by directed energy deposition, Addit. Manuf. 35 (2020) 101323.
[60] M. Selvakumar, T. Ramkumar, M. Mohanraj, P. Chandramohan, P. Narayanasamy, Experimental investigations of reciprocating wear behavior of metal matrix (Ti/TiB) composites, Arch. Civ. Mech. Eng. 20 (2020) 26.
[61] Y. Xiong, M. Du, F. Zhang, F. Saba, C. Shang, Preparation and mechanical properties of titanium alloy matrix composites reinforced by Ti3AlC and TiC ceramic particulates, J. Alloys Compd. 886 (2021) 161216.
[62] J. Jin, S. Zhou, Y. Zhao, Q. Zhang, X. Wang, W. Li, D. Chen, L.C. Zhang, Refined microstructure and enhanced wear resistance of titanium matrix composites produced by selective laser melting, Opt. Laser Technol. 134 (2021) 106644.
[63] R. Kumar, M. Antonov, L. Liu, I. Hussainova, Sliding wear performance of in-situ spark plasma sintered Ti-TiBw composite at temperatures up to 900 °C, Wear. 476 (2021) 203663.
[64] F. Song, Q. Wang, T. Wang, The effects of crystallinity on the mechanical properties and the limiting PV (pressure×velocity) value of PTFE, Tribol. Int. 93 (2016) 1–10.
[65] J. Yu, Q. Zhao, Y. Zhao, W. Zhang, L. Dong, J. Lu, W. Huo, Y. Zhang, The tribological behavior of different carbon nanomaterials-reinforced the titanium (TC21) matrix composite, J. Mater. Res. Technol. 15 (2021) 3683–3693.
[66] M. Gürbüz, T. Mutuk, P. Uyan, Mechanical, Wear and Thermal Behaviors of Graphene Reinforced Titanium Composites, Met. Mater. Int. 27 (2021) 744–752.
[67] Anawati, H. Tanigawa, H. Asoh, T. Ohno, M. Kubota, S. Ono, Electrochemical corrosion and bioactivity of titanium-hydroxyapatite composites prepared by spark plasma sintering, Corros. Sci. 70 (2013) 212–220.
[68] C. Prakash, S. Singh, S. Ramakrishna, G. Królczyk, C.H. Le, Microwave sintering of porous Ti–Nb-HA composite with high strength and enhanced bioactivity for implant applications, J. Alloys Compd. 824 (2020) 153774.
[69] J. Fojt, L. Joska, J. Málek, Corrosion behaviour of porous Ti-39Nb alloy for biomedical applications, Corros. Sci. 71 (2013) 78–83.
[70] E. Yılmaz, A. Gökçe, F. Findik, H.O. Gulsoy, O. İyibilgin, Mechanical properties and electrochemical behavior of porous Ti-Nb biomaterials, J. Mech. Behav. Biomed. Mater. 87 (2018) 59–67.
[71] J.C. Wang, Y.J. Liu, P. Qin, S.X. Liang, T.B. Sercombe, L.C. Zhang, Selective laser melting of Ti–35Nb composite from elemental powder mixture: Microstructure, mechanical behavior and corrosion behavior, Mater. Sci. Eng. A. 760 (2019) 214–224.
[72] H. Gu, Z. Ding, Z. Yang, W. Yu, W. Zhang, W. Lu, L.C. Zhang, K. Wang, L. Wang, Y. fei Fu, Microstructure evolution and electrochemical properties of TiO 2 /Ti-35Nb-2Ta-3Zr micro/nano-composites fabricated by friction stir processing, Mater. Des. 169 (2019) 107680.
[73] B.N. Mordyuk, S.M. Voloshko, V.I. Zakiev, A.P. Burmak, V. V. Mohylko, Enhanced Resistance of Ti6Al4V Alloy to High-Temperature Oxidation and Corrosion by Forming Alumina Composite Coating, J. Mater. Eng. Perform. 30 (2021) 1780–1795.
[74] S. Zhou, Y. Zhao, X. Wang, W. Li, D. Chen, T.B. Sercombe, Enhanced corrosion resistance of Ti-5 wt.% TiN composite compared to commercial pure Ti produced by

selective laser melting in HCl solution, J. Alloys Compd. 820 (2020) 153422.
[75] A. Bordbar-Khiabani, S. Ebrahimi, B. Yarmand, Highly corrosion protection properties of plasma electrolytic oxidized titanium using rGO nanosheets, Appl. Surf. Sci. 486 (2019) 153–165.
[76] S. Singh, K.K. Pandey, A. Islam, A.K. Keshri, Corrosion behaviour of plasma sprayed graphene nanoplatelets reinforced hydroxyapatite composite coatings in simulated body fluid, Ceram. Int. 46 (2020) 13539–13548.
[77] S. Singh, C. Prakash, A. Pramanik, A. Basak, R. Shabadi, G. Królczyk, M. Bogdan-Chudy, A. Babbar, Magneto-rheological fluid assisted abrasive nanofinishing of β-phase ti-nb-ta-zr alloy: Parametric appraisal and corrosion analysis, Materials (Basel). 13 (2020) 1–15.
[78] H. Shi, D. Liu, Y. Pan, W. Zhao, X. Zhang, A. Ma, B. Liu, Y. Hu, W. Wang, Effect of shot peening and vibration finishing on the fatigue behavior of TC17 titanium alloy at room and high temperature, Int. J. Fatigue. 151 (2021) 106391.
[79] G. Ghosh, A. Sidpara, P.P. Bandyopadhyay, Performance improvement of magnetorheological finishing using chemical etchant and diamond-graphene based magnetic abrasives, Precis. Eng. 79 (2023) 221–235.
[80] Y. Tian, C. Shi, Z. Fan, Q. Zhou, Experimental investigations on magnetic abrasive finishing of Ti-6Al-4V using a multiple pole-tip finishing tool, Int. J. Adv. Manuf. Technol. 106 (2020) 3071–3080.
[81] G. Parameswari, V.K. Jain, J. Ramkumar, L. Nagdeve, Experimental investigations into nanofinishing of Ti6Al4V flat disc using magnetorheological finishing process, Int. J. Adv. Manuf. Technol. 100 (2019) 1055–1065.
[82] H.S. Mali, A. Manna, Optimum selection of abrasive flow machining conditions during fine finishing of Al/15 wt% SiC-MMC using Taguchi method, Int. J. Adv. Manuf. Technol. 50 (2010) 1013–1024.
[83] M.R. Sankar, V.K. Jain, K.P. Rajurkar, Nano-finishing Studies Using Elastically Dominant Polymers Blend Abrasive Flow Finishing Medium, Procedia CIRP. 68 (2018) 529–534.
[84] M. Sushil, K. Vinod, K. Harmesh, Experimental Investigation and Optimization of Process Parameters of Al/SiC MMCs Finished by Abrasive Flow Machining, Mater. Manuf. Process. 30 (2015) 902–911.
[85] D. Sudhakara, S. Suresh, B. Vinod, Experimental Study on Abrasive Flow Machining (AFM): New Approach for Investigation on Nano-SiC in the Improvement of Material Removal and Surface Finishing, J. Bio- Tribo-Corrosion. 6 (2020).
[86] V.B. Bhandari, Design of Machine Elements, Tata McGraw-Hill Publishing House Pvt. Ltd., 2009.
[87] R.S. Khurmi, J.K. Gupta, A Textbook of Machine Design, Eurasia Publishing House Pvt. Ltd., 2006.
[88] Y. Yan, G.L. Nash, P. Nash, Effect of density and pore morphology on fatigue properties of sintered Ti-6Al-4V, Int. J. Fatigue. 55 (2013) 81–91.
[89] M. Rashad, F. Pan, Z. Yu, M. Asif, H. Lin, R. Pan, Investigation on microstructural, mechanical and electrochemical properties of aluminum composites reinforced with graphene nanoplatelets, Prog. Nat. Sci. Mater. Int. 25 (2015) 460–470.

[90] V.K. Sharma, V. Kumar, R.S. Joshi, Investigation of rare earth particulate on tribological and mechanical properties of Al-6061 alloy composites for aerospace application, J. Mater. Res. Technol. 8 (2019) 3504–3516.
[91] A. Moses, R. Machaka, S. Sipho, L. Mtech, S. Ranti, M. Ajimegoh, A.M. Eng, P. Apata, Materials Science & Engineering A Nanoindentation studies of the mechanical behaviours of spark plasma sintered multiwall carbon nanotubes reinforced Ti6Al4V nanocomposites, Mater. Sci. Eng. A. 765 (2019) 138320.
[92] K. Fan, F. Zhang, C. Shang, F. Saba, J. Yu, Mechanical properties and strengthening mechanisms of titanium matrix nanocomposites reinforced with onion-like carbons, Compos. Part A. 132 (2020) 105834.
[93] L. Chen, Z. Huang, S. Kumar, Impact of bonding at multi-layer graphene/metal Interfaces on thermal boundary conductance, R. Soc. Chem. 4 (2014) 35852–35861.
[94] W. Wang, H. Zhou, Q. Wang, B. Wei, S. Xin, Y. Gao, Microstructural evolution and mechanical properties of graphene-reinforced Ti-6Al-4V composites synthesized via spark plasma sintering, Metals. 10 (2020) 737.
[95] Y. Song, Y. Chen, W.W. Liu, W.L. Li, Y.G. Wang, D. Zhao, X.B. Liu, Microscopic mechanical properties of titanium composites containing multi-layer graphene nanofillers, Mater. Des. 109 (2016) 256–263.
[96] Q. Yan, B. Chen, J.S. Li, Super-high-strength graphene/titanium composites fabricated by selective laser melting, Carbon. 174 (2021) 451–462.
[97] H. chuan Cao, Y. long Liang, The microstructures and mechanical properties of graphene-reinforced titanium matrix composites, J. Alloys Compd. 812 (2020) 152057.
[98] S. Ehtemam-haghighi, G. Cao, L. Zhang, Nanoindentation study of mechanical properties of Ti based alloys with Fe and Ta additions, J. Alloys Compd. 692 (2017) 892–897.
[99] K. Arora, A.K. Singh, Magnetorheological finishing of UHMWPE acetabular cup surface and its performance analysis, Mater. Manuf. Process. 35 (2020) 1631–1649.
[100] A. Oketola, T. Jamiru, O. Ogunbiyi, A.L. Rominiyi, S. Smith, O.D. Adedayo, Process parametric optimization of spark plasma sintered Ni–Cr–ZrO2 composites using response surface methodology (RSM), Int. J. Light. Mater. Manuf. 7 (2024) 14–24.
[101] M. Rahimian, N. Ehsani, N. Parvin, H. reza Baharvandi, The effect of particle size, sintering temperature and sintering time on the properties of Al-Al2O3 composites, made by powder metallurgy, J. Mater. Process. Technol. 209 (2009) 5387–5393.
[102] H. Yun, B. Zou, J. Wang, Effects of sintering temperature and nano Ti(C,N) on the microstructure and mechanical properties of Ti(C,N) cermets cutting tool materials with low Ni-Co, Mater. Sci. Eng. A. 705 (2017) 98–104.
[103] S. Grützner, L. Krüger, M. Radajewski, I. Schneider, Characterization of in-situ TiB/TiC particle-reinforced Ti-5Al-5Mo-5V-3Cr matrix composites synthesized by solid-state reaction with B4C and graphite through sps, Metals. 8 (2018) 377.
[104] M.C. Şenel, M. Gürbüz, E. Koç, Mechanical and tribological behaviours of aluminium matrix composites reinforced by graphene nanoplatelets, Mater. Sci. Technol. (United Kingdom). 34 (2018) 1980–1989.
[105] A. Bahrami, N. Soltani, M.I. Pech-Canul, Effect of sintering temperature on

tribological behavior of Ce-TZP/Al2O3-aluminum nanocomposite, J. Compos. Mater. 49 (2015) 3507–3514.
[106] V.A. Alves, R.Q. Reis, I.C.B. Santos, D.G. Souza, T. de, M.A. Pereira-da-Silva, A. Rossi, L.A. da Silva, In situ impedance spectroscopy study of the electrochemical corrosion of Ti and Ti-6Al-4V in simulated body fluid at 25 °C and 37 °C, Corros. Sci. 51 (2009) 2473–2482.
[107] B. Beverskog, J.O. Carlsson, A. Delblanc Bauer, C. V. Deshpandey, H.J. Doerr, R.F. Bunshah, B.P. O'Brien, Corrosion properties of TiC films prepared by activated reactive evaporation, Surf. Coatings Technol. 41 (1990) 221–229.
[108] G. Kant, K.S. Sangwan, Predictive modelling and optimization of machining parameters to minimize surface roughness using artificial neural network coupled with genetic algorithm, Procedia CIRP. 31 (2015) 453–458.
[109] M.R. Sankar, V.K. Jain, J. Ramkumar, K.K. Kar, Rheological characterisation and performance evaluation of a new medium developed for abrasive flow finishing, Int. J. Precis. Technol. 1 (2010) 302.
[110] V.K. Jain, S.G. Adsul, Experimental investigations into abrasive flow machining (AFM), Int. J. Mach. Tools Manuf. 40 (2000) 1003–1021.